TECHNICAL UNIVERSITY OF KOŠICE
Faculty of Electrical Engineering and Informatics
Department of Electronics and Multimedia Communications

THROUGH WALL IMAGING WITH UWB RADAR SYSTEM

by
Ing. Michal Aftanas

A dissertation submitted in partial fulfillment
of the requirements for the degree of
Doctor of Philosophy
(Electrical Engineering: 5.2.13 Electronics)

August, 2009

Supervisor: **doc. Ing. Miloš Drutarovský, CSc.**

"If we save even one life, we have been cost effective."
Dr. Rochelle Dicker

Acknowledgement

I give a sincere gratitude to all the people who made it possible for me to write this thesis, especially to my family. I also want to thank to the doc. Ing. Miloš Drutarovský, CSc. for my supervising, to the Dr. Jürgen Sachs and Dr. Rudolf Zetik for their technical and theoretical suggestions and remarks, and to the prof. Ing. Dušan Kocur, CSc. for his support.

Contents

List of Tables

List of Figures

List of Abbreviations

1D	–	One dimensional
2D	–	Two dimensional
3D	–	Three dimensional
ADC	–	Analog to Digital Converter
ART	–	Algebraic Reconstruction Technique
AWGN	–	Additive White Gaussian Noise
BST	–	Boundary Scattering Transform
DSAR	–	Differential Synthetic Aperture Radar
ECS	–	Extended Chirp Scaling
EOK	–	Extended Omega Ka
FFT	–	Fast Fourier Transform
GPR	–	Ground Penetrating Radar
HT	–	Hough Transform
IBST	–	Inverse Boundary Scattering Transform
IFFT	–	Inverse Fast Fourier Transform
IHT	–	Inverse Hough Transform
IR	–	Impulse Response
MAC	–	Multiply And Accumulate
M-sequence	–	MLBS – Maximum Length Binary Sequence
MUSIC	–	MUltiple SIgnal Characterization
NUFFT	–	NonUniform Fast Fourier Transformation
RADAR	–	RAdio Detection And Ranging system
RAW	–	Unprocessed data
RPE	–	Relative Positioning Error
RX	–	Receiver
SAR	–	Synthetic Aperture Radar
SEABED	–	Shape Estimation Algorithm based on Boundary Scattering Transform and Extraction of Directly scattered waves
SCR	–	Signal to Clutter Ratio
SVD	–	Singular Value Decomposition
TOA	–	Time Of Arrival
TWR	–	Through Wall Radar
TX	–	Transmitter
T&H	–	Track And Hold
UWB	–	Ultra Wide Band

List of Symbols

$*$	–	Convolution
*	–	Complex conjugation
a	–	Attenuation
a_w	–	Wall attenuation
α	–	Attenuation constant
A	–	Antenna position
$A(t)$	–	Source waveform at the scatterpoint
$A\,(k_x, f)$	–	first arbitrary function of (k_x, f)
$\vec{A}$	–	Vector function
$B\,(k_x, f)$	–	second arbitrary function of (k_x, f)
$B(X, n)$	–	Received B-scan
B_s	–	Oversampled B-scan
$B_{s\tau}$	–	Oversampled B-scan shifted to the time zero
$B_{s\tau c}$	–	Oversampled B-scan shifted to the time zero with removed crosstalk
B_P	–	Preprocessed B-scan
B_{PC}	–	Preprocessed B-scan with compensated irregular movement
B_Δ	–	B-scan modified for differential SAR
β	–	Propagation factor
c	–	Speed of the light in the vacuum
co	–	Coefficients of a polynomial equation
C_A	–	Crosstalk
d	–	Distance that wave flight inside a wall in X direction
d_{init}	–	Initial condition of d
d_{inwall}	–	Distance that wave flight in the wall
d_{tot}	–	Total distance that wave flight between antenna and target
d_{tot_bist}	–	Total distance that wave flight between antenna and target in bistatic cases
d_{tot_TX2T}	–	Total distance that wave flight between transmit antenna and target
d_{tot_T2RX}	–	Total distance that wave flight between target and receive antenna
$d_{TX\,RX}$	–	Distance between TX and RX
D	–	Pseudo spectrum
D_w	–	Thickness of the wall
δ	–	Dirac delta function
ε	–	Permittivity
ε_a	–	Permittivity of the air
ε_w	–	Permittivity of the wall

ε_{ra}	–	Relative permittivity of the air
ε_{rw}	–	Relative permittivity of the wall
E^{rad}	–	Radiated electric field
E^{meas}	–	Measured electric field
Err_d	–	Relative error of d
Err_{TOA}	–	Relative error of TOA
en	–	Delay between two adjacent multiple reflections
FFT	–	Fast Fourier transform
$F(k)$	–	Filter for multiple echo reducing
f	–	Frequency
f_c	–	Clock frequency
$footprint$	–	Weight function of antenna look angle
$G(x_0; x)$	–	Greens function, x_0: source point , x: observation point
g^p	–	Vector of Greens functions
Γ	–	Reflection coefficient
HF	–	Hough transform
H_x	–	Distance from antenna to the target in X direction
H_z	–	Distance from antenna to the target in Z direction
h	–	Transfer function
h_A	–	Transfer function of a measurement system
h_s	–	Transfer function of a radar system including antennas
h_C	–	Transfer function of a clutter
h_T	–	Transfer function of a target
h_m	–	Transfer function of antenna measured against an ideal reflector
h_{TX}	–	Transfer function of a transmit antenna
h_{RX}	–	Transfer function of a receive antenna
i	–	Artificial variable
I	–	Number of iterations
$I(x_T, z_T)$	–	Migrated image
$I_F(x_T, z_T)$	–	Migrated image transformed back from Hough space
$I_w(x_T, z_T)$	–	Migrated image after all compensations
$I_{wDE}(x_T, z_T)$	–	Migrated image with detected edges
$I_{HT}(x_T, z_T)$	–	Hough Transform of migrated image with detected edges
$I_{WHT}(x_T, z_T)$	–	Hough Transform of migrated image with detected edges after filtering in Hough space
$IFFT$	–	Inverse fast Fourier transform
IHF	–	Inverse Hough transform
j	–	Number of receive antennas, also artificial variable
k	–	Wavenumber, also oversampled discrete time, also artificial variable

k_x – Horizontal wavenumber
k_z – Vertical wavenumber
K – Multistatic response matrix
KO – Oversampling factor
λ – Eigenvalue
M – Chips number of M-sequence, also number of scatterers
μ – Permeability
μ_a – Permeability of the air
μ_w – Permeability of the wall
μ_{rw} – Relative permeability of the wall
N – Number of antennas positions
N_x – Resolution of migrated image in X direction
N_z – Resolution of migrated image in Z direction
n – Discrete time, also artificial variable, also number of transmit antennas
$\vec{n}$ – Outward pointing normal to the surface
$noise$ – Noise
$\overrightarrow{\nabla}$ – Divergence
∇^2 – Laplacian
O_{SAR} – Computational complexity of SAR imaging
O_{Kir} – Computational complexity of Kirchhoff migration
O_{Sto} – Computational complexity of Stolt migration
ω – Angular frequency
P – Position of point-like target
ϕ – Scalar wavefield in frequency domain, also angle of wave
ϕ_0 – Scalar potential at $z = 0$
ψ – Scalar wavefield in time domain
R – Position of antenna center
r, θ, φ – Spatial coordinates
r – Distance from the origin to the line along a vector perpendicular to the line
σ – Conductivity
σ_w – Conductivity of the wall
$S(X, Z)$ – Measured space with coordinates X and Z
S_{pline} – Spline function
S_0 – Surface at plane $Z = 0$
S_z – Surface below the reflector
S_∞ – Surface at vertical cylindrical walls
$surf$ – Surface
θ – vertical angle between the receiver and ray to the scatterpoint, also angle of the vector perpendicular to the line

θ_w – Wall angle
T – Transmission coefficient, also target position
TOA – Time of arrival
TOA_{AT} – Travel time between antenna and target
TOA_{TX-T} – Travel time between transmit antenna and target
TOA_{T-RX} – Travel time between target and receive antenna
t – Time
Δt – Time difference between air-wall and wall-air interface
$t_{TX\,RX}$ – Travel time between TX and RX
t_{inwall} – Travel time inside a wall
t_{delay} – Time delay caused by through the wall penetration
$\tau(k)$ – Time zero
$\tau(m)$ – Strength of m-th target
V_S – Voltage at transmit antenna
V_R – Voltage at receive antenna
v – Velocity of a wave propagation, also eigenvector
v_w – Velocity of a wave propagation inside a wall
v_0 – Constant velocity of a wave propagation
vol – Volume
∂V – Surface of V
W – Inflection point
W_{di} – Distance from antenna to the wall
W_H – Window function
w – Weight function of antenna footprint
X – Position of scatterer, also coordination X
$X(r, \theta, \varphi, n)$ – Transfer function of measured environment
$[x_T, z_T]$ – Coordinations of target
$[x_{tr}, z_{tr}]$ – Coordinations of transmitter
$[x_{re}, z_{re}]$ – Coordinations of receiver
Z – Coordination Z
Z_0 – Impedance of the air
Z_c – Impedance of the cable

Chapter 1

Introduction

1.1 Motivation

A man was interested in knowing of unknown from the very beginning of the human history. Our human eyes help us to investigate our environment by reflection of light. However, wavelengths of visible light allows transparent view through only a very small kinds of materials. On the other hand, Ultra WideBand (UWB) electromagnetic waves with frequencies of few Gigahertz are able to penetrate through almost all types of materials around us. With some sophisticated methods and a piece of luck we are able to investigate what is behind opaque walls. Rescue and security of the people is one of the most promising fields for such applications.

Rescue: Imagine how useful can be information about interior of the barricaded

Fig. 1.1.1: Policeman is scanning the room with terrorists and hostage.

Fig. 1.1.2: Fireman is scanning the room on fire.

building with terrorists and hostages inside for a policemen. The tactics of police raid can be build up on realtime information about ground plan of the room and positions of big objects inside. How useful for the firemen can be information about current interior state of the room before they get inside? Such hazardous environment, full of smoke with zero visibility, is very dangerous and each additional information can make the difference between life and death.

Security: Investigating objects through plastic, rubber, dress or other nonmetallic materials could be highly useful as an additional tool to the existing x-ray scanners. Especially it could be used for scanning baggage at the airport, truckloads on borders, dangerous boxes, etc.

1.2 Problem Formulation

The UWB radar system is used for scanning of the objects behind a wall. An electromagnetic wave is transmitted via antenna system, penetrates through the wall, it is reflected by the investigated object, penetrates again through the wall, and is received back via receiver antenna. The wall cannot be too thick, and may not be from to attenuating material in the used frequency band, to allow electromagnetic wave to travel through the wall and back. Every time the wave passes into (or from) an another material, the reflection, refraction, diffraction, and absorption on the boundaries of these materials occurs [10]. Also multiple reflections between antennas, walls, and all the objects in the scanned area arise.

In addition, the wave changes the velocity of its propagation depending on the material properties. As the result of all these factors, the radar receives a very complex signal, full of noise and clutters, which is very difficult to interpret. The main aim of the signal processing stages between the receiver and the radar display is to decompose the received interposed signals, use them for estimation of the scanned environment and represent this information for the end users in a human understandable and effective way. There exist no explicit method how to solve this complex problem, and that is why it represents a big challenge for researchers and engineers.

One has to mention that through-wall imaging is much more problematic in comparison to detection or localization of moving objects behind the wall. Whereas, in moving objects detection background subtraction can be applied, what solves a lot of problems, this approach is not possible to apply. During imaging measurements where antenna system is moving and everything what is measured is background, and that is why it cannot be subtracted. Background subtraction eliminates influence of antennas, radar electronics, walls etc. on measured objects. Therefore, a calibration in imaging have to be done with a great precision because at the final stage it would significantly affects the results.

The radar imaging is well known field for a long time, mostly used for Ground Penetrating Radar (GPR) applications [76]. However, through-wall imaging has become investigated only a few years ago [60]. The most of the published methods were tested only on simulated data, and results from practical measurements are showing poor performance for most of them. Therefore, through-wall imaging has not found many applications that could be possibly used in the practical situations yet. A lot of research in signal processing as well as in radar hardware field is still required.

1.3 Thesis Organization

In Section 2, the state of the art of through-wall imaging is described. The function of an UWB radar is sketched, all the preprocessing and calibration steps required for through-wall imaging are explained, and simplified mathematical and physical ideas of most of the radar migration techniques are mentioned. In Section 3, the goals of this thesis are introduced. In Section 4, the three main contributions of this thesis are described. Efficient, precise and fast time of arrival through-wall estimation is shown in Section 4.1. Precise, easy to handle and fast measurement technique for estimation of wall parameters such as thickness, permittivity, and conductivity is introduced in Section 4.2. A method of building contours highlighting is presented in Section 4.3. Basic migration methods are compared in Section 4.4 on scenario measured with M-sequence UWB radar device. Also the imaging results of real measurements based on many practical scenarios are shown. Finally,

a contribution of this thesis and possible extensions of the research are proposed in Section 5.

1.4 Support of the Thesis

This thesis originated within the support of the project Ultra Wideband Radio application for localisation of hidden people and detection of unauthorised objects (Acronym: RADIOTECT) co-funded by the European Commission within the Sixth Framework Programme under the contract COOP-CT-2006-032744 [38], project Digital Processing of UWB Radar Signals (Acronym: DSP-UWB-RAD), and the Slovak Research and Development Agency under the contract No. LPP-0287-06.

Chapter 2

State Of The Art

2.1 UWB Radar Systems

2.1.1 History of Radar

Christian Huelsmeyer gave public demonstrations of the use of radio echoes to detect ships so that collisions could be avoided in Germany and the Netherlands in 1904. System consisted of a simple spark gap aimed using a multipole antenna. When a reflection was picked up by the two straight antennas attached to the separate receiver, a bell sounded. The system detected the presence of ships up to 3 km. It did not provide range information, only warning of a nearby metal object, and would be periodically "spun" to check for ships in bad weather. He patented the device, called the telemobiloscope, but due to lack of interest by the naval authorities the invention was not given into production [16]. Nikola Tesla proposed principles regarding frequency and power levels for primitive radar units in August 1917. Tesla proposed the use of standing electromagnetic waves along with pulsed reflected surface waves to determine the relative position, speed, and course of a moving object and other modern concepts of radar [94]. The World War II moved forward developing of airborne radars [22]. The next major development in the history of radars was the invention of the cavity magnetron by John Randall and Harry Boot of Birmingham University in early 1940's. This was a small device which generated microwave frequencies much more efficiently. The UWB term was at first used in the late 1960's Harmuth at Catholic University of America, Ross and Robbins at Sperry Rand Corporation and Paul van Etten at the USAF's Rome Air Development Center [13]. Till the end of 20th century there were lot of radar types for different applications like airborne radars, ground penetrating radars, sonars, and one which will be discussed further in detail the through-wall penetrating radar.

2.1.2 UWB Radar Fundamentals

A basic principle of the UWB radar is shown in Fig. 2.1.1. UWB radar generates and transmits short pulse through the transmit antenna TX. The signal propagates in an environment. When it meets target, the part of the electromagnetic energy is reflected from the object and propagates back to receive antenna RX. The time delay between the transmitted and received signal represents spatial distance between TX - target - RX.

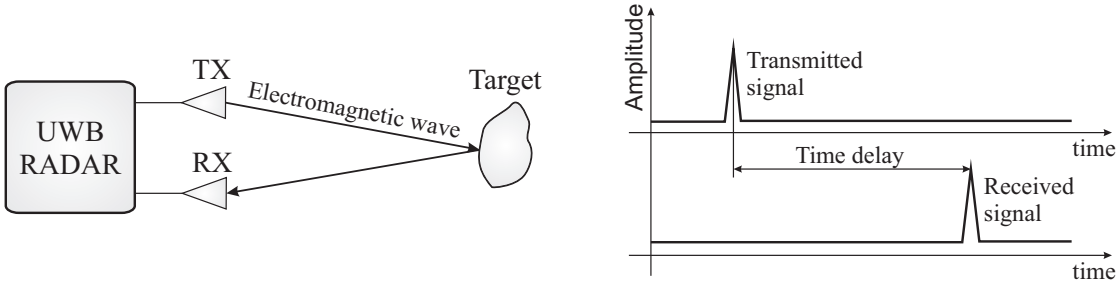

Fig. 2.1.1: Basic principle of the UWB radar.

There are many advantages why to use UWB radar instead of radars with continuos waves described in [74, 109]. To name just a few most important the UWB signal can be transmitted with no carrier, the produced transmit signal requires less power, improved range measurement accuracy and object identification (greater resolution), reduced radar effects due to passive interference (rain, mist, aerosols, metalized strips, ...), and many others.

2.1.3 M-sequence UWB Radar System

The UWB Maximum Length Binary Sequence (M-sequence) radar system [43, 116, 118, 111] with frequency band DC - 2.25 or 4.5 GHz is used for testing of all of the methods proposed in this work. The first idea to use a very well known M-sequence in UWB radar was proposed by Jürgen Sachs and Peter Peyerl, US patent No. 6272441 in 1996 [43]. The main advantages of using M-sequence radar instead of classical UWB radar are: the use of periodic signals avoids bias errors, it allows linear averaging for noise suppression, M-sequence has a low crest factor which allows to use limited dynamics of real systems and the signal acquisition may be carried out by undersampling. These signals of an extreme bandwidth may be sampled by using low cost, commercial Analog to Digital Converters (ADC) in combination with sampling gates.

The block diagram of the used M-sequence UWB radar system is shown in Fig. 2.1.2. The N-stage shift register generates the M-sequence which is transmitted via TX. The M-sequence reflected from a target is received by RX, undersampled,

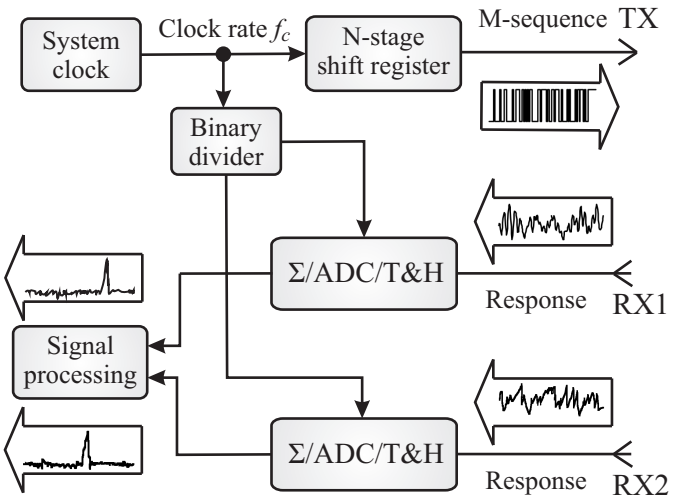

Fig. 2.1.2: Block diagram of M-sequence UWB radar system.

averaged, and correlated with the transmitted one. In principle, after the correlation, the output from the M-sequence radar system is the same as the output from a classic UWB pulse radar system. Therefore, the common signal processing techniques could be used after the data are gathered from radars. An analysis of 2 Dimensional (2D) target positioning accuracy for M-sequence UWB radar system under ideal conditions with the concentration on error caused by sampling with finite frequency we described in [2].

Two M-sequence UWB radars with number of chips $M = 511$ and clock frequency $f_{c1} = 4.5$ GHz or $f_{c2} = 9$ GHz are used for our experiment. One chip represents time interval between the two nearest impulses in M-sequence. M-sequence generator has $N = 7$ stages. For more information about M-sequence UWB radar see [43, 116, 118].

2.2 Through-Wall Radar Basic Model

Through-wall radar (TWR) basic model specifies all processes which contribute to the measured data. These processes are caused mainly by the measurement system, the measurement environment and partly also by measured objects. For description of this model TWR system with one RX and one TX stationary antenna is used.

Antenna signal effects would be shown for both, RX and TX antennas. The electric field which is generated by the TX antenna is called E^{rad} and could be modeled by [79, 125]:

$$E^{rad}(r,\theta,\varphi,n) = \frac{1}{2\pi rc} h_{TX}(\theta,\varphi,n) * \frac{\sqrt{Z_0}}{\sqrt{Z_c}} \frac{\Delta V_S(n)}{\Delta n} \tag{2.2.1}$$

Fig. 2.1.3: M-sequence UWB radar system. a) $f_{c2} = 9$ GHz b) $f_{c1} = 4.5$ GHz.

where r, θ, φ are spatial coordinates, and n is a discrete time, Z_c and Z_0 impedances of the feed cable and free space respectively, and c is the speed of light in vacuum. The voltage time evolution applied to the TX antenna is denoted $V_S(n)$, h_{TX} is the transfer function for the emitting antenna and $*$ represents the convolution. The received voltage from RX antenna V_R is then:

$$V_R(n) = \frac{\sqrt{Z_c}}{\sqrt{Z_0}} h_{RX}(\theta, \varphi, n) * E^{meas}(n) \tag{2.2.2}$$

where h_{RX} is the transfer function of the receiving antenna, and $E^{meas}(n)$ is the field at the RX antenna. $V_S(n)$ and $V_R(n)$ are scalars due to the fact that the antenna integrates all spatial components into one signal. The process that transforms E^{rad} into E^{meas} depends on the different travel signal paths and is denoted temporarily as an unknown impulse response $X(r, \theta, \varphi, n)$. The received voltage thus becomes:

$$V_R(n) = \frac{\sqrt{Z_c}}{\sqrt{Z_0}} h_{RX}(\theta, \varphi, n) * X(r, \theta, \varphi, n) * E^{rad}(r, \theta, \varphi, n). \tag{2.2.3}$$

If the $1/r$ dependency is taken out of the definition of E^{rad} all antenna terms could be combined into one term h_A:

$$V_R(n) = \frac{1}{r} h_A(\theta, \varphi, n) * X(r, \theta, \varphi, n). \tag{2.2.4}$$

h_A contains the contributions of the measurement system to the signal. It can be accurately measured only in lab conditions but it is very difficult and exacting challenge, that requires too precise measurements.

Antenna crosstalk effects means signal traveling directly from the transmitter to the receiver. This signal is thus constantly present in all the measurements

and shall remain constant for a fixed antenna setup. The impulse response of the direct path between both antennas will be expressed as C_A. The expression for the received field becomes:

$$V_R(n) = \frac{1}{d_{TX\,RX}} h_A(\theta, \varphi, n) * C_A + \frac{1}{r} h_A(\theta, \varphi, n) * X_1 \tag{2.2.5}$$

where X_1 represents the other (non-direct) paths between the antennas, and $d_{TX\,RX}$ is the direct distance between TX and RX. The first term can be measured (calibrated) by pointing the antenna system to the anechoic chamber room, so that X_1 becomes zero. It can thus be easily subtracted out of any measured data. The second term contains information about eventual target presence, and thus it is the most interesting one.

X_1 contains a combination of the impulse responses of target h_T and clutter h_C.

$$X_1 = h_T + h_C. \tag{2.2.6}$$

Here, targets are behind wall scatterers we want to detect, while clutter is anything else which adds misinformation to the signal. A typical clutter examples, presents in most of the measurements are the multiple reflections inside wall, multiple reflections between walls inside the room, multiple reflections between objects and walls or objects itself, non constant permittivity in wave propagation, moving trees in outside measurements, false objects received from behind antennas, etc. The model of the received signal (2.2.5) becomes:

$$V_R(n) = \frac{1}{d_{TX\,RX}} h_A(\theta, \varphi, n) * C_A(n) + \frac{1}{r} h_A(n) * (h_T(n) + h_C(n)) + noise. \tag{2.2.7}$$

The last term *noise* is added to represent measurement noise which is not added to the signal due to a reflection, but due to the measurement system itself.

Even if most of the variables in (2.2.7) could be measured, it is very difficult to measure them precisely. In practical measurements only $V_R(n)$ is measured what is summation of all these variables. This is the first source of systematic error.

One stationary measurement of $V_R(n)$ is the so called A-scan and represents impulse response of the measured environment including impulse response of the whole measurement system, clutters, noise, and systematic errors.

2.3 SAR Scanning

Only one impulse response from the whole environment is obtained in case when the antennas are stationary during measurements. In order to obtain more information about the investigated objects and to narrow antenna flaring angle beam, the Synthetic Aperture Radar (SAR) scanning is applied.

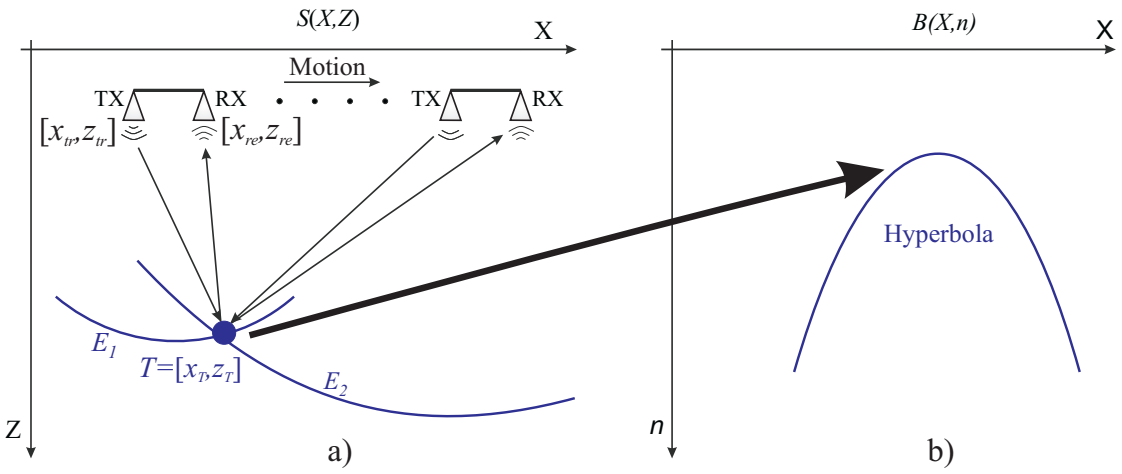

Fig. 2.3.1: a) 2D SAR spatial model. b) B-scan of one point.

The basic 2D SAR spatial model is shown in Fig. 2.3.1 a). A transmitted wave is reflected from the target to all directions uniformly. Because the antenna beam is wide, the signal reflected from the target is received not only when the antenna system is exactly over the target, but in a lot of positions that allow to "see" the target. This will cause that one point in $S(X, Z)$ space will be represented in an acquired B-scan $B(X, n)$ (set of A-scans assembled together in a 2D structure) as a hyperbola, as it is show in Fig. 2.3.1 b). The X is scanning direction and Z is looking direction.

2.4 Calibration and Preprocessing

There are several types of calibrations and preprocessing methods that help us to remove some unwanted artifacts from measured data. The most important are: oversampling in time domain, time zero estimation, crosstalk removing and deconvolution. Such signal processing methods affect the imaging results on a large scale. For example crosstalk does not contain any information about the scanned object and should be removed. Time zero estimation is very important for correct focusing measured hyperbolas back to the one point, which will be described in Section 2.5. An image of the investigated object would be blurred, if time zero estimation is incorrect even in a few chips. All of these calibration and preprocessing methods are applied individually to the A-scans.

2.4.1 Time Domain Interpolation

The measured B-scan $B(X, n)$ (Fig. 2.4.1 a)) is oversampled by the cubic spline interpolation [83] with an oversampling factor KO in the discrete time domain, so

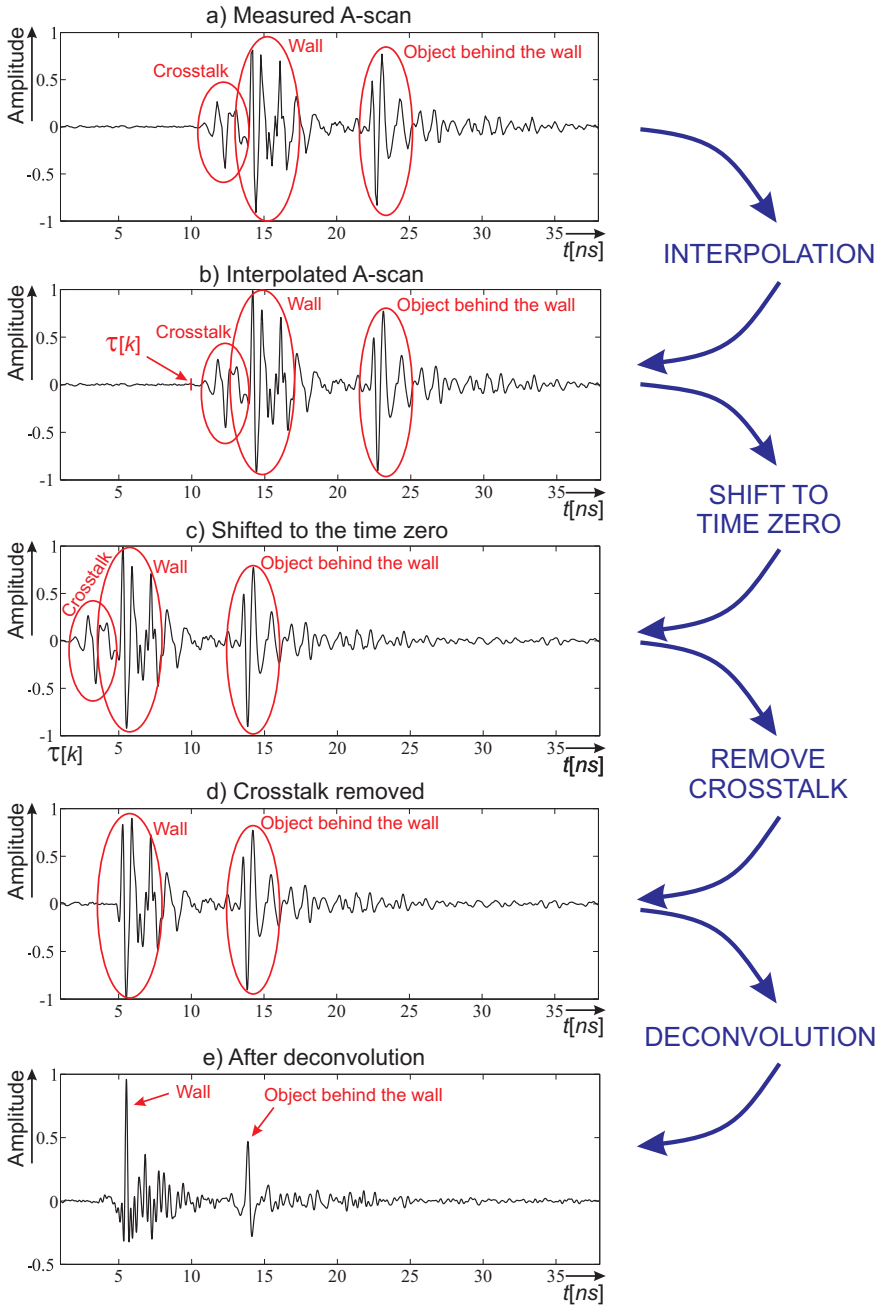

Fig. 2.4.1: Preprocessing and calibration steps: a) Measured A-scan. b) Interpolated A-scan. c) Shift to time zero. d) Crosstalk removed. e) After deconvolution.

the interpolated B-scan $B_s(X,k)$ is obtained (Fig. 2.4.1 b)):

$$B_s(X,k) = S_{pline}(B(X,n), KO), \quad k = nKO - KO + 1 \tag{2.4.1}$$

where S_{pline} is a cubic spline function and k is an oversampled discrete time. This step does not improve hardware resolution of the radar system, but could help to find crosstalk and time zero more precisely and slightly improve the image after migration (Section 2.5).

2.4.2 Time Zero Estimation

Time zero $\tau(k)$ is the time instant (or corresponding digitized sample) in which the transmitted signal leaves the transmit antenna. $B_s(X,k)$ has to be shifted, so that the $\tau(k)$ is at the beginning of the dataset (Fig. 2.4.1 c)).

$$B_{s\tau}(X,k) = B_s(X, k-\tau(k)). \tag{2.4.2}$$

In case of M-sequence radar the M-sequence is transmitted periodically around. The exact time at which the TX antenna starts emitting the first chip from M-sequence is time zero [79]. This time depends mostly on antennas cables lengths, antennas itself and radar hardware. Finding time zero in case of M-sequence radar means to rotate all the received impulse responses so that the first chip corresponds with spatial position of the TX antenna.

There are several methods how to find the $\tau(k)$. Most often the crosstalk signal $C_A(k)$ is used [149]. Since the geometry of antenna system is known, and the transmission medium of the crosstalk is air, the time needed for the signal to arrive from TX to RX can be easily estimated as:

$$t_{TX\,RX} = d_{TX\,RX}/c \tag{2.4.3}$$

where $d_{TX\,RX}$ is the known distance between the antennas. As can be seen in Fig. 2.4.1 a), the crosstalk has both a negative and a positive peak. The study [149] has shown that the best and most reliable part of the crosstalk response to estimate its position is the first peak. In principle, for determination of $\tau(k)$ whichever measured object can be used instead of crosstalk. Position in data that corresponded to the well known spatial position of object has to be found.

2.4.3 Antenna Crosstalk Removing

After the crosstalk $C_A(k)$ has been used to determine time zero, it may be removed out from the data. The crosstalk is the part of the signal that travels directly between the emitting and receiving antennas. It is the first and often the largest peak in the A-scan signal,thus its removal is really important. The crosstalk can be obtained by measuring with radar in the free space, or with absorbers around (anechoic chamber room). This reference measurement can be then subtracted from the data.

$$B_{s\tau c}(X,k) = B_{s\tau}(X,k) - C_A(k-\tau(k)). \tag{2.4.4}$$

Practically, it is very difficult to make a good quality crosstalk measurement. It can be done in anechoic chamber room like it is shown in Fig. 2.4.2 a). In this case the results are very close to ideal ones, but mostly they are useless. It is very difficult to transport the whole measurement setup including the antennas system and motion system that are necessary for SAR measurement into the anechoic chamber room without any mechanical changes in the setup. If even minor part of mechanical (mostly metal) setup changes within real measurement and anechoic chamber room measurement, the shape of the crosstalk changes too. The better results are mostly obtained when crosstalk measurement is done during real measurements with absolutely the same arrangement of the whole measurement system. However, in this case it is very difficult to find a "free space". The crosstalk measurement inside a building is shown in Fig. 2.4.2 b). It can be seen that lots of another artifacts like floor, roof, near walls etc. are present. Fig. 2.4.1 d) represents examples of data after the crosstalk has been removed.

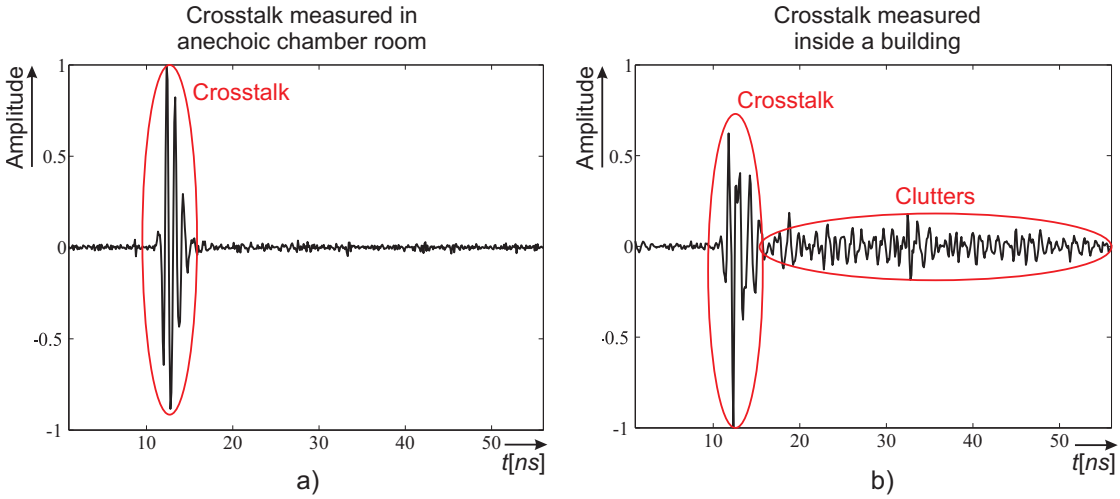

Fig. 2.4.2: Example of crosstalk measured a) in an anechoic chamber room with horn antennas b) inside a building with double-ridge horn antennas.

2.4.4 Deconvolution

An effort to remove influence of the antenna and the whole radar system impulse response to the measured data is the most complex calibration process. There exist lots of more or less complicated methods how to provide deconvolution described e.g. in [125, 123, 42, 126, 113, 11, 55]. Long impulse response of antenna causes that any object that reflects the wave energy and is received by RX is presented in data also in long area. Influence of the whole radar system, and mainly the antennas, to the received signal can be reduced by deconvolving the whole data with radar

impulse response $h_s(k)$:

$$B_P(X,k) = B_{s\tau c}(X,k) * h_s^{-1}(k). \tag{2.4.5}$$

This is time consuming process, mostly done in the frequency domain, and requiring lots of experience for adjusting many of the parameters when it is done manually. Therefore, there were made some automatic optimization processes [123, 42, 55], that reduced a need to manually adjust parameters and improved quality of the deconvolution.

An example of manually made antenna deconvolution is shown in Fig. 2.4.1 e). It can be seen that after deconvolution the main energy form front wall and metal plate behind the wall is concentrated in one peak, what improves imaging results.

In case the target is known (e. g. we are looking for special object behind the wall, or land mine problem), the impulse response of this target can be measured and then used for deconvolution. There are several methods [42] like optimum or least squares filtering, Wiener filtering, matched filtering, minimatched filtering, etc. which performances are compared in [112]. The selection of a suitable filter depends on the characteristics of the signal. As the sample data set is composed of signal, noise and clutter, the question of the stability of the filter must be considered. There are lots of mathematical optimization methods [42] how to propose a good solution.

2.4.5 Multiple Echoes Reducing

Multiple echoes or reverberations are very often produced in through-wall radars. They can occur as a result of reflections between the antenna and the wall, inside the wall, or within cables connecting the antennas to either the receiver or transmitter. The effect of these echoes can be considerably increased as a result of the application of time varying gain [42]. This can be easily appreciated by considering the case of an antenna spaced at distance W_{di} from the wall. Multiple reflections occur every $2W_{di}$ (twice the separation) and will decrease at a rate equal to the product of the wall reflection coefficient and the antenna reflection coefficient. This problem may be partially overcome by suitable signal processing algorithms which could be applied to the sampled time series output from either time domain or frequency domain radars. The general expectation is that all the individual reflections would be delayed at minimum. This expectation is generally reliable because most reflection coefficients are less than one, hence the more the impulse is reflected and re-reflected the more it is attenuated and delayed [42]. As a result, the energy is concentrated at the beginning of the train of wavelets. The easy way how to remove multiple reflections is by means of a filter on the form of:

$$F(k) = \frac{1}{1 + \alpha k^{en}}. \tag{2.4.6}$$

In essence, this filter subtracts a delayed (by en) and attenuated (by α) value of the primary wavelet from the multiple wavelet train at a time corresponding to the arrival of the first reflection.

An alternative method of resolving overlapping echoes is based on the use of the MUltiple SIgnal Characterization (MUSIC) algorithm [127, 32]. It is a high resolution spectral estimation method and is used to estimate the received signals covariance and then perform a spectral decomposition.

2.5 Radar Imaging Methods Overview

SAR scanning causes that one point in space domain $S(X, Z)$ is represented in B-scan $B(X, n)$ as a hyperbola, as it can be seen in Fig. 2.3.1. The main task of radar imaging methods is to focus hyperbolas from $B(X, n)$ back to the one point in $S(X, Z)$. By other words, the task of imaging is to transform time domain back into the depth domain, where depth means the coordination from antenna to the target (X-axes, looking direction). Such transformation is often called migration. The migration algorithms perform spatial positioning, focusing, and amplitude and phase adjustments to correct the effects of the spreading or convergence of raypaths as waves propagates. Most of the migration algorithms are based on a linearisation of the wave scattering problem. This means that the interactions of the field inside the scatterer and between different scatterers presented in the scene are neglected. This approximation is known from optic as the Born approximation [54, 26].

Most of basic imaging methods, e.g. like SAR were developed for airborne radar system, ground penetrating radar, tomography, seismology, or sound waves. They have undergone a long way of successive changes, improvements and adaptations for specific uses. This can cause confusion in terms, because they often changed their names but not the fundamentals or another methods acquired the same names. As a notable example the term "SAR" could be explained as: In airborne the SAR imaging process is mostly refereed to a synthesize of a very long antenna by combining signals received by the radar as it moves along its flight track and compensating Doppler effects [41]. On the other hand, in GPR is SAR imaging process mostly mentioned as convolving the observed data set with the inverse of the point target response [66]. In this work, the term SAR is associated with scanning (Section 2.3) as well as with imaging (Section 2.5.2).

2.5.1 Backprojection vs. Backpropagation

As the result of naming conflict, we will use terms backprojection and backpropagation in this work as follows. Backprojection is mostly associated with geometrically based methods. On the other hand, backpropagation is associated with wave

equations based methods. Very good subdivision of the basic imaging methods into these two categories is shown in [79].

- Backprojection Algorithms: This class of algorithms contains the conventional SAR imaging (geometrical migration) as well as simple migration algorithms as diffraction summation.
- Backpropagation Algorithms: This class of algorithms contains most migration algorithms (including the well known Kirchoff migration) as well as the wave equation based, non-conventional SAR.

The first migration methods are based on a geometrical approach. After the introduction of computers, more complex techniques based on the scalar wave equation were introduced. A good overview of these techniques is given in [150,17].

2.5.2 SAR Imaging - Geometrical Migration

In this Section a conventional SAR imaging with geometrically based bistatic migration will be described. All geometrically based imaging methods perform only spatial positioning and focusing. The amplitude and phase of the wave is not adjusted, because the wave equation is not taken into the account.

The basic 2D SAR bistatic spatial model is shown in Fig. 2.3.1 a). Time Of Arrival (TOA) is the time interval within the wave flying from transmitter to the target and from the target back to the receiver. For transmitter position $[x_{tr}, z_{tr}]$, receiver position $[x_{re}, z_{re}]$ and point target position $[x_T, z_T]$ TOA is given by the:

$$TOA = \frac{\sqrt{(x_{tr} - x_T)^2 + (z_{tr} - z_T)^2} + \sqrt{(x_T - x_{re})^2 + (z_T - z_{re})^2}}{v} \tag{2.5.1}$$

where v is velocity of the wave propagation. This holds for constant wave velocity, in case all the measurement environment is homogeneous. The measured and preprocessed signal $B_P(X, k)$ received in a given time can be reflected from all the points that lie on the locations where TOA is constant. The migration process that transforms preprocessed data set $B_P(X, k)$ back to the real spatial data $S(X, Z)$ can be computed in a measured scene $B_P(X, k)$, or in an image scene $S(X, Z)$. The second method is mostly used in praxis when the data are sampled. First of all, the spatial grid with specified resolution in the migrated image $I(X, Z)$ is created. Every point in $Bp(X, k)$ is gradually added to all the points that have the corresponding constant TOA in $I(x_T, z_T)$ for all antennas positions. One pixel in the migrated image is created as:

$$I(x_T, z_T) = \frac{1}{N} \sum_{n=1}^{N} B_{Pn}\left(X, k = TOA_n\right) \tag{2.5.2}$$

where N is the number of antennas positions during SAR scanning, $B_{Pn}(X, k = TOA_n)$ represents magnitudes of all the points for target position $[x_T, z_T]$ and antennas positions where TOA is constant. Theoretically this migration geometrically focuses hyperbolas from $B_P(X, k)$ into the one point in $S(X, Z)$. Of course, this is not an ideal approach and hence produces a lot of artifacts [96].

Conflict in names of basic imaging methods becomes evident in simple geometrical approach. This method is often called also back projection [140, 71, 78, 47, 87] or diffraction summation [98, 112, 96, 108, 99]. Moreover, this geometrical approach is often incorrectly called Kirchhoff migration [46, 35, 34, 153, 154].

2.5.3 Simple Wall Compensation

In through-wall imaging, the electromagnetic wave has to penetrate through the wall, reflect from the investigated object, and penetrate back through the wall to the receive antenna. The wave inside the wall will propagate with different velocity as in the air, because the wall has another permittivity, permeability, and conductivity. Wave diffraction and refraction will therefore occur on air-wall and wall-air interfaces as well as wave direction will change. A spatial model of the wave penetrating through the wall is shown in Fig. 2.5.1. The accurate calculation

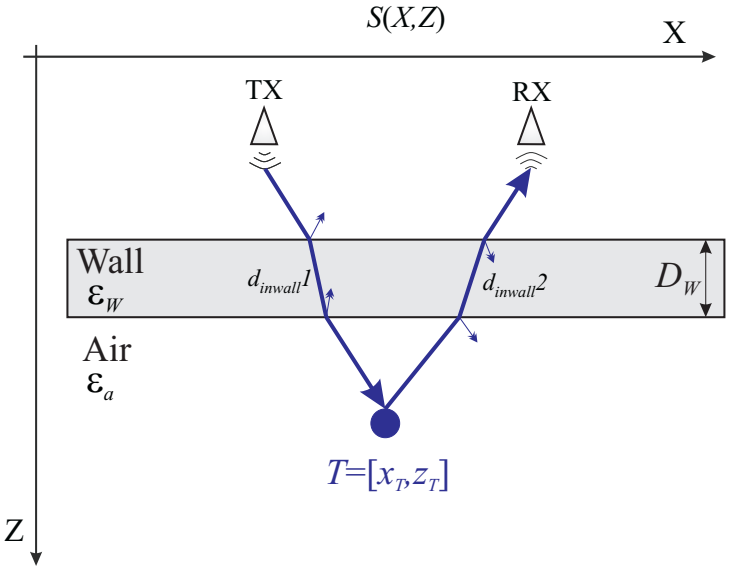

Fig. 2.5.1: Spatial model of the wave penetrating through the wall.

of the total flight time TOA is a critical step for through-wall imaging algorithms. The velocity of the signal inside the wall is slower as in the air what causes the longer flight time. There are several imaging methods that more or less precisely compensate the effect of wave penetrating through the wall [61, 60, 130, 89, 7, 9, 28,

30, 29, 31, 131, 39, 151, 44, 92]. Most of them present methods for computing d_{inwall}. Even if it looks like a simple task, it is a very complex problem that mostly requires huge computational power. In Section 4.1 we introduce an efficient, precise and fast method how to compute TOA for through the wall scenario.

Very simple, fast, but not too precise approximation for compensation of the wall effect is presented in [31]. Here, the time of flight of the wave inside a wall is given by:

$$t_{inwall} = \frac{d_{inwall}}{v_w} \tag{2.5.3}$$

where v_w is the velocity of the signal inside the wall. The approximation of the velocity inside the wall is related to the wall permittivity and permeability given by:

$$v_w \approx \frac{1}{\sqrt{\mu_w \varepsilon_w}} = \frac{1}{\sqrt{\mu_a \varepsilon_a \mu_{rw} \varepsilon_{rw}}} = \frac{c}{\sqrt{\mu_{rw} \varepsilon_{rw}}} \tag{2.5.4}$$

where μ_w and ε_w are the permeability and permittivity of the wall, μ_a and ε_a are the permeability and permittivity of the air, and μ_{rw} and ε_{rw} are the relative permeability and permittivity of the wall. For non-magnetic materials such as concrete or brick wall, the relative permeability $\mu_{rw} = 1$. Hence the velocity in non-magnetic wall is given by:

$$v_w = \frac{c}{\sqrt{\varepsilon_{rw}}} \tag{2.5.5}$$

and time in the wall by:

$$t_{inwall} = \frac{\sqrt{\varepsilon_{rw}} d_{inwall}}{c}. \tag{2.5.6}$$

With the assumption that the wave mostly penetrates perpendicularly to the wall, the approximation of d_{inwall} can be given by:

$$d_{inwall} \approx D_w \tag{2.5.7}$$

where D_w is thickness of the wall. Time delay caused by through-wall penetration is then expressed as comparison to through the air propagation:

$$t_{delay} = \frac{D_w}{v_w} - \frac{D_w}{c} = \frac{D_w}{c} \left(\sqrt{\varepsilon_{rw}} - 1 \right). \tag{2.5.8}$$

All impulse responses B_{Pn} should be shifted by t_{delay} before SAR imaging is applied. Including t_{delay} into the migration (2.5.2) partly compensates effect of the wall:

$$I(x_T, z_T) = \frac{1}{N} \sum_{n=1}^{N} B_{Pn} \left(X, k = (TOA_n + t_{delay}) \right). \tag{2.5.9}$$

The example of migrated image with and without simple wall compensation is shown in [31]. In general, the targets in compensated image are better focused as well as the positions of objects behind the wall are closer to the real positions.

2.5.4 Differential SAR

The wall is mostly represented in a long area of the migrated image. Sometimes the objects behind the wall are overlapped by the wall reflection. Differential SAR (DSAR) is a method for elimination of direct reflection from the walls proposed by Mojtaba Dehmollaian et al. [45] in 2009. The idea is similar to applying background subtraction for detection of moving objects behind the wall. Although during SAR scanning all the scanned objects seems to move, the reflection from the first wall is almost the same for two successive antenna positions. However, the reflection from the object behind the wall is not the same, as it can be seen in Fig. 2.5.2. Before the SAR imaging is applied, the matrix of difference signal is

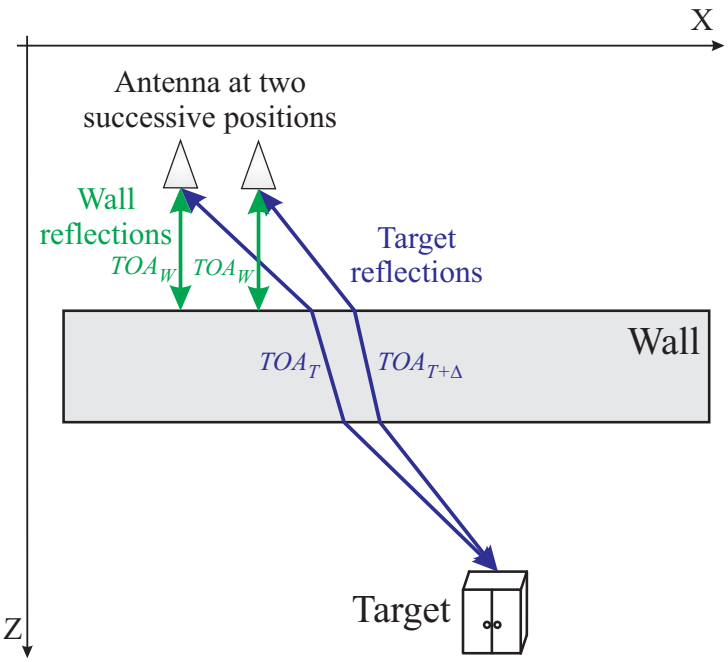

Fig. 2.5.2: Differential SAR model for monostatic approach.

obtained by substracting two successive impulse responses:

$$B_\Delta = V_R(n+1) - V_R(n). \tag{2.5.10}$$

Computing the SAR image with B_Δ leads to elimination of direct reflection from the first wall. This can increase a signal-to-clutter ratio of small objects behind the wall. The wall has to be homogenous and scan has to be performed in parallel to the wall in order to obtain the same wall reflection in two successive antenna positions.

2.5.5 Kirchhoff Migration

Kirchhoff migration is based on solving scalar wave equation. Partial differential equations called separation of variables based on Green's theorem are used to solve this scalar wave equation [96]. Kirchhoff migration theory provides a detailed prescription for computing the amplitude and phase along the wavefront, and in variable velocity, the shape of the wavefront. Kirchhoff theory shows that the summation along the hyperbola must be done with specific weights. In this case, the hyperbola is replaced by a more general shape.

Kirchhoff migration is mathematically complicated algorithm and is described in depth in e.g. [96] and [150] and applied for landmine detection e.g. in [57]. In this section, only a short overview of mathematical description from [96] with focus on physical interpretation of the method is explained.

Gauss's theorem [59] and Green's theorem [23] is used for Kirchhoff migration description. Gauss's theorem generalizes the basic integral result (2.5.11) into the more dimensions (2.5.12).

$$\int_a^b \phi'(x)dx = \phi(x)\Big|_a^b = \phi(b) - \phi(a) \tag{2.5.11}$$

$$\int_V \vec{\nabla}.\vec{A}dvol = \oint_{\partial V} \vec{A}.\vec{n}dsurf \tag{2.5.12}$$

where $\vec{n}$ is the outward pointing normal to the surface ($surf$) ∂V bounding the integration volume (vol) V (Fig. 2.5.3). $\vec{A}$ is a vector function that might physically represent electric field. $\vec{\nabla}.\vec{A}$ denotes the divergence of $\vec{A}$. In many important

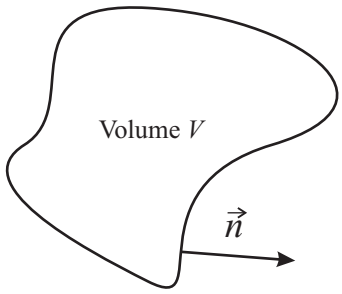

Fig. 2.5.3: Volume vector and normal to the bounding surface.

cases, the vector function $\vec{A}$ can be calculated as a gradient of a scalar potential $\vec{A} = \vec{\nabla}\phi$. In this case, Gauss's theorem becomes:

$$\int_V \nabla^2\phi dvol = \oint_{\partial V} \frac{\partial\phi}{\partial n}dsurf \tag{2.5.13}$$

where $\nabla^2\phi = \vec{\nabla}.\vec{\nabla}\phi$ and $\frac{\partial\phi}{\partial n} = \vec{\nabla}\phi.\vec{n}$. In the case when $\phi = \phi_1\phi_2$, the $\phi' = \phi_2\phi_1' + \phi_1\phi_2'$ and (2.5.11) becomes:

$$\int_a^b [\phi_2\phi_1' + \phi_1\phi_2']dx = \phi_1\phi_2\big|_a^b \tag{2.5.14}$$

or

$$\int_a^b \phi_2\phi_1' dx = \phi_1\phi_2\big|_a^b - \int_a^b \phi_1\phi_2' dx. \tag{2.5.15}$$

An analogous formula in higher dimensions arises by substituting $A = \phi_2\vec{\nabla}\phi_1$ into (2.5.12). Using the identity $\vec{\nabla}.a\vec{\nabla}b = \vec{\nabla}a.\vec{\nabla}b + a\nabla^2 b$ leads to:

$$\int_V \Big[\vec{\nabla}\phi_2.\vec{\nabla}\phi_1 + \phi_2\nabla^2\phi_1\Big]dvol = \oint_{\partial V} \phi_2\frac{\partial\phi_1}{\partial n}dsurf. \tag{2.5.16}$$

Similar result can be obtained when $A = \phi_1\vec{\nabla}^2\phi_2$:

$$\int_V \Big[\vec{\nabla}\phi_1.\vec{\nabla}\phi_2 + \phi_1\nabla^2\phi_2\Big]dvol = \oint_{\partial V} \phi_1\frac{\partial\phi_2}{\partial n}dsurf. \tag{2.5.17}$$

Finally, subtracting (2.5.17) from (2.5.16) yields to:

$$\int_V \big[\phi_2\nabla^2\phi_1 - \phi_1\nabla^2\phi_2\big]dvol = \oint_{\partial V} \left[\phi_2\frac{\partial\phi_1}{\partial n} - \phi_1\frac{\partial\phi_2}{\partial n}\right]dsurf. \tag{2.5.18}$$

(2.5.18) is known as Green's theorem that represents fundamental of the Kirchhoff migration theory. It is a multidimensional generalization of the integration by formula from elementary calculus and is valuable for its ability to solve certain partial differential equation. ϕ_1 and ϕ_2 in (2.5.18) may be chosen as desired to conveniently expressed solutions to a given problem. Typically, in the solution to a partial differential equation like the wave equation, one function is chosen to be the solution to the problem at hand and the other is chosen to be the solution to the more simple reference problem. The reference problem is usually selected to have a known analytic solution and this solution is called a Green's function [96].

In general, the scalar wavefield ψ is a solution to the Helmholtz scalar wave equation:

$$\left(\nabla^2 + k^2\right)\psi = 0 \tag{2.5.19}$$

where ∇^2 is the Laplacian and k is the wavevector. When the wave travels through the medium from point x_0 to the point x this Helmholtz scalar wave equation can be expressed with the aid of Green's function $G(x_0, x)$ as:

$$\left(\nabla^2 + k^2\right)G(x_0, x) = \delta(x_0 - x) \tag{2.5.20}$$

where the $\delta(x_0 - x)$ is a Dirac delta function. The Green's function describes how the wave changes during travel from point x_0 to the point x.

Kirchhoff diffraction integral can be derived as follows. Let ψ be a solution to the scalar wave equation:

$$\nabla^2 \psi(x,t) = \frac{1}{v^2} \frac{\partial^2 \psi(x,t)}{\partial^2 t} \tag{2.5.21}$$

where $\psi(x,t)$ is a wave function, v is the wave velocity and do not has to be a constant. When Green's theorem from (2.5.18) is applied to the (2.5.21) with the aid of Helmholtz equation, Hankel functions, and good mathematical skills (the complete process can be find in [96]) the Kirchhoff's diffraction integral can be obtained:

$$\psi(x_0,t) = \oint_{\partial V} \left[\frac{1}{r} \left[\frac{\partial \psi}{\partial n} \right]_{t+r/v_0} - \frac{1}{v_0 r} \frac{\partial r}{\partial n} \left[\frac{\partial \psi}{\partial t} \right]_{t+r/v_0} + \frac{1}{r^2} \frac{\partial r}{\partial n} [\psi]_{t+r/v_0} \right] dsurf \tag{2.5.22}$$

where $r = |x - x_0|$, x_0 is the source position and v_0 is a constant velocity. In many cases this integral is derived for forward modeling with the result that all of the terms are evaluated at the retarded time $t - r/v_0$ instead of the advanced time. This Kirchhoff diffraction integral expresses the wavefield at the observation point x_o at time t in terms of the wavefield on the boundary ∂V at the advanced time $t + r/v_0$. It is known from Fourier theory that knowledge of both ψ and $\partial_n \psi$ is necessary to reconstruct the wavefield at any internal point.

In order to obtain practical migration formula, two essential tasks are required. First, the apparent need to know $\partial_n \psi$ must be addressed. Second, the requirement that the integration surface must extend all the way around the volume containing the observation point must be dropped. There are various ways how to fulfill both of these arguments. Schneider [128] solved the requirement of $\partial_n \psi$ by using a dipole Green's function with an image source above the recording place, that vanished at $z = 0$ and cancelled the $\partial_n \psi$ term in (2.5.22). Wiggins in [143] adapted Schneider's technique to rough topography. Docherty in [51] showed that a monopole Green's can also leads to an acceptable result and once again challenged Schneider's argument, so the integral over the infinite hemisphere could be neglected. After all, migration by summation along diffraction curves or by wavefront superposition has been done for many years. Though Schneider's derivation has been criticized, his final expressions are considered correct.

As a first step in adapting (2.5.22) it is usually considered as appropriate to discard the term 1 $\frac{1}{r^2} \frac{\partial r}{\partial n} [\psi(x)]_{t+r/v_0}$. This is called the near-field term and decays more strongly with r than the other two terms. Then, the surface $S = \partial V$ will be taken as the $z = 0$ plane, S_0, plus the surface infinitesimally below the reflector, S_z, and finally these surfaces will be joined at infinity by vertical cylindrical walls, S_∞,

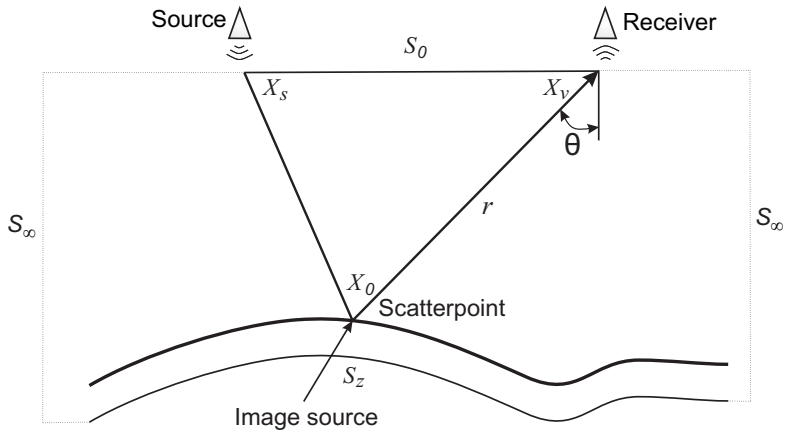

Fig. 2.5.4: The geometry of Kirchhoff migration [96].

as it is shown in Fig. 2.5.4 - the geometry of Kirchhoff migration. The integration surface consists from $S_0 + S_z + S_\infty$, but only S_0 contributes meaningfully to the estimation of the backscattered field at vx_0. S_∞ could never be realized due to finite aperture limitations and its neglection may introduce unavoidable artifacts. With these considerations, (2.5.22) becomes:

$$\psi(x_0,t) = \oint_{S_0} \left[\frac{-1}{r} \left[\frac{\partial \psi}{\partial z} \right]_{t+r/v_0} + \frac{1}{v_0 r} \frac{\partial r}{\partial z} \left[\frac{\partial \psi}{\partial t} \right]_{t+r/v_0} \right] dsurf \tag{2.5.23}$$

where the signs on the terms arise because $\vec{n}$ is the outward normal and z is increasing downward so that $\partial n = -\partial z$.

Now, $\partial_z \psi$ must be evaluated. Fig. 2.5.4 shows the source wavefield being scattered from the reflector at x_0 which is called the scatterpoint. A simple model for ψ is that it is approximately the wavefield from a point source placed at the image source location that passes through the scatterpoint to the receiver. This can be expressed as:

$$\psi(x,t) \sim \frac{1}{r} A\left(t - r/v\right) = \frac{[A]_{t-r/v}}{r} \tag{2.5.24}$$

where $A(t)$ is the source waveform at the scatterpoint. Using the chain rule, applying near-field term, and doing substitution into (2.5.23) the result is obtained:

$$\psi(x_0,t) = \oint_{S_0} \frac{2}{vr} \frac{\partial r}{\partial z} \left[\frac{\partial \psi}{\partial t} \right]_{t+r/v_0} dsurf \tag{2.5.25}$$

where $v = v_0$. Since $r = \sqrt{(x-x_0)^2 + (y-y_0)^2 + (z-z_0)^2}$, the $\partial_z \psi$ can be written as:

$$\frac{\partial r}{\partial z} = \frac{\partial}{\partial z} \sqrt{(x-x_0)^2 + (y-y_0)^2 + (z-z_0)^2} = \frac{z}{r} = \cos\theta \tag{2.5.26}$$

where θ is the vertical angle between the receiver location and the ray to the scatterpoint. With this, the final formula for the scattered wavefield just above the reflector is:

$$\psi(x_0,t) = \oint_{S_0} \frac{2\cos\theta}{vr} \left[\frac{\partial\psi}{\partial t}\right]_{t+r/v} dsurf. \tag{2.5.27}$$

The fact that (2.5.27) is a form of direct wavefield extrapolation, but not recursive is the reason why it is not yet a migration equation. A migration equation has to estimate reflectivity, not just the scattered wavefield, and for this purpose a model relating the wavefield to the reflectivity is required. The most simple model is the exploding reflector model [93] which asserts that the reflectivity is identical to the downward continued scattered wavefield at $t = 0$ provided that the downward continuation is done with $v = v/2$. Thus, a wave migration equation follows immediately from equation (2.5.27) as:

$$\psi(x_0,0) = \oint_{S_0} \frac{2\cos\theta}{vr} \left[\frac{\partial\psi}{\partial t}\right]_{r/v} dsurf = \oint_{S_0} \frac{4\cos\theta}{vr} \left[\frac{\partial\psi}{\partial t}\right]_{2r/v} dsurf. \tag{2.5.28}$$

Finally, (2.5.28) is the Kirchhoff migration equation. This result was derived by many authors including Schneider [128] and Scales [124]. It expresses migration by summation along hyperbolic travel paths through the input data space. The hyperbolic summation does not have to be seen at the first view, but it can be indicated by $[\partial_t\psi]_{2r/v}$, notation means that partial derivation is to be evaluated at the time $2r/v$. $\partial_t\psi\,(x,t)$ is integrated over the $z = 0$ plane, only those specific traveltimes values are selected by:

$$t = \frac{2r}{v} = \frac{2\sqrt{(x-x_0)^2 + (y-y_0)^2 + (z-z_0)^2}}{v} \tag{2.5.29}$$

which is the equation of a zero-offset diffraction hyperbola.

In addition to diffraction summation, (2.5.28) requires that the data be scaled by $4cos\theta/(vr)$ and that the time derivative be taken before summation. These additional details were not indicated by the simple geometric theory in Section 2.5.2 and are major benefits of Kirchhoff theory. The same correction procedures are contained implicitly in f-k migration that will be described in Section 2.5.6. Kirchhoff migration is one of the most adaptable migration schemes available. It can be easily modified for account of such difficulties as topography, irregular recording geometry, pre-stack migration, converted wave imaging as well as through-wall imaging. Computational cost is one of the biggest disadvantages of this method.

2.5.6 f-k Migration

Wave equation based migration could be done also in the frequency domain. Stolt in 1978 showed that migration problem could be solved by Fourier transform [133].

The basic principle for 2D problem is described. Complete mathematical solution is derived in [133] or in [96], therefore only the basic relations and principles from [96] of the method is shown in this work.

Scalar wavefield $\psi(x, z, t)$ is a solution to:

$$\nabla^2\psi - \frac{1}{v^2}\frac{\partial^2\psi}{\partial t^2} = 0 \tag{2.5.30}$$

where v is the constant wave velocity. It is desired to compute $\psi(x, z, t = 0)$ given knowledge of $\psi(x, z = 0, t)$. The wavefield can be written as an inverse Fourier transform of its (k_x, f) spectrum as:

$$\psi(x, z, t) = \iint \phi(k_x, z, f)\, e^{2\pi i(k_x x - ft)} dk_x df \tag{2.5.31}$$

where k_x is a horizontal wavenumber, cyclical wavenumbers and frequencies are used and the Fourier transform convention uses a + sign in the complex exponential for spatial components $(k_x x)$ and a − sign for temporal components (ft). By substituting (2.5.31) into (2.5.30) and providing some mathematical tricks [96] it can be obtained:

$$\iint \left\{ \frac{\partial^2\phi(z)}{\partial z^2} + 4\pi^2 \left[\frac{f^2}{v^2} - k_x^2 \right] \phi(z) \right\} e^{2\pi i(k_x x - ft)} dk_x df = 0. \tag{2.5.32}$$

If v is constant, then the left-hand-side of (2.5.32) is the inverse Fourier transform of the term in curly brackets. From Fourier theory it is known that if signal in one domain is zero than also in another domain it would be zero. This results to:

$$\frac{\partial^2\phi(z)}{\partial z^2} + 4\pi^2 k_z^2 \phi(z) = 0 \tag{2.5.33}$$

where the vertical wavenumber k_z is defined by

$$k_z^2 = \frac{f^2}{v^2} - k_x^2. \tag{2.5.34}$$

(2.5.33) and (2.5.34) are a complete reformulation of the problem in the (k_x, f) domain. The boundary condition is now $\phi(x, z = 0, t)$ which is the Fourier transform, over (x, t), of $\psi(x, z, t)$. (2.5.33) is a second-order differential equation with exact solution $e^{\pm 2\pi i k_z z}$, Thus the unique solution can be written by substitution:

$$\phi(k_x, z, f) = A(k_x, f)\, e^{2\pi i k_z z} + B(k_x, f)\, e^{-2\pi i k_z z} \tag{2.5.35}$$

where $A(k_x, f)$ and $B(k_x, f)$ are arbitrary functions of (k_x, f) to be determined from the boundary condition(s). The two terms on the right-hand-side of (2.5.35) have the interpretation of a downgoing wavefield, $A(k_x, f)\, e^{2\pi i k_z z}$, and an upgoing

wavefield, $B\left(k_x, f\right) e^{-2\pi i k_z z}$. Downgoing means in z direction and upgoing in $-z$ direction.

It is now apparent that only one boundary condition $\phi\left(x, z=0, t\right)$ is not enough and the solution will be ambiguous. To remove this ambiguity, the two boundary conditions are required, for example ψ and $\partial_z \psi$. But this is not known in our case so the migration problem is said to be ill-posed and another trick has to be used. If both conditions were available, A and B would be found as solutions to ϕ for $z = 0$ and it would be specified as ϕ_0 as well as $\partial\phi/\partial z$ would be specified as ϕ_{z0}:

$$\phi(z=0) \equiv \phi_0 = A + B \tag{2.5.36}$$

and

$$\frac{\partial \phi}{\partial z}(z=0) \equiv \phi_{z0} = 2\pi i k_z A - 2\pi i k_z B. \tag{2.5.37}$$

The solution for this ill-posed problem and ambiguity removing will be done by assumption of one-way waves. In the receiver position, the wave cannot be downgoing, only upgoing. This allows the solution:

$$A(k_x, f) = 0 \quad \textit{and} \quad B(k_x, f) = \phi_0(k_x, f) \equiv \phi(k_x, z=0, f). \tag{2.5.38}$$

Then, the wavefield can be expressed as the inverse Fourier transform of ϕ_0:

$$\psi(x, z, t) = \iint \phi_0(k_x, f) e^{2\pi i(k_x x - k_z z - ft)} dk_x df \tag{2.5.39}$$

and the migrated solution is:

$$\psi(x, z, t=0) = \iint \phi_0(k_x, f) e^{2\pi i(k_x x - k_z z)} dk_x df. \tag{2.5.40}$$

(2.5.40) gives a migration process as a double integration of $\phi_0(k_x, f)$ over f and k_x. Even if it looks like the solution is complete, it has a disadvantage. Only one of the integrations, that over k_x, is a Fourier transform that can be done by a numerical fast Fourier Transform (FFT). The f integration is not a Fourier transform because the Fourier kernel $e^{-2\pi f t}$ was lost when the imaging condition (setting t = 0) was invoked. However, another complex exponential $e^{-2\pi i k_z z}$ shows up in (2.5.40). Stolt suggested a change of variables from (k_x, f) to (k_x, k_z) to obtain a result in which both integrations are Fourier transforms. The change of variables is defined by (2.5.34) and can be solved for f to give:

$$f = v\sqrt{k_x^2 + k_z^2}. \tag{2.5.41}$$

Performing the change of variables from f to k_z according to the rules of calculus transforms (2.5.40) yields into:

$$\psi(x, z, t=0) = \iint \phi_m(k_x, k_z) e^{2\pi i(k_x x - k_z z)} dk_x dk_z \tag{2.5.42}$$

where

$$\phi_m(k_x, k_z) \equiv \frac{\partial f(k_z)}{\partial k_z}\phi_0(k_x, f(k_z)) = \frac{vk_z}{\sqrt{k_x^2 + k_z^2}}\phi_0(k_x, f(k_z)). \tag{2.5.43}$$

(2.5.42) is Stolts expression for the migrated section and forms the basis for the f-k migration algorithm. The change of variables reformed the algorithm into one that can be accomplished with FFTs. (2.5.43) results from the change of variables and is a prescription for the construction of the (k_x, k_z) spectrum of the migrated section from the (k_x, f) spectrum of the measured data.

In Fig. 2.5.5, the same examples of transformation from (k_x, k_z) to $(k_x, f/v)$ space and vice versa are shown. The v is a constant wave velocity. This geo-

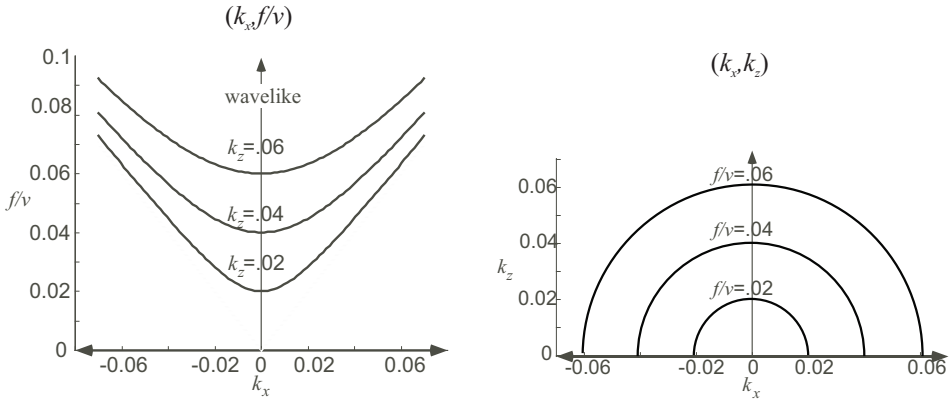

Fig. 2.5.5: Comparison of $(k_x, f/v)$ space - left side, with (k_x, k_z) space - right side, [96]

metric relationships between (k_x, k_z) and $(k_x, f/v)$ can be explained as follows: In $(k_x, f/v)$ space, the lines of constant k_z are hyperbolas that are asymptotic to the dashed boundary. They are transformed into the (k_x, k_z) space like curves of constant f/v - semi-circle and vice versa. At $k_x = 0$ and $k_z = f/v$ these hyperbolas and semi-circles intersect, in case the plots are superimposed. Conceptually, it can also be viewed as a consequence of the fact that the (k_x, f) and the migrated section must agree at $z = 0$ and $t = 0$.

On a numerical dataset, this spectral mapping is the major complexity of the Stolt algorithm. Generally, it requires an interpolation in the (k_x, f) domain since the spectral values that map to grid nodes in (k_x, k_z) space cannot be expected to come from grid nodes in (k_x, f) space. In order to achieve significant computation speed that is considered the strength of the Stolt algorithm, it turns out that the interpolation must always be approximate. This causes artifacts in the final result [96]. The creation of the migrated spectrum also requires that the spectrum be scaled by $vk_z/\sqrt{k_x^2 + k_z^2}$ like it is shown in (2.5.43). The steps of Stolt migration

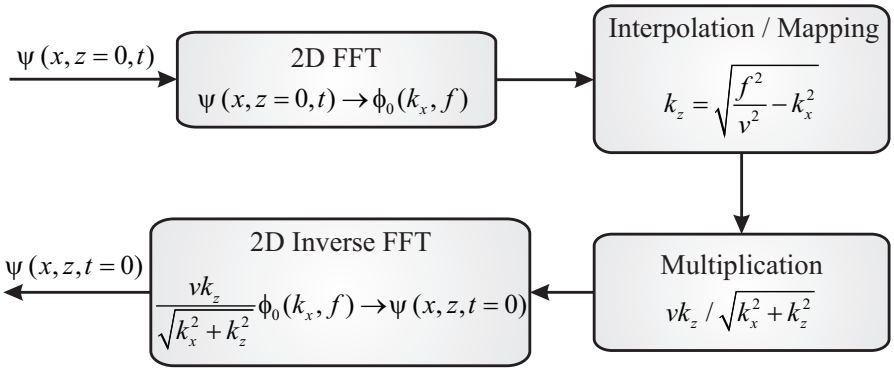

Fig. 2.5.6: Implementation of Stolt migration.

in blocks for practical implementation are shown in Fig. 2.5.6. The measured data in time domain at receiver position $\psi(x, z = 0, t)$ are transformed into the frequency domain by 2D FFT. k_x is interpolated and mapped into the k_z. k_z is multiplied by $v/\sqrt{k_x^2 + k_z^2}$ and transformed back into the time domain by inverse FFT. The result $\psi(x, z, t = 0)$ at time $t = 0$ is obtained.

The f-k migration algorithm, which has been just described, is limited to constant velocity. Its use of Fourier transforms for all of the numerical integrations means that it is computationally very efficient.

Stolt provided an approximate technique to adapt f-k migration to non constant wave velocity $v(z)$. This method used a pre-migration step called the Stolt stretch, and after this step follows classical f-k migration. The idea was to perform a one-dimensional time-to-depth conversion with $v(z)$ and then convert back to a pseudo time with a constant reference velocity. The f-k migration is then performed with this reference velocity. Stolt developed the time-to-depth conversion to be done with a special velocity function derived from $v(z)$ called the Stolt velocity. This method is now known to progressively lose accuracy with increasing dip and has lost favor. A technique that could handle this problem more precisely is the phase-shift method of Gazdag and is described in [62]. Unlike the direct f-k migration, phase shift is a recursive algorithm that processes $v(z)$ as a system of constant velocity layers. In the limit when layer thickness is going to be infinitely small, any $v(z)$ variation could be modeled. This method has quite complicated geometric and long mathematically representation that is very precisely described by the author of the idea in [62] and really user-friendly described in [96]. How does it work for one layer will be described in this work.

The method can be derived starting from (2.5.39). Considering the first velocity layer only, this result is valid for any depth within that layer provided that v is replaced by the first layer velocity, v_1. If the thickness of the first layer is Δz_1, then the wavefield just above the interface between layers one and two can be written

as

$$\psi(x, z = \Delta z_1, t) = \iint \phi_0(k_x, f) e^{2\pi i(k_x x - k_{z1}\Delta z_1 - ft)} dk_x df \tag{2.5.44}$$

where

$$k_{z1} = \sqrt{\frac{f^2}{v_1^2} - k_x^2}. \tag{2.5.45}$$

(2.5.44) is an expression for downward continuation or extrapolation of the wavefield to the depth Δz_1. The wavefield extrapolation expression in (2.5.44) is more simply written in the Fourier domain to suppress the integration that performs the inverse Fourier transform:

$$\phi(k_x, z = \Delta z_1, f) = \iint \phi_0(k_x, f) e^{2\pi i k_{z1}\Delta z_1} dk_x df. \tag{2.5.46}$$

Now consider a further extrapolation to estimate the wavefield at the bottom of the layer two ($z = \Delta z_1 + \Delta z_2$). This can be written as:

$$\phi(k_x, z = \Delta z_1 + \Delta z_2, f) = \phi(k_x, z = \Delta z_1, f) T(k_x, f) e^{2\pi i k_{z2}\Delta z_2} \tag{2.5.47}$$

where $T(k_x, f)$ is a correction factor for the transmission loss endured by the wave as it crossed from layer two into layer one.

If this method want to be applied in praxis, phase shift algorithm [96] would have to be studied into more depth in order to prevent many of unwanted effects and incorrect implementations.

The Fourier method discussed in this section is based upon the solution of the scalar wave equation using Fourier transforms. Though Kirchhoff methods seem superficially quite different from Fourier methods, the uniqueness theorems from partial differential equation theory guarantee that they are equivalent [96]. However, this equivalence only applies to the problem for which both approaches are exact solutions to the wave equation and that is the case of a constant velocity medium, with regular wavefield sampling. In all other cases, both methods are implemented with differing approximations and can give very distinct results. Furthermore, even in the exact case, the methods have different computational artifacts [96].

2.5.7 Improvements in f-k Migration

f-k migration obtained title of the most often used migration method in praxis due to its fast computation and very precise image results. A lot of improvements and modifications have been done in f-k migration. They are mostly described in airborne, or GPR scenarios. The most important of them will be shortly described in this section.

Nonuniform FFT

NonUniform Fast Fourier Transformation (NUFFT) [53,19,91] is based on classical Stolt migration for non equally spaced data. Stolt migration requires equally spaced input data for FFT algorithms. In many practical situations, however, the input data is nonuniform (i.e., not equally spaced). That is why the regular FFT can not be applied. NUFFT proposes an approach to achieve the fast Fourier transform for the nonuniform data by using the another class of matrices, the regular Fourier matrices [105]. This algorithm with the same complexity like Stolt migration is more accurate, because an approximation error is minimized in the leastsquare sense. Stolt migration requires so called Stolt interpolation which is cumbersome and reduces the computational efficiency of the Stolt algorithm. NUFFT does not require Stolt interpolation. NUFFT firstly compute Fourier coefficients usage of regular Fourier matrices. The uniform FFT is computed and results are scaled back into the nonuniform space. The mathematical background is described in depth e.g. in [91]. A nice review of more NUFFT methods in comparison to classical f-k migration tested on simulated data is shown in [135].

f-k Migration in Cylindrical Coordinations

f-k migration transformed into the cylindrical coordinate system is described in [70]. A three-dimensional, frequency-domain imaging algorithm for cylindrical geometry is obtained by making suitable approximations to the point spread function for wave propagation in cylindrical coordinates. Its Fourier transform is obtained by analogy with the equivalent problem in Cartesian coordinates. The focus is treated as a diverging source by the imaging algorithm, which then forms images on deeper cylindrical shells. Computer simulations and experimental results using wire targets show that this imaging technique attains the resolution limit dictated by the operating wavelength and the transducer characteristics.

f-k Migration with Motion Compensation

f-k migration with integrated motion compensation for airborne measurements is described in [110]. Wavenumber-domain processing is limited because of its inability to perform high-precision motion compensation. Extended Chirp Scaling (ECS) [100] algorithm has proven to be very powerful, although it has certain limitations concerning long aperture syntheses and highly squinted geometries. Analytically derived new stripmap SAR data processing algorithm is described, called Extended ωk (EOK). The EOK algorithm aims to combine the high focusing accuracy of the wavenumber domain algorithm with the high precision motion compensation of the ECS algorithm. The EOK algorithm integrates a three step motion compensation correction in the general formulation of the wavenumber-domain algorithm. It leads to a new airborne SAR processing scheme, which is

also very robust in the cases of long synthetic apertures and high squint angles. It offers the possibility of processing wide-band, low-frequency airborne SAR data up to near wavelength resolution.

f-k Migration with Ground Surface and Non Loss-Free Compensation

Standard f-k migration assumes that the ground surface is flat and the medium is loss-free which in reality is not true. Xiaoyin Xu et al. in [146] adapted it to rough ground surface and lossy medium. When implemented in the Fourier domain, the wave equation becomes the Helmholtz equation. It is then straight-forward to incorporate a complex index of refraction in the Helmholtz equation to describe wave phenomenon in lossy medium [49]. Here the f-k migration is generalized to the case of rough ground surface and lossy medium. In the framework of Tikhonov regularization [55], [85], an algorithm was developed that optimally alters the wave propagation velocity and the complex index of refraction to take into account of the ground roughness and lossy medium. In the process of searching the optimal velocity and complex index of refraction, the algorithm is constrained to produce an image of minimum entropy. By minimizing the entropy of the resulting image, better results are obtained in terms of enhanced mainlobe, suppressed sidelobes, and reduced noise.

Prestack Residual f-k Migration

Prestack residual migration in the frequency domain was introduced by Paul C. Sava in [122]. This method has advantages over classical f-k migration that estimates interval velocity functions for depth migration. It is more accurate than methods which are based on focusing the stack of migrated images, so it provides a more accurate estimate of the correct migration velocities. Although the theory is developed assuming constant velocity, the method can be used for depth migrated images produced with smoothly varying velocity models, since the residually migrated images depend only on the ratio of the reference and updated velocities.

f-k Migration with Anti-Leakage Fourier Transform

This method was introduced by Sheng Xu et al. in [145] in 2004. Its aim is to estimate the spatial frequency content on an irregularly sampled grid. After obtaining the Fourier coefficients, the data can be reconstructed on any desired grid. For this type of transform, difficulties arise from the non-orthogonality of the global basis functions on an irregular grid. As a consequence, energy from one Fourier coefficient leaks onto other coefficients. This well-known phenomenon is called "spectral leakage". The key to resolve the spectral leakage is to reduce the leakages among Fourier coefficients in the original data before the calculation of

subsequent components. The robustness and effectiveness of this technique with both synthetic and real data examples are presented in [145].

Lagrange's Interpolation in f-k Migration

Aining Li in [88] demonstrates that Stolt interpolation can by done also with Lagrange's and sampling interpolation. The Stolt interpolation is carried out by changing of frequency variables. The selection and implementation of the interpolator is critical for the final image quality. If the interpolation algorithm is not chosen correctly , it can cause shading and multiple images in the focused data. On the other hand interpolation algorithms are implemented by means of numerical calculations so that they give rise to truncation or rounding errors, etc. Therefore, the interpolator must be carefully designed in order to obtain good final image quality. There are many polynomial interpolation algorithms which approximate the function utilizing 1st order, 2nd order, or nth order differences. The higher the polynomial is, the better the approximation is. Comparison of calculation the Stolt interpolation by Lagrange's and sampling interpolation is presented and discussed in [88].

2.5.8 The Inverse Problem

Inverse problem is a method that should estimate both, the location as well as the physical parameters of the targets like permittivity and conductivity. The main idea is to use some basic imaging method that estimate initial conditions and then solve inverse problem that leads to estimate location and physical parameters of the targets. There are many various mathematically more or less complicated models how to solve inverse problem and in the last time this topic becomes an individual science discipline. In conjunction with radar imaging some of the good works can be found in [42] - chapter 7.9, [79] - chapter 6, or [104, 12, 18, 20, 37]. In this work only a basic principle is introduced.

From the inverse problem point of view, migration can be taken as an approximate solution to the general elastic wavefield inversion problem [63]. Full elastic inversion uses the entire measured wavefield as an input into a mathematical process that seeks to estimate the elastic parameters of the device under test. This is called an inverse problem because it is opposite to the classical forward modeling problem (Section 2.5.5) of predicting the measured wavefield response of a known elastic device under test model. Generally, a forward problem can be reduced to find the solution to a partial differential equation, in this case the elastic wave equation, given specifications of coefficients of the equation as functions of a position and given appropriate boundary conditions. Though it is often a very difficult process, it is usually more easily accomplished than the corresponding inverse problem. The inverse problem usually involve estimating the coefficients of

a partial differential equation given its response to a known source. Often, these inverse problems are ill-posed which is a mathematical term for a problem whose inputs are insufficient to determine all of its expected outputs. In addition, to being ill-posed, inversion problems are generally nonlinear and practical schemes are typically linearized approximations. The need to find approximate solutions has lead to a large number of different migration algorithms that are generally distinguished by the kind of approximations made. A true inversion technique would derive the velocity model from the data as a part of the inversion. Migration requires the velocity model as an input to focus and adjust amplitudes. In order to be a useful process, it should be true that migration requires only an approximate, or background, velocity model and that more detailed velocity information can be extracted from a successful migration than was put into it [96].

The possibility of "looking" at the interior of an object is based on the fact that the incident wave penetrates inside the object itself, collects information about its interior and finally is scattered, delivering information to the receivers. Although the capability of penetrating objects is part of the features of microwaves, there exists, however, a class of almost impenetrable objects. These objects are made up of perfect conductors, whereas objects made up of strong conductors are almost impenetrable in the sense that the impinging wave penetrates inside the object only to a shallow depth [75]. For such a class of objects it is thus possible to reconstruct only the object shapes but not to "look" inside them. This is what happens at optical frequencies, when the impinging electromagnetic radiation does not significantly penetrate inside objects of which our eyes are capable of seeing only the shape but not the interior [42]. Nevertheless, the inverse problem methods refer only to penetrable objects.

A practical implementation of inverse problem can be found e.g. in [79]. In this case it is used for landmine detection. As the first step, the position and overall shapes of the objects are computed in a fast manner. For this purpose the MUSIC algorithm [127,32] is used. After this first step the method chosen to solve the linearized problem is the Algebraic Reconstruction Technique (ART) [84, 77] which is widely accepted fast linear solution method. ART is used to determine the parameters of the objects, e.g. the parameter values of trinitrotoluene in landmine. It can be seen that results obtained by inverse problem are better than by the conventional Kirchhoff migration.

The simulations that use inverse problem in through-wall imaging field are shown e.g. in [157, 132, 131]. This technique promises reducing effect of multiple reflections between investigated objects including wall, as well as precise position, shape, and material characterization estimation. However, one has to mention that inverse problem requires huge computational cost. The computation requirements significantly rise with complexity of the measured scenario. Even a simple (close to the ideal) scenario with few targets requires long time for computation with

current computing techniques. That makes impossible to use inverse problem in real-time for rescue and security applications.

2.5.9 Multiple Signal Classification

MUSIC is generally used in signal processing problems and was introduced by Therrien in 1992 [138]. It is the method for estimating individual frequencies of multiple harmonic signals. The use of MUSIC for radar imaging was proposed by Devaney in 2000 [48]. He applied the algorithm to the problem of estimating the locations of a number of point-like scatterers. Detailed description of MUSIC algorithm can be found e.g. in [48, 32, 82].

MUSIC for image processing has been developed for multistatic radar systems. It is the wave equation based method. The basic idea of MUSIC is the formulation of the so called multistatic response matrix which is then used to compute the time reversal matrix whose eigenvalues and eigenvectors are shown to correspond to different point-like targets. The multistatic response matrix is formulated using frequency domain data, which is obtained by applying the Fourier transform to the time domain data.

N antennas are centered at the space points R_n, $n = 1, 2, ..., N$. The positions of the antennas are not necessarily restricted to be in the same plane or regularly spaced. The n-th antenna radiate a scalar field $\psi_n(r, \omega)$ into a half space in which are embedded one or more scatterers (targets). M ($M \leq N$) is the number of scatterers and X_m is the location of the m-th target in the space. Born approximation is again considered [54, 26]. The waveform radiated by the n-th antenna, scattered by the targets and received by the j-th antenna is given by:

$$\psi_n(R_j, \omega) = \sum_{m=1}^{M} G(R_j, X_m)\, \tau_m(\omega) G(X_m, R_n)\, V_{Sn}(\omega) \tag{2.5.48}$$

where $G(R_j, X_m)$ and $G(X_m, R_n)$ are the Green's functions of the Helmholtz equation in the medium in which the targets are embedded in direction from transmitter antenna to the target and from the target to the receiving antenna respectively. $\tau_m(\omega)$ represents the strength of the m-th target and $V_{Sn}(\omega)$ is the voltage applied at the n-th antenna. In this formula, the signal is only considered for a single angular frequency ω. However, the extension for multiple frequencies is obvious. The multistatic response matrix K is defined by:

$$K_{nj} = \sum_{m=1}^{M} G(R_j, X_m)\, \tau_m(\omega) G(X_m, R_n). \tag{2.5.49}$$

The scattered waveform emitted at each antenna is measured by all the antennas,

so the elements of the multiple response matrix K can be calculated as:

$$K_{nj} = \frac{\psi_n(R_j, \omega)}{V_{Sn}(\omega)}. \tag{2.5.50}$$

The main idea of MUSIC is to decompose a selfadjoint matrix into two orthogonal subspaces which represent the signal space and the noise space. This method is often called Singular Value Decomposition (SVD) [27]. Since the multistatic response matrix is complex, symmetric but not Hermitian (i.e. it is not self-adjoint), the time reversal matrix T is defined from the multistatic response matrix:

$$T = K_{nj}^{*} K_{nj} \tag{2.5.51}$$

where * denotes the complex conjugation. The time reversal matrix has the same range as the multistatic response matrix. Moreover, it is selfadjoint. The time reversal matrix T can be represented as the direct sum of two orthogonal subspaces. The first one is spanned by the eigenvectors of T with respect to non-zero eigenvalues. If noise is present, this subspace is spanned by the eigenvectors with respect to eigenvalues greater than a certain value, which is specified by the noise level. This space is referred to as the signal space. Note that its dimension is equal to the number of the point-like targets. The other subspace, which is spanned by the eigenvectors with respect to zero eigenvalues (or the eigenvalues smaller than a certain value in the case of noisy data), is referred to as the noise subspace. The corresponding eigenvectors are denoted by the eigenvalues:

$$\lambda_1 \geq \lambda_2 \geq ... \geq \lambda_M \geq \lambda_{M+1} \geq ... \geq \lambda_N \geq 0 \tag{2.5.52}$$

of the time-reversal matrix T and v_n, $n = 1, 2, ..., N$ are the corresponding eigenvectors. The signal subspace is spanned by $v_1, ..., v_M$ and the noise subspace is spanned by the remaining eigenvectors. For detection of the target the vector g^p is calculated from the vector of the Green's functions:

$$g^p = (G(R_1, p), G(R_2, p), ..., G(R_N, p))'. \tag{2.5.53}$$

The point P is at the location of one of the point-like targets if and only if the vector g^p is perpendicular to all the eigenvectors v_n, $n = M+1, ...s, N$. In practice, the following pseudo spectrum is usually calculated by:

$$D(P) = \frac{1}{\sum_{n=M+1}^{N} |(v_n, g^p)|^2}. \tag{2.5.54}$$

The point P belongs to the locations of the targets if its pseudo spectrum is very large (theoretically, in the case of exact data, this value will be infinity).

Simulated time-reversal imaging with MUSIC considering multiple scattering between the targets is shown in [64]

In this case influence of a wall can be taken into account by applying Green's function considering the wall, what is a real challenge itself.

2.5.10 Singular Value Decomposition

As it is mentioned above, the singular value decomposition is used as part of the Music algorithm, in particular to make a distinction between which vectors span the signal subspace and which ones span the noise subspace. The next step of MUSIC is construction of Green's functions vector and project them to noise subspace in order to determine if the spatial point for which it was constructed contains a scatterer or not. However, the SVD do not has to be used with a time consuming solving of Green's function. It can be very effectively used to reduce clutters after the imaging was applied [27]. The challenging problem in through-wall imaging is a large reflection of energy from the wall that occurs due to high contrast between the dielectric constant of the wall and air, which leaves very small amount of energy to pass through the wall, reflect from the target and then pass through the wall back again to reach the receiving antenna. Thus, separating the weak target signal and strong reflection is very important. Clutter may result in a false alarm as it dominates the data and obscures the target information. For clutter reduction, it is important to separate the target signal and clutter in the received data. The SVD may be a useful tool to achieve this separation [27].

2.5.11 Boundary Scattering Transform

Shape Estimation Algorithm based on Boundary Scattering Transform (BST) [120] and Extraction of Directly scattered waves (SEABED) algorithm was introduced by Takuya Sakamoto et al. [121] in 2004. The algorithm uses very simple geometrical approach without velocity compensation based on Inverse Bistatic Boundary Scattering Transform (IBST) [120]. First, the image of the wave front $Iw(X, Y, Z)$ is derived from measured raw data (B-scan). It mostly means to find peaks in B-scan. The image of the front wave is binary, hence contains only two amplitudes: amplitude zero - when there is nothing or noise, and amplitude one - when there is the is front wave of the measured object. The transformation from $Iw(X, Y, Z)$ space (before imaging) to the real $Ir(x, y, z)$ space (after imaging) can be done by simple geometrical approach [121]:

$$\begin{aligned} x &= X - Z\frac{dZ}{dX} \\ y &= Y - Z\frac{dZ}{dY} \\ z &= Z\sqrt{1 - \left(\frac{dZ}{dX}\right)^2} \end{aligned} \tag{2.5.55}$$

SEABED was developed for monostatic approach. Shouhei Kidera et al. in [81] in 2006 introduced IBBST what is bistatic modification of SEABED. Transformation

from $Iw(X,Y,Z)$ space to the real $Ir(x,y,z)$ space can be done by:

$$\begin{aligned} x &= X - \frac{2Z^3 Z_x}{Z^2 - d^2 + \sqrt{\left(Z^2 - d^2\right)^2 + 4d^2 Z^2 Z_X^2}} \\ y &= Y + Z_Y \left\{ d^2 \left(x - X\right)^2 - Z^4 \right\} / Z^3 \\ z &= \sqrt{Z^2 - d^2 - \left(y - Y\right)^2 - \left(Z^2 - d^2\right)\left(x - X\right)^2 / Z^2} \end{aligned} \tag{2.5.56}$$

where d is distance between transmitter and receiver.

SEABED method was used for detecting the contours of object behind a wooden wall by Sebastian Hantscher et al. in [68] in 2006. The results from real measurement are compared with Kirchhoff migration and f-k migration on a very simple scenario. The cylinder was positioned behind the wooden wall with the smooth surface. The next practical 3 Dimensional (3D) measurement was done through the 5 cm concrete wall [69] in 2008. The SEABED reasonable saves a computational time. It is even ten times faster than f-k migration. A number of points with nonzero amplitudes in $Iw(X,Y,Z)$ space is very small, therefore only a few points have to be processed. However, for practical scenarios through thick brick, or concrete walls the derivation of the wave front from the measured data will be a critical step.

2.5.12 Fast Back Projection

Fast back projection algorithm was developed for tomography [21, 148] and later modified for airplane SAR imaging in [144]. The main advantage of this method is the smaller computational complexity in comparison with classical back-projection described in Section 2.5.2. Classical back projection requires $O(N^3)$ operations to generate N projections for $N \times N$ image whereas the fast back projection requires only $O\left(N^2 \log N\right)$ operations. The fast back projection algorithm is performed in two parts. First, the received data are recursively factorised into a number of decimated data-sets for subimages of the reconstructed image. An example of factorisation is shown on Fig. 2.5.7 (upper side), the resultant hierarchy of data-sets is shown on lower side.

Secondly, each data-set is back-projected to the corresponding subimage. A computational gain is achieved through decimating the data in the factorisation step. However, this step introduces an error that degrades the image quality [73]. There were made lot of modifications in the fast projection algorithm, like filtered back-projection [15], fast factorised back-projection [50], [140], quadtree back projection [97], omega-k quadtree back projection [36], etc. However, none of these methods has better accuracy than classical back projection, or faster computational times than f-k migration.

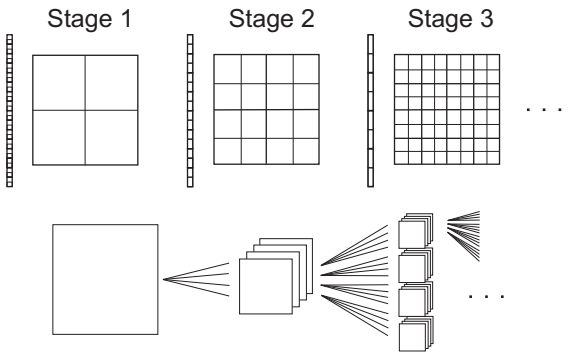

Fig. 2.5.7: An example of factorisation (upper side) and the resultant hierarchy of data-sets (lower side).

2.5.13 Migrations with Antenna Beam Compensation

Kun Liu et al. [90] in 2002 made a research how the consideration of antenna angle beam would change computations and results in wave equation based algorithms such as Kirchhoff migration and f-k migration. They called it the effects of dip-limited Kirchhoff migration and f-k migration. In praxis most measurements are done with wide beam antennas. However, not with omni-directional, but with some specific antenna flaring angel beam, that can be precisely measured. The waves that are aslant to the antennas have lower transmitted or received amplitudes. Taking into account this fact in computations some improvements can be done in the resulting image. It also decreases the computational cost in Kirchhoff migration or suppress noise in both Kirchhoff and f-k migration [90]. Dip-limited f-k migration is common f-k migration with an embedded dip filter. The dip-limited Kirchhoff migration is implemented by limiting the aperture of migration operators. The dip-limited Kirchhoff migration generates additional artifacts when the dip limit is less than the maximum dip on the desired output section. These artifacts are caused by the endpoints of the migration operators and become more obvious as the dip limit is decreased. A geometric explanation as well as a synthetic experiment are described in [90]. With the same idea, however, much more from mathematical point of view Murthy N. Guddati et al. [65] came in 2005.

2.5.14 Conclusion

The migrations are formally divided into two main groups. Backprojection involves migration based on simple geometrical approach, whereas Backpropagation represents migrations based on wave equations. Hence, the backpropagation migrations should provide better results from physical point of view.

SAR imaging, Kirchhoff migration, and Stolt migration are most often used migrations. SAR imaging and Kirchhoff migrations have almost the same compu-

tational complexity and they differ only in details. However, SAR imaging falls into the backprojection methods, whereas Kirchhoff migration into the backpropagation. Stolt migration is formally the Kirchhoff migration in frequency domain from mathematical point of view. Only the practical implementation introduces differences, that lead to the disparity in results. Because of implementation in frequency domain, the Stolt migration has much smaller computational complexity than Kirchhoff migration. SAR imaging and Kirchhoff migration are easily modifiable for precise compensations and improvements in comparison to Stolt migration. All three methods are not ideal and produce several artifacts.

BST as a part of the Backprojection is the method with a very small computational complexity. However, it requires wave front derivation from the measured data, what is a difficult and critical step, especially for complex scenarios.

Very promising group of methods are migrations based on using Green's function for solving the inverse problem, such as MUSIC that includes SVD. This technique promises reducing of an effect of multiple reflections between investigated objects including wall, as well as precise position, shape, and material characterization estimation. However, the inverse problem requires huge computation cost. The computation requirements significantly arise with complexity of the measured scenario. Even a simple (close to the ideal) scenario with few targets requires long time for computation with the current computing techniques. That makes impossible to use inverse problem real-time for rescue and security applications. This is the reason why we will not deal with this method in our research.

All the migrations give unprecise results without the compensation of a wall. The simple wall compensation technique presented in Section 2.5.3 do not provide sufficient result for complex scenarios. Therefore, a more precise compensation method is required, however, with small computational complexity that still can be used in practice.

Chapter 3

Goals of Dissertation

Investigation of the objects behind an opaque wall is a very promising field for a rescue and security applications nowadays. However, through-wall imaging is still a very young developing field based mostly on theoretical approaches. There are only few works published recently showing real measurements results. It is obvious, that the present methods are not ready for practical usage. Using conventional methods in praxis leads to unprecise and distorted results. Moreover, most of them uses extremely time consuming computations what obstructs to use them in real-time applications. The way to introduce through-wall radars in real and practical applications is very meander and still requires a lot of research in signal processing as well as in radar hardware field.

Based on the previous analysis, our research would be concentrated on signal processing and improvements of methods, that move through-wall radar field closer to the practical utilization. We will be focused on methods that can be used in realtime. The goals of the thesis can be summarized as follows:

- to develope an effective and precise method for estimation of TOA through the wall that is required for precise migrations, with small computational complexity that can be used for practical applications;
- to develope fast, precise, and easy to handle measurement method for estimation of wall parameters required for precise TOA through-wall estimation that can be used for practical applications;
- to develope an image processing method for highlighting the building contours in order to enhance the wall visibility of a building scanned from the outside;

Chapter 4

Selected Research Methods

Our research was concentrated onto three main tasks. First, in Section 4.1 a precise, efficient, and fast method of TOA estimation for through-wall scenario was investigated. Second, in Section 4.2 easy to handle, fast and practical method for measurements of wall parameters with UWB radar, that is required for precise TOA estimation was developed. Third, in Section 4.3 a method for highlighting of inner and outer building contours scanned from the outside by utilization of image processing algorithms is presented. In Section 4.4, the performance of basic migration methods was compared for through-wall scenario and several practical measurement scenarios measured with M-sequence UWB radar system are shown.

4.1 Through-Wall TOA Estimation

Precise TOA estimation is a basic step of standard migration methods for object imaging from SAR measurements. In this section, an effective computational method of the TOA for through-wall model is presented, published by the author in [1]. The conventional method that uses constant velocity model produces errors in object shape and position estimation [141, 4, 3]. Computation of the TOA (corresponding to the true flight distance) for three layer model requires the complex minimization algorithm. The proposed method transforms three layer (air-wall-air) model to an equivalent two layer (air-wall) model with lower computation complexity and the same precision. It uses iterative solution of well defined minimization problem. Moreover, conveniently selected initial conditions of iteration process can further decrease computational complexity of the method. The proposed method provides more precise TOA estimation than the conventional one and is less complex than three layer methods. Therefore, it is suitable for implementation on realtime hardware. The method performance is demonstrated by processing of real 2D SAR data acquired by through-wall M-sequence UWB radar system.

The conventional method for computing TOA with constant velocity model, which does not consider different velocity in the wall and air, introduces an error in estimation of target shape and position [141]. Therefore, more or less accurate methods based on a ray theory and Snell's law are used in algorithms of TOA computation to compensate the presence of the wall [61, 5, 86, 6]. The TOA for multilayer model cannot be computed directly, some numerical minimization method [106], has to be chosen. In general, the optimization techniques use TOA as an error function, and a vector of independent variables over which the error is minimized [76]. The number of variables is equal to the number of layers. This is a very time consuming process, but for small number of layers (especially for air-wall-air structure) a few improvements that significantly reduce the computation complexity will be presented.

4.1.1 Properties of the Waves Penetrating Through the Wall

Through-wall imaging requires waves to penetrate through the specific building materials such as concrete blocks, clay bricks, mortar, plaster, drywall, asphalt shingles, fiberglass insulation, etc. The transmitted signal is attenuated several times due to the free space loss, scattering from air-wall interface, loss in the wall, and the scattering from objects. The propagation loss inside the wall is a function of the frequency [147]. Electromagnetic waves are able to penetrate through the concrete walls without massive attenuation of up to approximately 3 - 4 GHz [101]. With regard to this fact, M-sequence UWB radar technology is very attractive for through-wall object imaging.

TOA is commonly referred to the flight time of the wave between transmit antenna, target, and receive antenna. To simplify the notation we denote TOA_{AT} as the flight time of wave between transmit antenna and target, or receive antenna and target. TOA_{AT} corresponds to the summation of distances between antenna and the target divided by appropriate velocities in air and the wall (4.1.1).

When the wave arrives to the wall under a certain angle, the wave in the wall will continue its propagation but with changed direction. This holds in the case when the permittivity of the wall differs from the permittivity of the layer in front of the wall. Even more, when the wave is leaving the wall, it changes its direction once more. In the case that the permittivity of the wall is greater than the permittivity of the air $\varepsilon_w > \varepsilon_a$, the wave velocity in the wall would be lower than in the air. When the relative permittivity of the air ε_{ra} is equal to 1, the wave velocity in the air is equal to the velocity of the light c. The velocity in the wall in this case is given by (2.5.5).

In the case when ε_{a1} of the air in front of the wall and ε_{a2} of the air behind the wall are the same, $\varepsilon_a = \varepsilon_{a1} = \varepsilon_{a2}$, the incidence angle of the incoming wave

is the same as the angle of the outgoing wave which is leaving the wall, so the wave behind the wall has the same direction as that in front of the wall. This condition is fulfilled only for a homogeneous wall or if the wall consists of the arbitrary numbers of homogeneous layers in parallel to the wall.

This section is focused on computation of the true TOA_{AT} between antenna and target, with the wall in between them. The losses in the wall are not considered here.

4.1.2 True TOA Between Antenna and Target

To estimate the correct position of the objects behind the wall, the exact TOA_{AT} between the antenna and the object has to be known. To compute this time, the model that is shown in Fig. 4.1.1 is used.

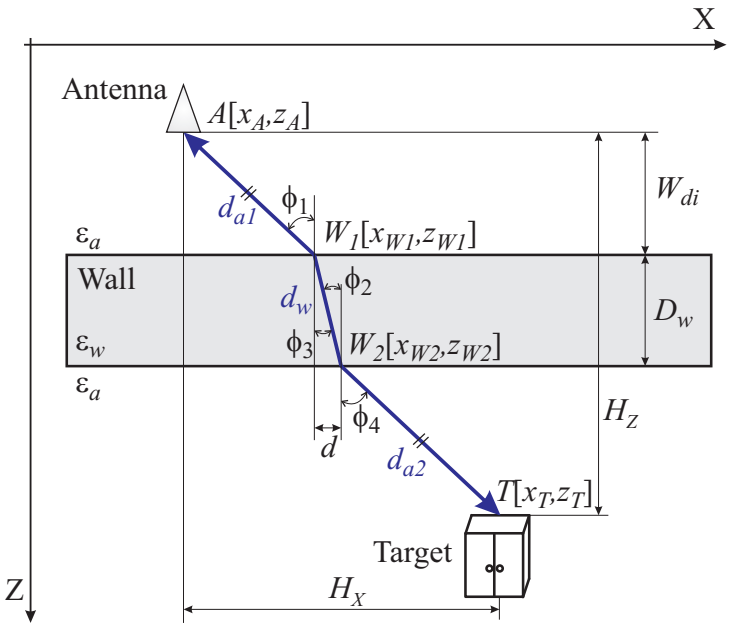

Fig. 4.1.1: True flight distance model in through-wall scenario.

There are several assumptions: the wall is homogeneous with constant permittivity and constant thickness; the relative permittivity of the air in front of the wall and behind it is the same and equals to one; the coordinations of the antenna $A[x_A, z_A]$ and the target $T[x_T, z_T]$, the permittivity of the wall ε_w, the thickness of the wall D_w, and distance of the wall from antenna in Z direction W_{di} have to be known. Because the material inside the wall is homogeneous, the angles $\phi_1 = \phi_4$ and $\phi_2 = \phi_3$.

The true flight distance between antenna and target is not equal to straight distance $|AT|$ between them. It has to be computed as summation of distances

$d_{tot} = d_{a1} + d_w + d_{a2}$. A minimization method has to be used, because the coordinates of W_1 and W_2 (Fig. 4.1.1) are unknown and cannot be computed directly. Optimization procedures are based on the minimization of the travel time principle. For example, the travel path must be certain that the travel time between two arbitrary points is minimal [76]. Ryohei Tanaka in [136] introduced a method how to compute true TOA for two layer model (air-ground) used for ground penetrating radar applications. Four roots are computed from derivation of the TOA equaled to zero. Then, the right one is chosen and the true TOA is computed. For three layer model (air-wall-air) Fauzia Ahmad in [6] introduced complex and time consuming method that solves several goniometrical functions for computing true TOA. In order to transform three layer model (air-wall-air) into the less complex two layer model that will not introduce any error in precise TOA_{AT} estimation we introduce one simple trick.

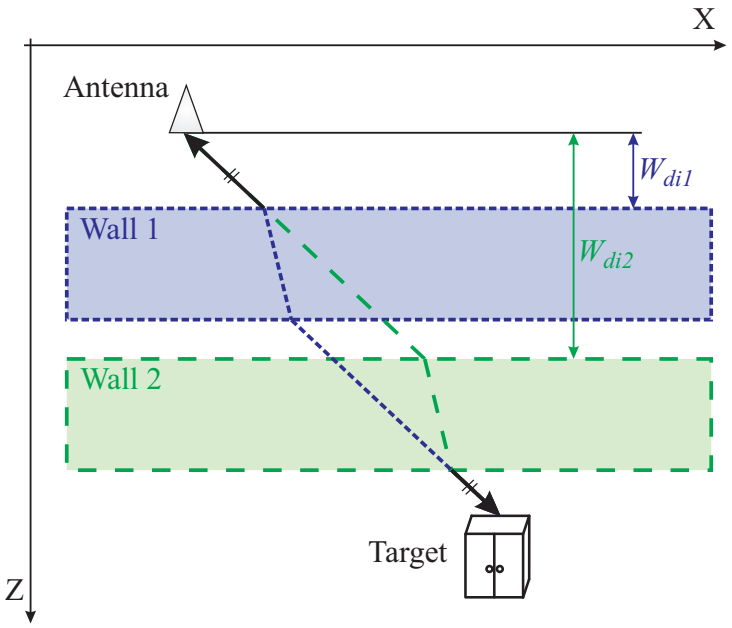

Fig. 4.1.2: Total flight distance does not depend on distance between antenna and wall W_{di}.

The distance between the antenna and the wall W_{di} in Z direction does not play any role in the TOA_{AT} estimation (Fig. 4.1.2). When the distance between antenna and wall changes from W_{di1} to W_{di2}, the true flight distance between antenna and target would not be changed. The only one condition has to be fulfilled, the entire wall has to be between the antenna and the target. Now, all the computations can be done with assumption that the rear side of the wall is at the target position and the two layer model (air - wall) can be used. With this simple trick the minimization process for three layer model does not need to be

computed, what leads to much faster computation. Even if the Tanaka has already solved this problem in [136], hereunder, we introduce several improvements and simplifications that speed up computations even more.

One have to mention, that antennas can be placed directly on a wall during measurements, and two layer model is directly obtained. However, in this case, the wall is in the antenna's near field and therefore antenna impulse response in time domain has been significantly changed. Hereby, the reducing of long antenna impulse response influence on measured data by deconvolution, as it is described in Section 2.4.4, is not applicable any more. Therefore, antennas are placed at least 0.5 m from a wall during SAR scanning in practice, $W_{di} \geq 0.5$ m.

The true TOA_{AT} can be computed like summation of both times, the time of flight in the air and the time of flight in the wall:

$$TOA_{AT}(d) = \frac{d_a}{c} + \frac{d_w}{v_w} \tag{4.1.1}$$

where $d_a = d_{a1} + d_{a2}$. The total flight distance d_{tot} is computed as:

$$d_{tot} = d_a + d_w \tag{4.1.2}$$

where

$$d_a = \sqrt{(H_Z - D_w)^2 + (H_X - d)^2}, \quad d_w = \sqrt{D_w^2 + d^2} \tag{4.1.3}$$

where H_X is the distance between the antenna and target in X direction, H_Z is the distance between the antenna and target in Z direction (Fig. 4.1.1). The true TOA_{AT} for any antenna position $A[x_A, z_A]$ and target position $T[x_T, z_T]$ that is represented by the image pixel position H_X and H_Z is required for formatting the image during SAR imaging. After substituting d_a and d_w from (4.1.3) to the (4.1.1), only d will be unknown. In order to estimate d, the minimization process is computed by derivation:

$$\frac{\boldsymbol{d}TOA_{AT}(d)}{\boldsymbol{d}d} = 0 \tag{4.1.4}$$

After several simple mathematical operations the fourth order polynomial equation with five coefficients is obtained:

$$co_1 d^4 + co_2 d^3 + co_3 d^2 + co_4 d + co_5 = 0 \tag{4.1.5}$$

where coefficients:

$$\begin{aligned} co_1 =& c^2 - v_w^2, & co_2 =& 2H_X\left(v_w^2 - c^2\right) \\ co_3 =& H_X^2\left(c^2 - v_w^2\right) + c^2\left(H_Z - D_w\right)^2 - v_w^2 D_w^2 & & \\ co_4 =& 2v_w^2 D_w^2 H_X, & co_5 =& -v_w^2 D_w^2 H_X^2 \end{aligned} \tag{4.1.6}$$

The analytical solution of (4.1.5) even with Ferraris or Galois method [139] requires huge number of divisions and square root operations. Therefore, unlike in [136],

we have chosen the Newton-Horner iteration method [24,107] for root computation because of its lower computational cost. Two of the roots are complex conjugate, the third is real but negative and the fourth - the right one, is real and positive. Unlike in [136], all four roots do not have to be computed. Because the required root can be estimated from an initial value quite well, only this one root is computed. This root represents the examined value of d, therefore it is restricted at least to the interval $d \in < 0, H_X >$. Practically, the limitation of d could be much more narrower. There are many possibilities how to estimate the initial values of d_{init} very close to the right one, so only a few iterations have to be done to obtain the correct d with sufficient precision.

The Newton-Horner iteration algorithm can be described as follows:

$$d_{n+1} = \left| d_n - \frac{\sum_{i=1}^{5} co_i d_n^{5-i}}{\sum_{j=1}^{4} \left(\sum_{k=1}^{j} co_k d_n^{j-k} \right) d_n^{4-j}} \right|, \quad \begin{matrix} n = 1, 2, ..., I \\ d_1 = d_{init} \end{matrix} \tag{4.1.7}$$

where I is the number of iterations. After 10 iterations the result has higher accuracy than is required in praxis for standard applications, even after 5 iterations the results are sufficient. The iteration algorithm requires only a few Multiply And Accumulate (MAC) operations and one division per iteration. The proposed algorithm for true TOA_{AT} computation does not require sine or cosine computation and the whole algorithm can be implemented in realtime hardware with relatively small computational requirements. The conventional method with no wall compensation computes the TOA_{ATconv} as straight line between antenna and target:

$$TOA_{ATconv} = \sqrt{(x_T - x_A)^2 + (z_T - z_A)^2}/c \tag{4.1.8}$$

It requires 5 MAC and 1 square root operation. In the proposed algorithm the co_i, d and TOA_{AT} are computed from (4.1.6), (4.1.7) and (4.1.1), respectively. It requires 109 MAC operations, 2 square roots, and 10 divisions for 10 iterations.

Computation of the TOA_{AT} by the proposed method is much more time consuming process than by the conventional method, but it is still very fast process comparing to the three layer model [6] with different permittivity in each layer. TOA_{AT} can be expressed by the one unknown variable also for three layer model, but it is very complex relation and after derivation polynomial of a very high order is obtained. Therefore, this simple numerical method for root computation is very time consuming and the critical points have to be investigated with the second order derivation.

In order to form image during migration, unlike in the simple wall compensation

algorithm (2.5.9), the summation is describer as:

$$I(x_T, z_T) = \frac{1}{N} \sum_{n=1}^{N} B_{Pn} \left(X, k = (TOA_{TX-T} + TOA_{T-RX}) \right) \tag{4.1.9}$$

where TOA_{TX-T} is a time of flight between transmit antenna and target and TOA_{T-RX} is a time of flight between target and receive antenna.

The TOA_{AT} of targets behind and inside the wall can be computed with the proposed algorithm. For targets in front of the wall, the conventional geometrical approach can be used (4.1.8). For targets inside the wall, only the thickness of the wall has to be changed and the same algorithm as for the targets behind the wall can be used. Therefore it is possible to use this approach for correct imaging of the targets behind the wall as well as in the wall itself.

This algorithm can be used for computation of TOA_{AT} between transmitter and target as well as between target and receiver for both monostatic and bistatic cases. It is interesting that the true flight distance between the antenna and the target from d and (4.1.2) can be computed, although the coordinates of inflection points W_1 and W_2 stay unknown.

The proposed method can be used for static objects and moving antennas - SAR imaging, as well as for static radar when the targets are moving - detection of moving people behind the wall [114, 115] and detection of trapped people [152].

4.1.3 Estimation of Initial Conditions

There is one initial parameter used as an input to the iteration algorithm described above. It is the distance d (see Fig. 4.1.1). d is restricted at least to the interval $d \in < 0, H_X >$. The more precisely d_{init} is estimated the less number of iteration are required to obtain d with sufficient precision. Very simple prediction can be done by:

$$d_{init} \approx \frac{H_X}{2}. \tag{4.1.10}$$

Because the three layer model was transformed into the two layer model (Fig. 4.1.3) without any error introduction, the estimation from well-known GPR field can be used. We suggest to used more precise estimation method than expressed by (4.1.10) but still with small computational complexity described in [76]. Here, the d_{init} can be estimated as:

$$d_{init} \approx \sqrt{\frac{\varepsilon_a}{\varepsilon_w}} \left| ET_1 \right|. \tag{4.1.11}$$

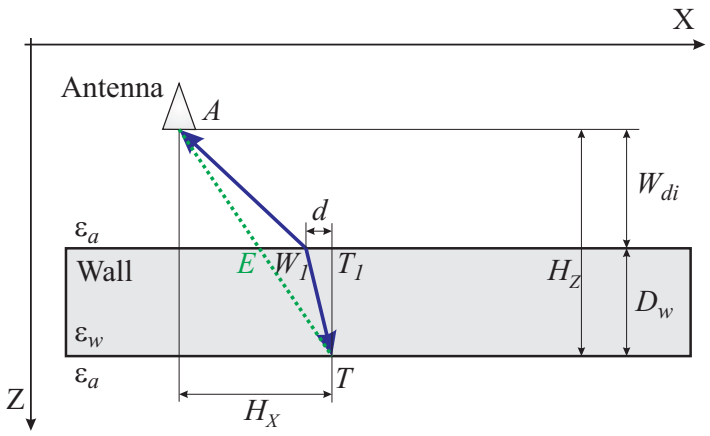

Fig. 4.1.3: Two layer through-wall model.

By a simple geometrical manipulations as we described in [137] the d_{init} can by estimated as:

$$d_{init} \approx \sqrt{\frac{\varepsilon_a}{\varepsilon_w}} \frac{H_X D_W}{H_Z}. \tag{4.1.12}$$

In [137] we used (4.1.12) as a final estimation of d for TOA computation, here it is used only to estimate the initial condition - d_{init}.

4.1.4 Simulation Results

Several simulation experiments are shown in order to demonstrate efficiency and precision of the proposed algorithm. The simulated scenario of an object behind the wall is shown in Fig. 4.1.4. Firstly, the investigated parameter d is computed with initial condition given by (4.1.10). The results dependant the on number of iterations are compared with the true value of d and shown in Table 4.1. In next,

Table 4.1: Dependence of d on number of iterations. $d_{init} \approx \frac{H_X}{2}$.

Iterations	0	1	2	3	4	5	6	7
$d[cm]$	150	63.636	26.6	18.797	17.7	17.673	17.673	17.673
$Err_d[\%]$	748.752	260.075	50.512	6.360	0.153	0.000	0.000	0.000

d is computed with initial condition given by (4.1.12). The results are shown in Table 4.2. $Err_d[\%]$ represents a relative error of d in percentage. It is obvious, that only a few iterations lead to precise results. Only 5 iterations are required to obtain $Err_d < 0.0005\%$ in case the d_{init} is computed according to the (4.1.10). In case the d_{init} is computed by (4.1.12), only four iterations are required.

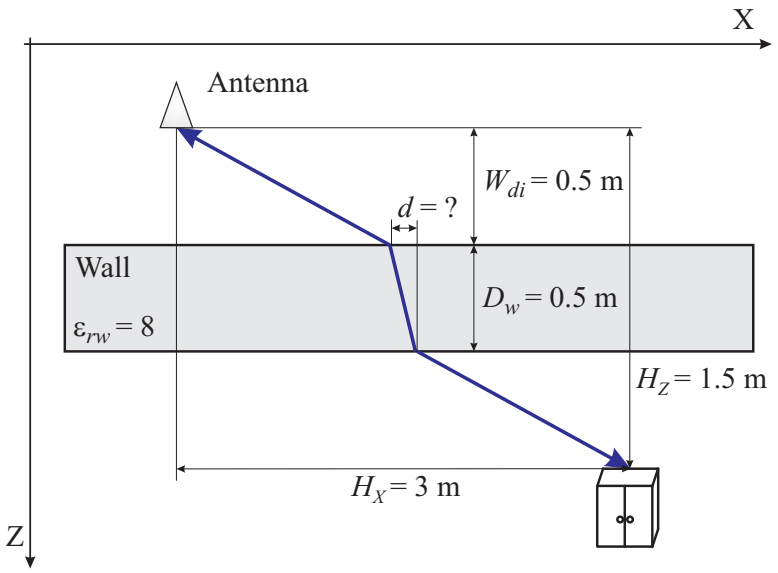

Fig. 4.1.4: Simulated scenario of object behind the wall.

Table 4.2: Dependence of d on number of iterations. $d_{init} \approx \sqrt{\frac{\varepsilon_a}{\varepsilon_w}} \frac{H_X D_W}{H_Z}$

Iterations	0	1	2	3	4	5	6	7
$d[cm]$	35.355	20.828	17.857	17.674	17.673	17.673	17.673	17.673
$Err_d[\%]$	100.051	17.852	1.041	0.006	0.000	0.000	0.000	0.000

The computation complexity of TOA estimation is a very important aspect, e.g. in order to compute migration from SAR scanning consisting from $N = 300$ scans and with final image resolution $N_x = 500 \times N_z = 500$ pixels, the parameter d has to be computed $N_c = 150$ millions times.

$$N_c = N_x N_z N. \tag{4.1.13}$$

The computation method of d_{init} should be therefore chosen with sophisticated trade-off between precision and complexity, and with regard to the hardware performance.

In Table 4.3 precisions of several TOA methods are compared. Firstly, the TOA is computed as a straight line between the antenna and the target according to the (2.5.1) (one way antenna - target only) with no wall compensation. Secondly, a simple wall compensation method (Section 2.5.3) is used to compute TOA. Finally, the TOA is computed according to the proposed precise method. $Err_{TOA}[\%]$ represents a relative error of TOA estimation in percentage.

The shown precision is obtained only in case of homogeneous walls. In addition, the velocity of the wave propagation depends also on conductivity, permeability,

Table 4.3: Error in TOA estimation for through-wall scenario.

Method	Straight line between antenna and target	Simple wall compensation	Proposed method
$TOA[ns]$	11.188	14.238	14.994
$Err_{TOA}[\%]$	25.383	5.042	0.000

and frequency, as it is shown in equation (4.2.2). However, these parameters cause neglectable modification of the propagation velocity in praxis.

4.1.5 Irregular Movement Compensation

The antenna system, or the whole radar system has to move in scanning direction during SAR scanning. A very precise and linear scanning system can be used in a laboratory environment. However, it is impractical in real measurement scenarios.

In scanning direction (X - axis):

For rescue or security applications a moving trolley or vehicle is used. In this case it is almost impossible to move it with a constant velocity. Most of the migrations require input dataset (B-scan) with linear distances between two subsequent scans. Otherwise the output image will be deformed.

We used hand moving trolley with positioner system for measurements pictured in Fig. 4.1.5. The information about actual position in scanning direction is continuously saved with every received impulse response from the radar device. In order to align all scans to the regular grid, where every two subsequent scans have the same distances, a vector of antenna positions $\mathbf{s}$ in scanning direction shown in Fig. 4.1.6 b) is created. The antenna positions in vector $\mathbf{s}$ are linearly dependent on the number of scans. The calibrated and preprocessed B-scan $B_{Pn}(X,k)$ is interpolated through Spline interpolation S_{pline} as:

$$B_{PC}(X,k) = S_{pline}(B_P(X,k), \mathbf{s}) \tag{4.1.14}$$

where $B_{PC}(X,k)$ is a B-scan with compensated irregular trolley movement in the scanning direction. For the next processing, the $B_{PC}(X,k)$ in combination with antennas positions $\mathbf{s}$ is used.

In looking direction (Z - axis):

The irregular movement of scanning trolley leads to a varying distance between antenna system and scanning objects. In order to compensate this behavior during migration, the precise distance between antenna and the wall W_{di} has to be known.

Fig. 4.1.5: Trolley antenna movement - positioner system.

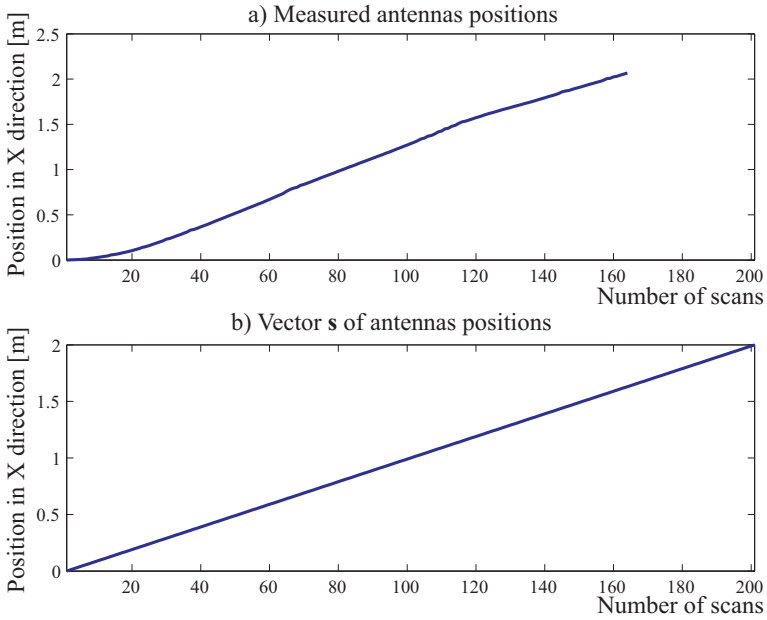

Fig. 4.1.6: Antenna system positions in X direction. a) Measured. b) Vector **s**.

The front wall that is directly in front of the antennas is clearly visible in the measured data set. It mostly represents the most significant part of the energy in B-scan after crosstalk removal. The positions of peak in dataset caused by the wall reflections could be effectively used to estimate the distances between the antennas and the wall W_{di}. The B-scan of through-wall scanning with zoom of the front

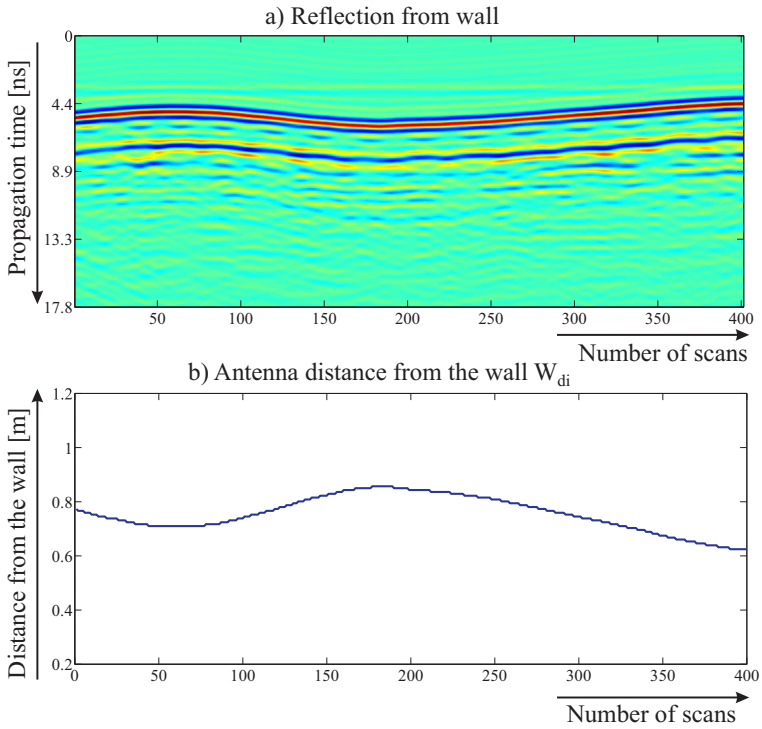

Fig. 4.1.7: Estimation of antenna distance from the wall. a) Reflection from the Wall, B-scan. b) Antenna distance from the wall W_{di}.

wall is shown in Fig. 4.1.7 a). The estimation of W_{di} is shown in Fig. 4.1.7 b). Estimated antenna distance from the wall can be used during TOA computation required for imaging.

4.1.6 Antenna Beam Compensation

Before the migration can be done, the antenna beam should be compensated according to the Section 2.5.13. Measurements of antenna direction proprieties leads to antenna footprint as a weight function depending on the antenna look angle:

$$w = footprint(\phi) \tag{4.1.15}$$

An example of horn antenna footprint is shown in Fig 4.1.8 a). Because the positions of the transmit and receive antennas are not the same in bistatic case (Fig 4.1.8 b)), two different weights for both antennas must be included in the formation of the SAR imaging algorithm:

$$I(x_T, z_T) = \frac{1}{N} \sum_{n=1}^{N} w_1 w_2 B_{PCn}\left(X, k = TOA_n\right) \tag{4.1.16}$$

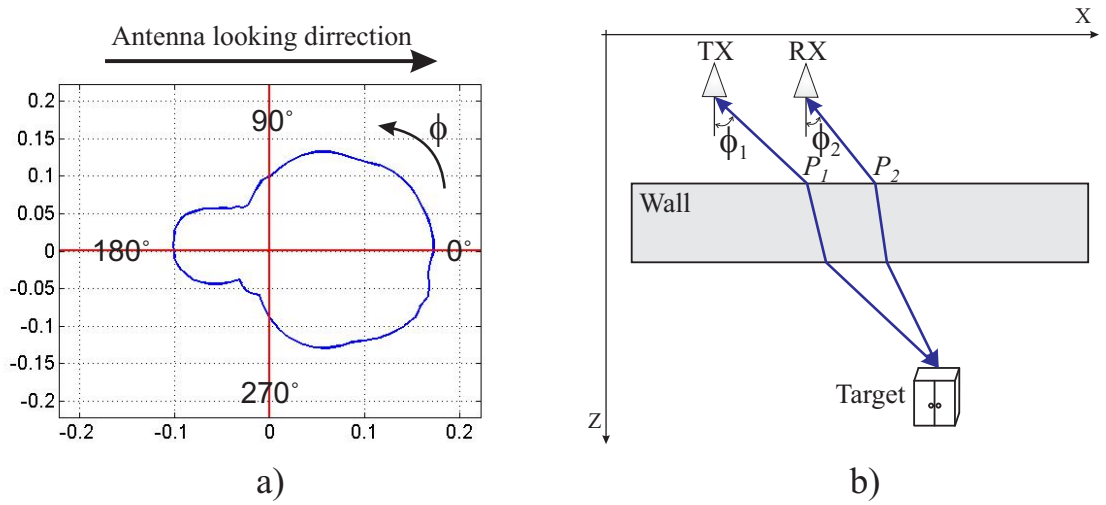

Fig. 4.1.8: a) The example of horn antenna footprint. b) Bistatic through-wall model.

where $w_1 = footprint(\phi_1)$ and $w_2 = footprint(\phi_2)$. The whole implementation of the antenna footprint to the SAR imaging increase the computation complexity only negligibly.

4.1.7 Measurements Results

The influence of the wall on imaging results is illustrated on two experiments. For testing of the proposed algorithm the 2D SAR measurements were chosen. The measurements were done with the 9 GHz M-sequence UWB radar system [43, 116, 118] described in Section 2.1.3. Bistatic model with the double-ridged horn antennas was used. For bistatic system the d_{tot} has to be computed twice, for transmitter-target flight distance and for target-receiver flight distance:

$$d_{tot\_bist} = d_{tot\_TX2T} + d_{tot\_T2RX}. \tag{4.1.17}$$

All the preprocessing and calibration steps described in Section 2.4 were undertaken. The irregular trolley movement was compensated, as well as antenna beam. The migration with a simple geometrical approach described in Section 2.5.2 called SAR imaging was used to transform time domain into the spatial domain. The wall was compensated by the proposed algorithm.

Scenario 1 is a simple scenario, where the measured object is in parallel with the scanned wall. The measured room was approximately 4 m × 5 m large, with the wall thickness of about 0.2 m. The wall was made of bricks with relative permittivity approximately $\varepsilon_{rw} = 4$. Distance between the centers of antennas

a) b)

Fig. 4.1.9: SAR measurement. a) Radar system in front of the wall. b) Measured object behind the wall.

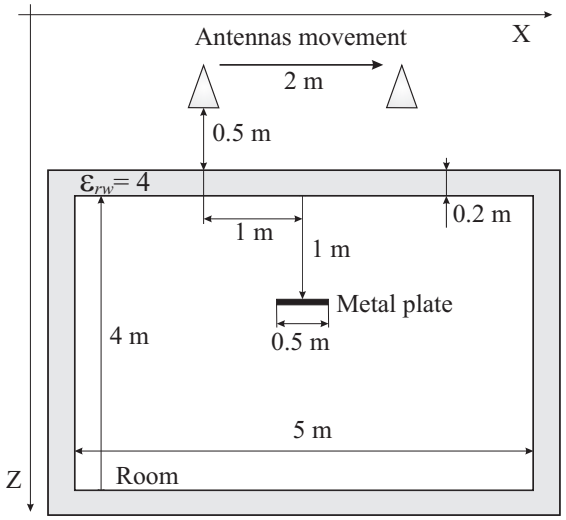

Fig. 4.1.10: SAR measurement - Scenario 1.

was 0.45 m vertically. The antenna system was moved in parallel to the wall along 2 m at distance 0.5 m from the wall. The object was placed 1 m behind the wall inside the room (Fig. 4.1.10). A metal plate of size 1 m × 0.5 m and thickness of a few millimeters was chosen as an object behind the wall.

In Fig. 4.1.11 a) and Fig. 4.1.11 b), the migrated images with conventional method where TOA si computed by (4.1.8) and the proposed method of *TOA* computation by (4.1.1) are shown, respectively. The targets have marked distances from antennas at antennas position 1 m in the scanning direction. The position of the metal plate in Z direction in Fig. 4.1.11 a) is about 1.9 m, what is approximately 0.2 m deviation from the real position. In Fig. 4.1.11 b) it is about 1.7 m what is very close to the real position. The front wall is in both images in the correct position, it starts approximately at 0.5 m in Z direction. The rear

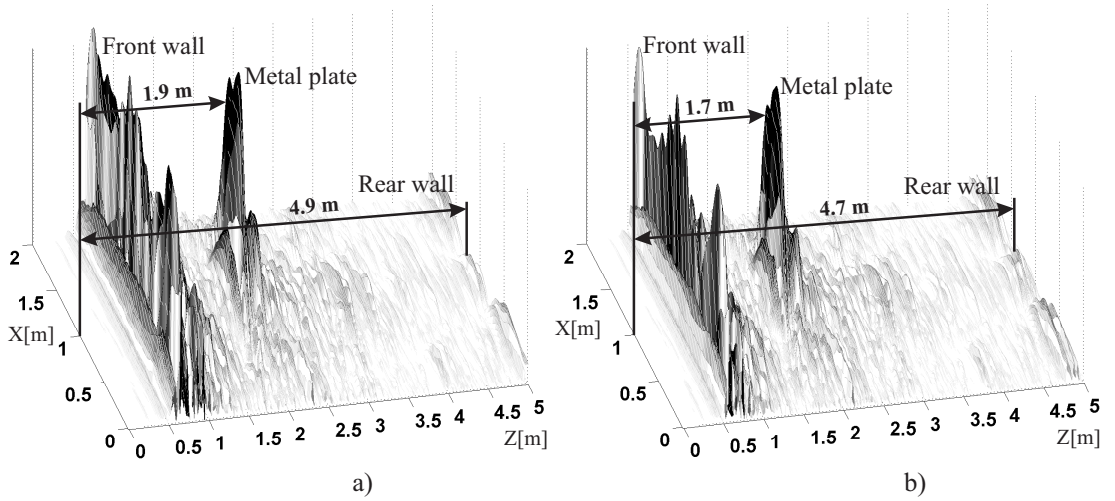

Fig. 4.1.11: Migrated images - Scenario 1. a) Conventional method without wall compensation. b) Proposed method with precise TOA estimation.

wall is in the correct position only in Fig. 4.1.11 b), approximately at 4.7 m in Z direction, in Fig. 4.1.11 a) it starts at 4.9 m.

Scenario 2 demonstrates how important true TOA estimation is in case the objects are not in parallel with the scanning direction. The wall compensation can be done also in much simpler way. An additional delay for a wave penetrating perpendicularly to the wall can be computed by (2.5.8) as we described in Section 2.5.3 and used for wall compensation [86]. This approach could be used only in case the waves are penetrating perpendicularly to the wall, what is not fulfilled in praxis. Compensation by this simple approach still provides much better results than without compensating the wall at all. However, it is not as precise as the compensation by the proposed method, as is shown in this second scenario (Fig. 4.1.12). The metal plate of size 0.67 m $\times$ 0.75 m was placed aslant behind the 0.4 m thick brick wall with relative permittivity approximately $\varepsilon_{rw} = 3.4$. As it can be seen in Fig. 4.1.13, even if the waves penetrate aslant in the wall, the proposed method provides correct coordinations of the left-bottom metal plate corner [X = 1.6 m, Z = 1 m], unlike the simple method for compensation [X = 1.73 m, Z = 1 m].

A noncompensation of the wall will cause that the objects will not be imaged in correct position. The image will be unfocused as well [141], however, in real measurements only the shifting of the objects to the incorrect positions is evident.

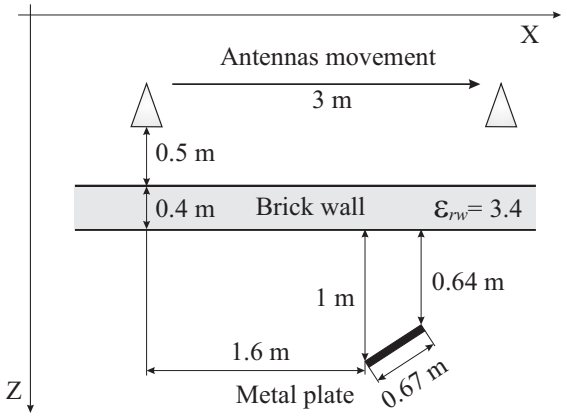

Fig. 4.1.12: SAR measurement - Scenario 2.

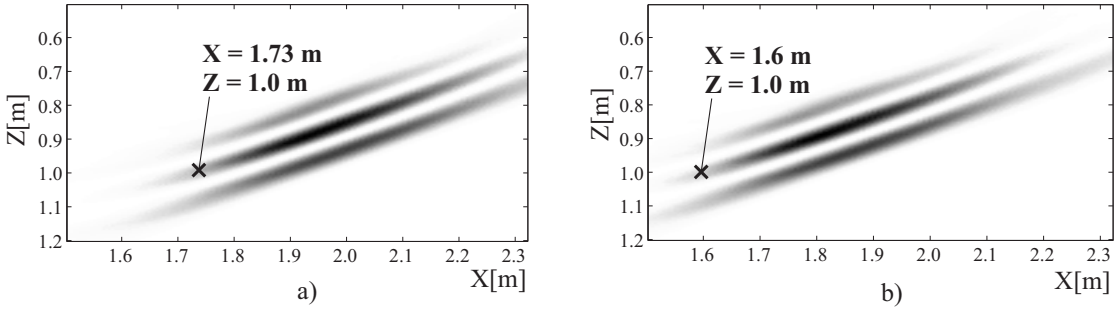

Fig. 4.1.13: Migrated images - Scenario 2. a) Method with simple wall compensation. b) Proposed method with precise TOA estimation.

4.2 Measurements of the Wall Parameters by Reflectometry

Precise SAR imaging of objects, detection of the moving person behind the wall, or non-destructive testing of the state or quality of walls constructions in civil engineering with UWB radar requires the knowledge of wall parameters like thickness, permittivity, and conductivity. Their use in data processing produces more precise and realistic results, as we have shown in Section 4.1. The more precise the wall parameters are known the better the complex algorithms for SAR imaging [1] or detection of moving persons [114] could be enhanced. The measurement of the wall parameters is challenge in a real environment especially when there is access only from one side of the wall. In this section, an effective and fast algorithm for wall parameters estimation that can be used in practice is presented. For that purpose the magnitudes and the time positions of reflections from inner and outer interfaces of the wall are extracted from the data. A new scanning method that

we propose significantly reduces the clutter caused by objects in the measurement environment such as reflections from other walls, the ceiling, the floor and antenna crosstalk. The algorithm was tested on 13 different types of walls with various permittivity, conductivity and thickness. A handheld M-sequence UWB radar with horn and circular antennas was used for data gathering. The proposed method is very robust and the error of the thickness estimation was less than 10% for most of the measured walls. The whole measurement could be handled by one person. The wall parameter estimation runs in real time and is fully automated.

4.2.1 Conventional Methods for Wall Parameters Estimation

There are several methods for estimation the wall parameters. They could be estimated most precisely when the wall is placed in between the antennas [102, 103,40]. However, this is not practical especially in case of terrorists or fire since it is meaningless for the intended applications to measure the wall from both sides. A further approach uses different standoff distances for wall parameters estimation in [141, 142]. A small object, that has to be visible from at least two antenna positions, has to be situated behind the wall what is impractical as well. Moreover, the wall parameters would be estimated incorrectly if the position of this object is estimated even with very little inaccuracy. Methods [141,142] were tested only on simulated data. SAR image de-smearing or auto-focusing were also used [8, 95]. However, the blurring of SAR images is practically very small and mostly lost in noise. Most of all the position of an object is changing significantly when the wall parameters are unknown as it has been shown in Section 4.1.7. This method was also tested only on simulated data. By representing the wall reflections in the Laplace domain, the pole positions can be used for wall parameter estimation using Prony's method [72]. However, even small noise would shift the pole positions significantly. Therefore, the approach is only useful for simulations. A model based solution of an inverse problem was also proposed. It solves iteratively the wave equations using Green's function [89, 14]. These methods are very complicated, require huge computation power as well as the time and most of them were tested only on simulated data.

In this section a new method for estimation of thickness, permittivity, and conductivity of a wall is introduced. The main attention was paid to develop a practical estimation method that could be used in the real environment. The measurement is carried out from one side of the wall, thus there is no need to enter a danger area. The measurement process is very fast and easy to handle. A positioning system is not required. The processing of the proposed algorithm does not take more than 2 seconds on a standard laptop with 1.8 GHz Intel processor in MATLAB.

4.2.2 Model of the Wave Propagation in the Wall

The main idea of the wall parameter estimation is to use time domain reflectometry. The Fresnel equations at the wall interfaces and plane wave propagation within the wall are applied. This idea was firstly introduced in [155]. However, here a time consuming iterative error minimization process that solves inverse problem for multilayer medium has to be processed. In addition, as a multiple reflection reduction technique a low effective time gating was chosen. Therefore, a wall with thickness only 12 cm was measured to prove the method's functioning. A time domain reflectometry was chosen for wall parameter estimation also in [119]. However, the piece of wall has to be placed in anechoic chamber room and measured with and without a metal plate behind it, what can not be done in a dangerous environment. The reflectometry principle was also used in [80]. However, only the theoretical approach was tested there on simulated data and an extensive iteration algorithm was used to estimate the wanted parameters. Furthermore, the whole wave propagation was assumed to be planar. This is not practical since it requires a large distance between the wall and the radar device.

Our approach permits spherical wave propagation. But within the wall we also simplify to planar waves in order to keep simple. An error made by that approximation is negligible since it only neglects the spreading losses in the wall. That is, the conductivity would be slightly overestimated. For our wall model, we suppose, as in [155] and [80], a flat wall surface, a homogeneous wall structure, and normal incidence of the sounding waves. Frequency independent wall permittivity ε_w and wall conductivity σ_w are also supposed. Moreover, it can be assumed that the relative permeability of common wall material will be $\mu_{rw} = 1$ and the wave attenuation would not be extremely strong at the applied radar frequencies.

Fig. 4.2.1 illustrates the wave propagation within a wall. Obviously, we have to deal with the reflections in both wall surfaces and the wave propagation within the wall. As demonstrated below, the reflections depicted in blue would be used to determine the wall parameters and the transmitted wave (green line) should sound the targets behind the wall. Reflections of higher order are not of interest (depicted as green dotted lines). Their amplitudes are negligible.

Fresnel's equations give ratios between the incident wave and the scattered respectively transmitted electrical field at a flat boundary for normal incident waves:

$$\Gamma = \pm\frac{\sqrt{\varepsilon_a} - \sqrt{\varepsilon_w}}{\sqrt{\varepsilon_a} + \sqrt{\varepsilon_w}}, \quad T = \frac{2\sqrt[4]{\varepsilon_a \varepsilon_w}}{\sqrt{\varepsilon_a} + \sqrt{\varepsilon_w}} = \sqrt{1 - \Gamma^2} \tag{4.2.1}$$

where Γ is a reflection coefficient, T is a transmission coefficient, and ε_a is the permittivity of the air or vacuum. The positive sign in Γ holds for the propagation air to a wall and the negative sign has be to applied if the wave moves from a wall to the air.

The wave propagation within the wall is characterized by the propagation

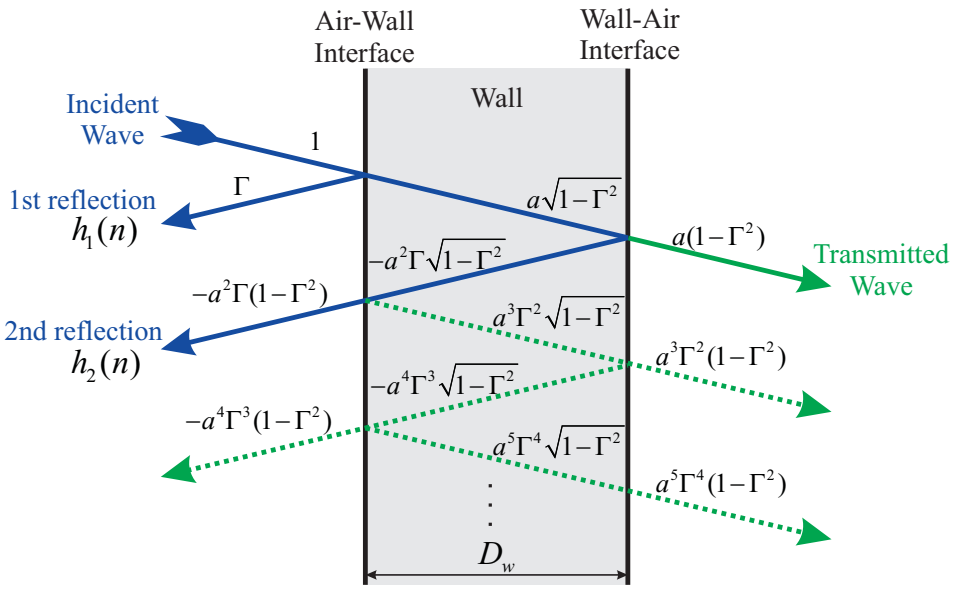

Fig. 4.2.1: Through-wall magnitude model - Reflectogram. Note: The aslant incidence of the wave is only plotted for better illustration of multiple reflections.

speed v_w and the propagation loss a_w. Both result from the solution of the plane wave equation of the electromagnetic field, which is usually determined for the frequency domain [134]:

Propagation factor:

$$\beta = \frac{2\pi f}{v_w} = \pm 2\pi f \sqrt{\frac{\varepsilon_w \mu_w}{2}\left(\sqrt{1+\left(\frac{\sigma_w}{2\pi f \varepsilon_w}\right)^2}+1\right)} \approx$$
$$\approx 2\pi f \sqrt{\varepsilon_w \mu_w} = \frac{2\pi f \sqrt{\varepsilon_{rw}}}{c} \tag{4.2.2}$$

Attenuation constant:

$$\alpha = \pm 2\pi f \sqrt{\frac{\varepsilon_w \mu_w}{2}\left(\sqrt{1+\left(\frac{\sigma_w}{2\pi f \varepsilon_w}\right)^2}-1\right)} \approx$$
$$\approx \frac{\sigma_w}{2 v_w \varepsilon_w} = \frac{\sigma_w}{2c\sqrt{\varepsilon_{rw}}} \tag{4.2.3}$$

where μ_w is the permeability of the wall, ε_{rw} is the relative permittivity of the wall, f is the frequency of the wave and c is the wave velocity in vacuum. Propagation

losses inside the wall can be computed as:

$$a_w = a_0 e^{-2D_w \alpha} \tag{4.2.4}$$

where a_0 is the magnitude of the incident wave and D_w is a wall thickness. Spread losses inside the wall are neglected.

Equations (4.2.2) and (4.2.3) also indicate approximations which follow from the fact that the conductivity of the most common wall materials is sufficiently small. Otherwise, the wave could not penetrate through the wall and the entire approach of object detection behind the wall would fail. In this case wall parameters estimation is useless.

From this set of simple equations, it is possible to estimate the wanted wall parameters. The first reflection would provide us the permittivity of the wall. From that the propagation speed can be calculated. Hence, the time delay of the inner wall reflection will give us the wall thickness. Thus, there is no iteration required as in [155] or [80] and the data may be taken directly from radar measurements which are usually given in the time domain.

4.2.3 Reducing of Clutters with New Scanning Method

The precise allocation of the second reflection from the wall-air interface is a critical step in wall parameters estimation by time domain reflectometry. However, it is a big challenge in practice because of antenna ringing, multiple reflections inside the antenna and inside the wall, multiple reflections between the antenna and wall, diffraction effects at the edge of the wall, signal scattered from objects other than the wall, lots of other clutter and random noise. Additionally, antenna crosstalk

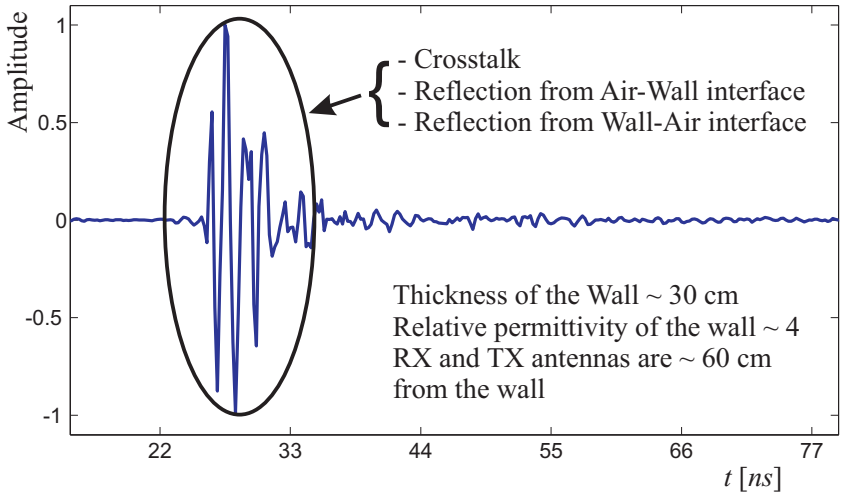

Fig. 4.2.2: Example of the reflections from the wall measurement.

and wall reflections are overlapped at close proximity to the wall (Fig. 4.2.2). In order to separate the wall reflections from unwanted components, we introduced a new method of scanning. The main idea behind this method is to move the antennas towards the wall (Fig. 4.2.3) and to average the data appropriately. During scanning, the positions of all clutter signals in the measured data are

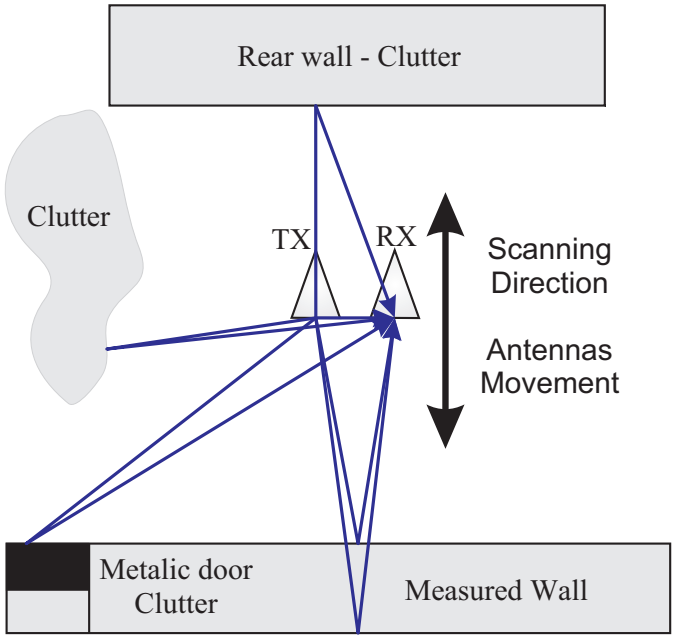

Fig. 4.2.3: Antennas movement with the new scanning method.

shifting with another velocity (sometimes even directions) as the position of the wall of interest. Fig. 4.2.4 depicts an example in which the radar was taken away from the wall, which can be seen by the growing propagation time. Other reflectors (ceiling, floor, back wall, etc) change their distance to the radar differently and hence they can be suppressed by averaging the signals along the "wall track". But note, the spreading losses due to spherical wave propagation have to be removed before averaging. The simplest way to reduce the clutter is to synchronize all impulse responses on the front wall reflection (it is always clearly visible), normalize each signal to its main peak and average all of them (Fig. 4.2.4). The antenna crosstalk should be removed beforehand and the data should be densely sampled in order to gain a precise synchronization between all measurements. Averaging the data from Fig. 4.2.4 b) in the horizontal direction leads to a cleaned impulse response $h(n)$ of the wall (see Fig. 4.2.5 a)) which we will separate in two parts - one originating from the reflection of the outer surface $h_1(n)$ and one caused by the inner surface $h_2(n)$. The two reflections are clearly visible. A third reflection is also indicated by the data. It is produced by a target which is out of interest here.

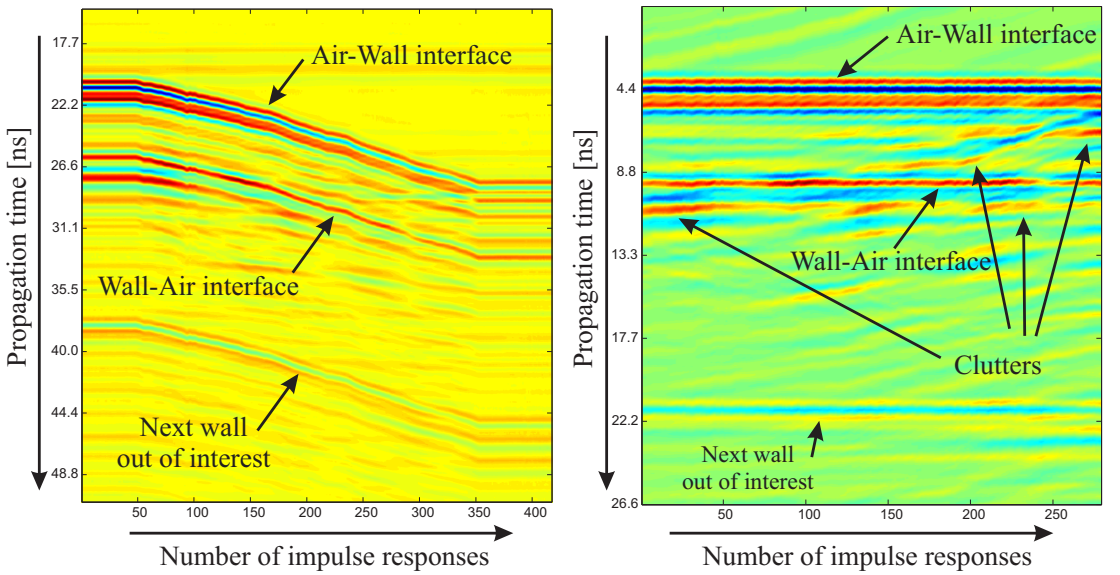

Fig. 4.2.4: B-scans, antennas were moved from 0.5 m to 1.5 m from the wall. a) Measured data, oversampled and without crosstalk. b) After synchronization and normalization, next wall is 1.8 m from measured wall.

4.2.4 Algorithm Description

As mentioned above, the first step is to determine the reflection coefficient Γ of the outer surface in order to be able to determine the wall permittivity. Since the incident wave is not known in practice, a reference measurement $h_m(n)$ was made beforehand and stored in the device memory. For that purpose, we used a large sheet of metal $\Gamma = -1$ and measured the reflection at 1 m distance. Since we have supposed wall parameters as frequency independent, we are able to determine Γ of the first surface from the peak values of the measured data:

$$\Gamma = -\frac{\|h_1(n)\|_\infty}{\|h_m(n)\|_\infty} = -\frac{\|h(n)\|_\infty}{\|h_m(n)\|_\infty}. \tag{4.2.5}$$

The reflection coefficient of a wall is always negative (compare (4.2.1) and see Fig. 4.2.5). The infinity norm is a positive number, hence the minus in (4.2.5). The determination of $h(n)$ has to be done carefully by using the same wall distance for synchronization as in the $h_m(n)$ measurement in order to respect the spreading loss of the waves. However, a distance measurement to the wall is not required, it can be easily obtained from position of $h_1(n)$.

Now, we can calculate the wall permittivity:

$$\varepsilon_{rw} = \frac{(1-\Gamma)^2}{(1+\Gamma)^2} \tag{4.2.6}$$

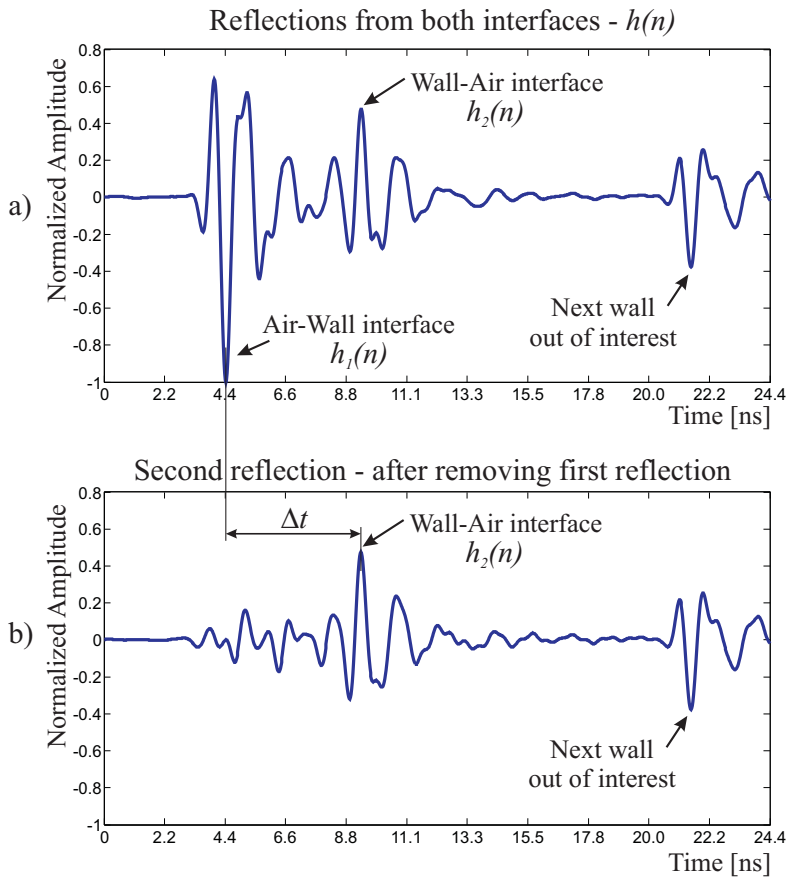

Fig. 4.2.5: Mean of reflections from wall interfaces. a) Reflection from both interfaces. b) Reflection from wall-air interface, after removing the first reflection.

and the propagation speed within the wall:

$$v_w = \frac{c}{\sqrt{\varepsilon_{rw}}}. \tag{4.2.7}$$

The propagation time Δt (see Fig. 4.2.5) within the wall will give the wall thickness:

$$D_w = \frac{v_w \Delta t}{2}. \tag{4.2.8}$$

Time Δt results from the time position of the maximum of $h_2(n)$ referred to the first reflection. However, the $h_1(n)$ and $h_2(n)$ may overlap each other as it is shown in Fig. 4.2.6. It is mostly obvious when the wall is too thin. In this case a wall thickness is only 13 cm. Therefore, we firstly subtract the first reflection $h_1(n)$ from the data in order to gain the improved reflection from the inner surface. Since the wall parameters are frequency independent, we can suppose that $h_1(n)$

and $h_m(n)$ have the same time shape, hence

$$h_2(n) \approx h(n) - \frac{\|h_1(n)\|_\infty}{\|h_m(n)\|_\infty} h_m(n) = h(n) - \frac{\|h(n)\|_\infty}{\|h_m(n)\|_\infty} h_m(n). \tag{4.2.9}$$

The norm of $h_1(n)$ may be approximated by norm of $h(n)$. As it can be seen from Fig. 4.2.6 b), even if the $h_1(n)$ and $h_2(n)$ overlap each other using formulas 4.2.9 leads to very good results in praxis (D_w=13 cm, Red small brick with plaster, Table 4.4).

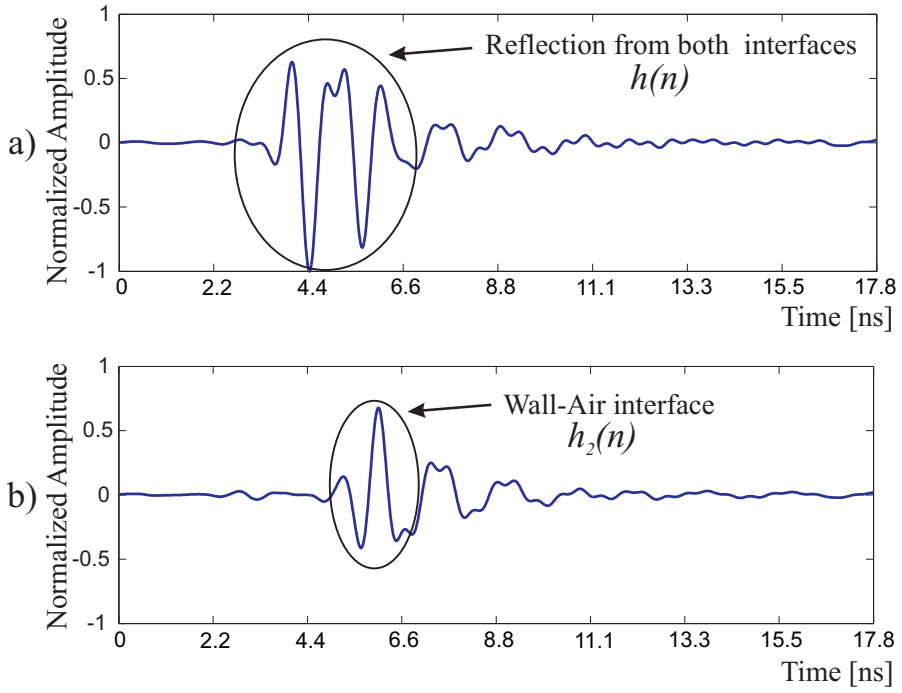

Fig. 4.2.6: Mean of reflections from wall interfaces, wall thickness $D_w = 13$ cm. a) Reflection from both interfaces. b) Reflection from wall-air interface, after removing first reflection.

The ratio between measured infinity norms of $h_1(n)$ and $h_2(n)$ could be used to calculate the wall attenuation representing the conductivity of the wall material.

$$a_w = \frac{\|h_2(n)\|_\infty}{\|h_1(n)\|_\infty} \frac{1}{1-\Gamma^2} = \frac{\|h_2(n)\|_\infty}{\|h(n)\|_\infty} \frac{1}{1-\Gamma^2}. \tag{4.2.10}$$

From (4.2.10) and (4.2.4) attenuation constant α can be computed as:

$$\alpha = \frac{\ln a_w}{-2D_w}. \tag{4.2.11}$$

From (4.2.11) and (4.2.3) wall conductivity σ_w can be computed as:

$$\sigma_w = 2\pi f \varepsilon_w \sqrt{\left(\left(\frac{\alpha}{2\pi f}\right)^2 \frac{2}{v_w \varepsilon_w} + 1\right)^2 - 1}. \tag{4.2.12}$$

4.2.5 Measurements Results

The proposed method was tested on 13 different types of walls. The walls were made of various types of bricks, concrete and reinforced concrete. The wall thicknesses ranged from 13 cm to 50 cm. Most of the walls were measured indoor, four walls were measured from outside. An M-sequence UWB radar device with 4.5 GHz sampling rate [117], frequency range 0.5 GHz to 2.25 GHz and double ridged horn antennas were used for the measurements. Five walls were also investigated with circular antennas.

For data capturing, the (handheld) radar device was simply moved towards or from the wall. Reasonable distances cover about 0.5 m to 1.5 m. The processing is completely automated and takes less than 2 seconds on a standard laptop in MATLAB. The results are shown in the Table 4.4. It can be seen, that the proposed algorithm is very robust and the error in the thickness estimation is less than 10% for most of walls. The wall parameters can be estimated precisely enough for many practical applications even when the thin layer of plaster is present. The method failed only in one case, when the wall was made of 4 cm stone pavement and then 40 cm light brick. The preciseness of the measured σ_w was not tested yet since it was not in an aim of our work up to now.

The occurred deviations are caused mainly by erroneous determination of the wall reflection resulting in permittivity and conductivity values of reduced reliability. The approach assumes an ideally flat surface and a homogeneous wall structure. If the surface is too rough or coated by some substances, there are also other quantities besides the volume material which determines the wall reflection. The use of more complex wall models may partially reduce these errors. However, under field conditions it will usually not be possible to determine all the required parameters.

The algorithm is suitable for handheld device operation without use of any additional equipment or prior knowledge. It can be applied under real conditions, the method is very robust and useful for typical walls that occur in the real environment. The whole algorithm is very fast, fully automatic and applicable under realtime conditions. The estimated parameters could be used to improve UWB through-wall SAR imaging as well as moving person detection. Possibly, the knowledge of wall permittivity and conductivity permits recognition of wall materials or estimates the material quality of the wall construction.

Table 4.4: Estimation of the permittivity, thickness and conductivity of 13 different walls.

Type of the wall	Environment Inside/Outside of the building	Estimated permittivity ε_{rw}	Estimated thickness D_w[cm]	Real thickness D_w[cm]	**Error in thickness** [%]	Estimated conductivity σ_w[mS/m]
White brick with plaster	I	3,141	41,91	40	**4,77**	7,4
Brick with plaster	I	4,11	29,24	29	**0,83**	17,9
Red small brick with plaster	I	3,46	13,24	13	**1,85**	11
Brick with plaster	I	4,95	20,97	20	**4,85**	34,5
Gray reinforced brick	O	2,46	18,46	18	**2,56**	9,3
Gray reinforced brick	O	2,71	47,75	50	**4,5**	6,8
White brick	I	3,04	22,56	25	**9,76**	17
Reinforced concrete with wallpaper	I	7,7	14,64	15,5	**5,55**	43,8
Reinforced concrete	O	7,69	14,77	15	**1,53**	46,9
Concrete	I	5,89	15,51	17	**8,76**	18,8
Concrete with plaster	I	4,72	15,48	15,7	**1,4**	12,6
Small inhomogeneous hard brick with thick mortar	I	5,58	44,14	38	**16,16**	40,5
4 cm Stone pavement, then 40 cm light brick	O	10,17	3,97	44	**-**	339

4.3 Highlighting of a Building Contours

Any actual information about a building interior could be very useful before entering dangerous area. It could be used to plan strategies in a lot of rescue and security applications. In this section, we introduce an imaging of the inner and outer building contours from the outside using through-wall UWB radar. For that purpose the preprocessing, calibration, and imaging is performed. The image processing method for highlighting of the building walls using Hough Transform (HT) with assumed knowledge about the direction of walls is presented. The algorithm was tested on real measured data acquired from a M-sequence UWB radar system.

4.3.1 Preprocessing and Imaging

Several preprocessing and calibration steps as well as imaging have to be applied before the highlighting of a building contours would be performed. After the building was scanned by SAR scanning (Section 2.3), the dataset was interpolated in time domain (Section 2.4.1), the time zero was estimated (Section 2.4.2), the crosstalk was removed (Section 2.4.3), and the dataset was deconvolved with impulse response of whole radar system (Section 2.4.4). The irregular trolley movement (Section 4.1.5) and antenna beam was compensated (Section 4.1.6). SAR imaging based on geometrical approach described in Section 2.5.2 was used as the migration.

In order to reconstruct the wave propagation through the wall more precisely, the TOA that takes into the account wall parameters was computed during SAR image formation, as it is described in Section 4.1. In addition, the attenuation of the wave propagation and looses were compensated in two ways:

Attenuation inside the wall: The wave penetrating through the wall is attenuated much more considerably in the wall than it is attenuated in the air. The attenuation inside the wall mostly depends on the wall conductivity σ_w, that can be easily measured by time domain reflectometry (Section 4.2). The magnitude of the wave behind the wall is given by (4.2.3) and (4.2.4):

$$a_w = a_0 e^{-D_w \left(2\pi f \sqrt{\frac{\varepsilon_w \mu_w}{2} \left[\sqrt{1+\left(\frac{\sigma_w}{2\pi f \varepsilon_w}\right)^2} - 1 \right]} \right)} \tag{4.3.1}$$

where a_0 is a magnitude of the incident wave before the wall and a_w is a magnitude of the wave behind the wall.

Spread losses in the air: The magnitude of the wave is reduced with distance even in the air. Such attenuation is called spread losses [67]. The spread losses for long distances such as few meters should not be neglected. A very simple and

theoretical approach was chosen for correcting the spread losses. Because most of the objects that are scanned, including walls, have flat surfaces, the spread losses could be expressed by reciprocal proportion [156]:

$$a_2 = a_1 \frac{T_2}{T_1} \tag{4.3.2}$$

where a_1 is the wave magnitude at position T_1 and a_2 is the wave magnitude at position T_2

Compensation of the wave attenuation and losses should improve the magnitudes level of all scanned objects according to their reflection properties. However, it has to be done carefully because the small magnitudes from far objects behind the wall are increased including the noise. In critical scenarios the noise and clutters from far positions could be raised into the target magnitude level.

After the preprocessed and calibrated dataset B_{PC} is migrated and attenuation and spread looses described above are compensated, the final image $I_w(X, Z)$ is obtained:

$$I_w(x_T, z_T) = \frac{1}{N} \sum_{n=1}^{N} a_w a_2 w_1 w_2 B_{PCn}\,(X, k = (TOA_{TX-T} + TOA_{T-RX})). \tag{4.3.3}$$

4.3.2 Wall Highlighting using Hough Transform

The walls that represent the building contours are mostly distorted by clutters and noise on the processed image $I_w(x_T, z_T)$. We are looking for big straight walls, with good reflections, that represent building contours. To highlight such walls we propose the following image processing steps: The image $I_w(x_T, z_T)$ is transformed to the gray-level. The edges are found with the edge detector so the picture is converted to the binary image $I_{wDE}(x_T, z_T)$. The Hough transform [129, 52] is applied. The peaks in Hough space are filtered according to the wall direction assumptions and lines which represent the investigated walls are drawn back to the $I_w(x_T, z_T)$ image.

Canny edge detector [25] is used to detect edges, as it is very often used for detection of lines in combination with HT in SAR images obtained by an aircraft [33] or for ground penetrating radar SAR scans [56].

The HT is used to find the lines in the image:

$$I_{HT} = HT(I_{wDE}(x_T, z_T)). \tag{4.3.4}$$

HT is a feature extraction technique used in image analysis, computer vision, and digital image processing [129, 52]. HT is mostly used for finding straight lines (or certain class of shapes) hidden in larger amounts of other data. The main advantage of the HT technique is that it is tolerant to gaps in feature boundary

descriptions and is relatively unaffected by image noise [58]. The motivating idea behind the Hough technique for line detection is that each input point in the image indicates its contribution to a globally consistent solution (e.g. the physical line which gave rise to that image point). A line segment can be described analytically in a number of forms. However, a convenient equation for describing a set of lines uses parametric or normal notion [58]:

$$x\cos(\theta) + z\sin(\theta) = r \tag{4.3.5}$$

where r is the distance from the origin to the line along a vector perpendicular to the line. θ is the angle of the perpendicular projection from the origin to the line measured in radians clockwise from the positive X-axis (see Fig. 4.3.1).

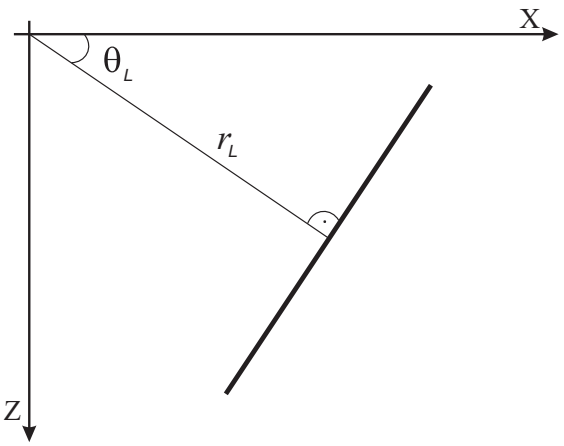

Fig. 4.3.1: Parametric description of a straight line.

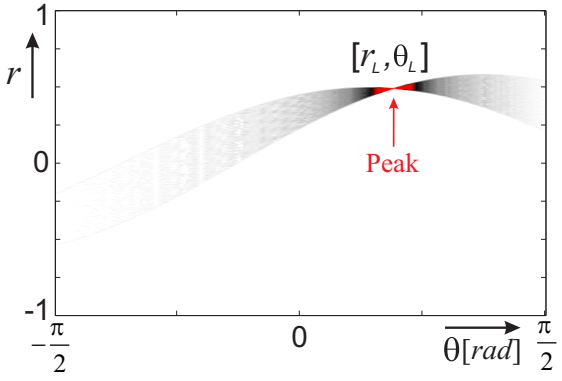

Fig. 4.3.2: Hough transform of a straight line from Fig. 4.3.1.

The range of theta is $-\pi/2 \leq \theta < \pi/2$. The angle of the line itself is $\theta + \pi/2$, also measured clockwise with respect to the positive X-axis. The possible plotted

(r, θ) values defined by each (x, z) map points in the Cartesian image space to curves (i.e. sinusoids) in the polar Hough parameter space. This point-to-curve transformation is the HT for straight lines. Resulting peaks in the Hough space represent a corresponding straight line in the investigated image [58].

The points (x, z) representing the line in Fig. 4.3.1 are transformed in Hough space into the number of sinusoids shown in Fig. 4.3.2. As can be seen, the maximum of summed sinusoids represents a peak at (r_L, θ_L) position corresponding to the line in (X, Z) space. The longer the lines are, the higher the peaks will be. Lower peaks are considered to be shorter lines and thus are not interesting for our purpose, because we are looking for long and straight walls.

The main idea of this section is to use the assumed information about the wall directions, which would considerably reduce falsely detected lines. Almost all buildings have all walls parallel, or perpendicular to the main outer walls. This means, that almost all of the walls are perpendicular or parallel to each other in one building. The radar scan is done alongside the one (or more) outer wall(s), as it is shown in Fig. 4.3.3 a). Therefore, there is a high probability that peaks in Hough space representing the scanned walls would be approximately at positions where the wall angle is equal to:

$$\theta_w = 0 \; and \; \pm \frac{\pi}{2}. \tag{4.3.6}$$

as it is shown in Fig. 4.3.3 b).

The easiest way to reduce all of the lines that are not perpendicular, or in parallel with the wall along which the scan is done, is to clear all points in Hough space, that are not close to the θ_w. For that purpose, sharp window functions with peaks at θ_w are used. The final window function W_H is made up from Hanning window functions as it is shown in Fig. 4.3.4. The investigated walls from image I_{HT} in Hough space are then raised up from noise and clutters by window function W_H:

$$I_{WHT}(r, \theta) = I_{HT}(r, \theta) W_H(r, \theta). \tag{4.3.7}$$

The peaks found in Hough space are then transformed by the Inverse Hough Transform (IHT) back to the (X, Z) space as a certain number of straight lines:

$$I_F(x_T, z_T) = IHT(I_{WHT}(r, \theta)). \tag{4.3.8}$$

These lines could be drawn over the original image, so the wall would be found much more easy.

The sequence of processing steps from SAR scanning to obtain the final image with the detected building contours is shown in Fig. 4.3.5.

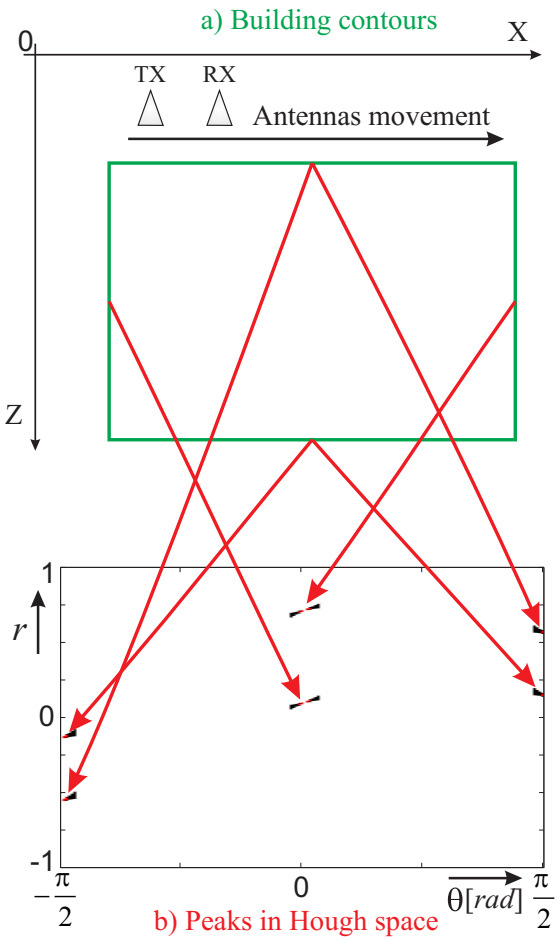

Fig. 4.3.3: Hough transform of the building contours. a) The building contours scanned from outside. b) The peaks in Hough space of the scanned image.

4.3.3 Measurements Results

For testing of the proposed algorithm, the M-sequence UWB radar system [43, 116, 118] with frequency band DC − 2.25 GHz was used. The next scenarios were measured for project RADIOTECT in Stockholm Rescue Center in Sweeden.

The wooden building shown in Fig. 4.3.6 was scanned from three sides (Fig. 4.3.7 a)). A bistatic model and the horn antennas with frequency band 0.3 − 3 GHz were used.

Interpolation with oversampling factor $KO = 10$ described in Section 2.4.1 was performed. The next preprocessing steps such as shifting to time zero (Section 2.4.2), crosstalk removing (Section 2.4.3), and deconvolution by radar impulse response (Section 2.4.4) were processed. 2D SAR migration in time domain described in Section 2.5.2 with precise TOA through-wall computation described in

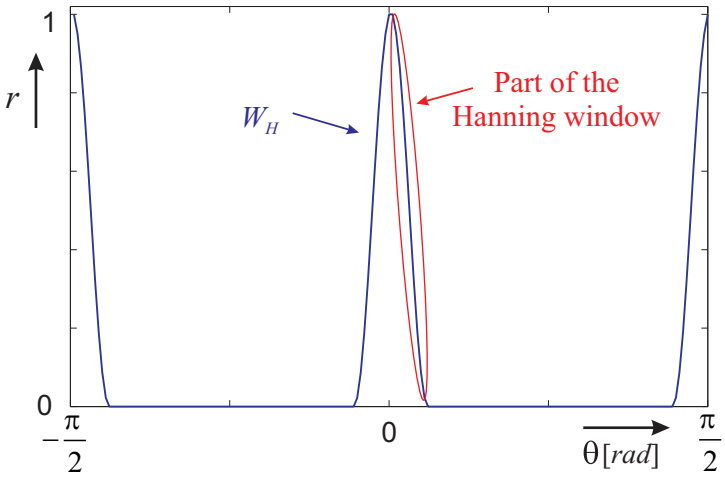

Fig. 4.3.4: Window function W_H made up from Hanning window functions.

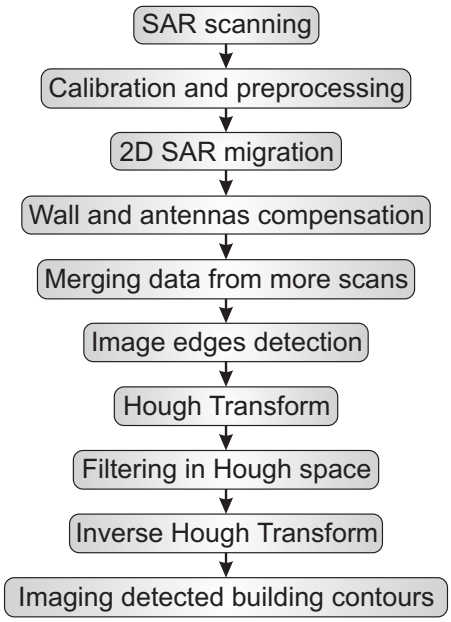

Fig. 4.3.5: Processing steps for imaging of building contours.

Section 4.1, antenna beam compensation (4.1.16), and attenuation losses compensation (Section 4.3.1) were computed for all the scans.

The migrated images from three scans were merged together (Fig. 4.3.7 b)) and edges were detected (Fig. 4.3.7 c)). The HT was applied (Fig. 4.3.8 a)) and the peaks in positions close to θ_w were filtered with a sharp window function W_H (Fig. 4.3.8 b)). The lines that represent the building walls were drawn over the migrated image after the IHT was performed (Fig. 4.3.8 c)).

Fig. 4.3.6: Photos of scanned building. Stockholm Rescue Center - Sweeden.

It is obvious that the migrated image (Fig. 4.3.7 b)) without additional image processing is very hard to interpret. The detected walls drawn in red (Fig. 4.3.8 c)) help to highlight the contours of the scanned building.

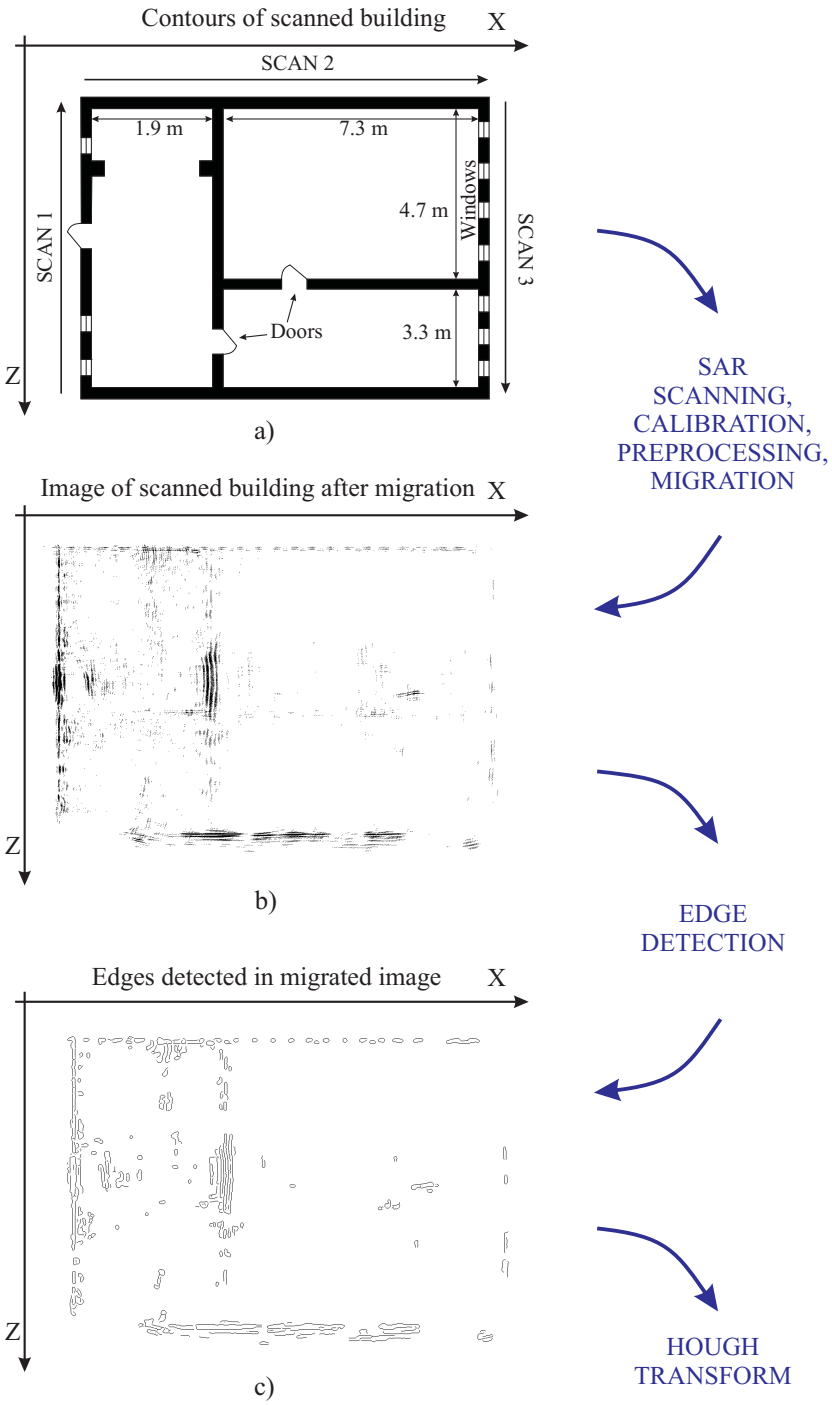

Fig. 4.3.7: Steps of highlighting the building walls in the scanned image. a) The real contours of the scanned building. b) The image of the scanned building merged from three scans. c) The edges detected in the image b) by Canny detector.

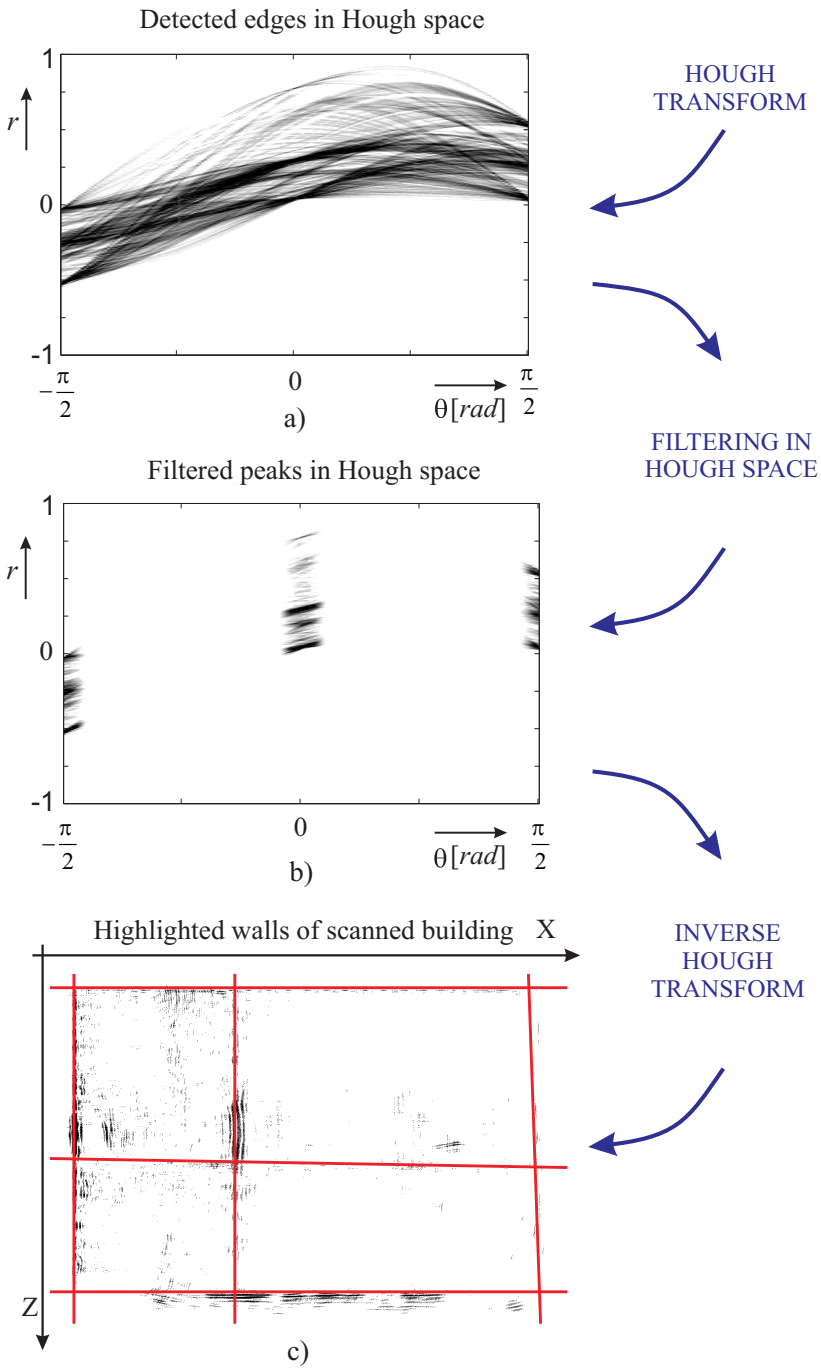

Fig. 4.3.8: Steps of highlighting the building walls in the scanned image, part 2. a) The Hough Transform performed on the detected edges. b) The peaks in Hough space filtered by a sharp window function. c) The highlighted walls drawn over the scanned image obtained by Inverse Hough Transform.

4.4 Measurements of the Practical Scenarios

4.4.1 Comparison of Basic Imaging Methods

As we have shown in Section 2.5 there is vast amount of methods that could transform measured SAR data back to the measured scenario. In this section we will show the results of several migration methods on the same measurement scenario, as we published in [137]. Three basic inversion methods will be compared: Kirchhoff migration (Section 2.5.5), Stolt migration (Section 2.5.6) also called f-k migration, and SAR imaging (Section 2.5.2) with simple geometrical approach.

In order to evaluate the imaging methods and compare their results, we introduced two parameters: the Signal to Clutter Ratio (SCR), which is defined as the ratio of energy between the estimated regions of the objects and the clutter regions close to the object. The second parameter is the Relative Positioning Error (RPE), which is defined as the ratio between the error in the object position estimation and the object real position. A good reconstruction method should have a large SCR and a small RPE. The computational complexities of imaging methods are also compared.

The measurements were done with the 9 GHz M-sequence UWB radar system [43,116,118] described in Section 2.1.3. The measurements were done in Electronic Measurement Research Lab, TU Ilmenau, Germany. Bistatic model with double-ridged horn vertical assembled antennas shown in Fig. 4.4.1 was used. The same scenario as to prove the precise through-wall TOA estimation in Section 4.1.7 was used. However, the metal plate behind the wall is clearly visible (Fig. 4.1.11)

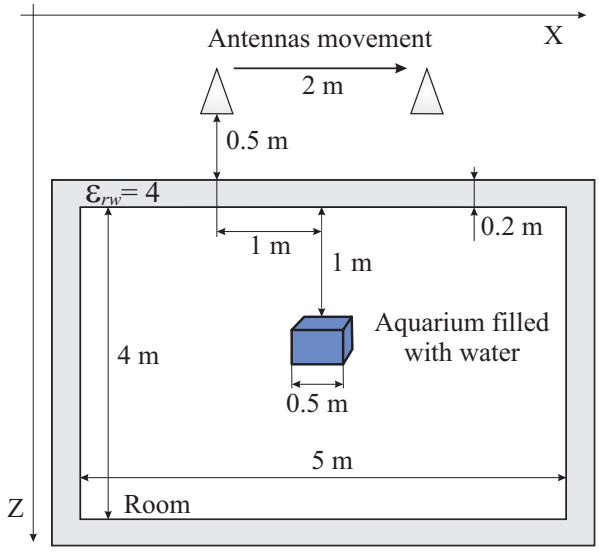

Fig. 4.4.1: SAR measurement scenario, aquarium filled with clear watter behind the wall.

and most of the imaging methods would provide very similar results. Therefore, a smaller and worse scatterer for electromagnetic waves was used. We have chosen the aquarium filled with clear water placed behind the wall to compare the imaging capabilities. The simplified sketch of the measurement scenario is shown in Fig. 4.4.1. The photos from the measurements are shown in Fig. 4.4.2.

a) b)

Fig. 4.4.2: SAR measurement. a) Radar system in front of the wall. b) Aquarium filled with water behind the wall.

The vertical antenna system was moved in parallel to the wall at distance 50 cm from the wall. The aquarium was placed behind the wall in the middle of the moving path of the system and 1 m far from the wall. The aquarium has size $50 \times 30 \times 30$ cm and is placed on wooden console.

In SAR imaging and Kirchhoff migration the estimation of travel time through the wall described in Section 4.1 was used. However, in Stolt migration, the implementation of this method is not possible. Therefore, the simple wall compensation method described in Section 2.5.3 was used.

The results from SAR imaging, Kirchhoff migration, and Stolt migration with and without wall compensation are shown in Fig. 4.4.3. The cross-range results of migrations with wall compensation are shown in Fig. 4.4.4. Even if the aquarium filled with clear watter is a weak scatterer in comparison with a metal plate it is visible after all migrations as well as the rear wall. However, the aquarium is most clearly visible after the SAR imaging and Kirchhoff migration. After Stolt migration the aquarium is visible only weakly. The SAR imaging and the Kirchhoff migration with precise wall compensation show objects very closely to the real positions. The aquarium is shown shifted only about 2 cm away from its real position. Stolt migration with simple wall compensation shows aquarium 3 cm away from its real position. However, because the principle of compensation method, also the front wall is shifted, but to a wrong position, approx. 20 cm forward comparison to its real position. Migration without wall compensation shifts objects behind the wall approx. 20 cm away (in Z direction) from their real positions. The RTE and SCR of aquarium for all migrations are shown in Table

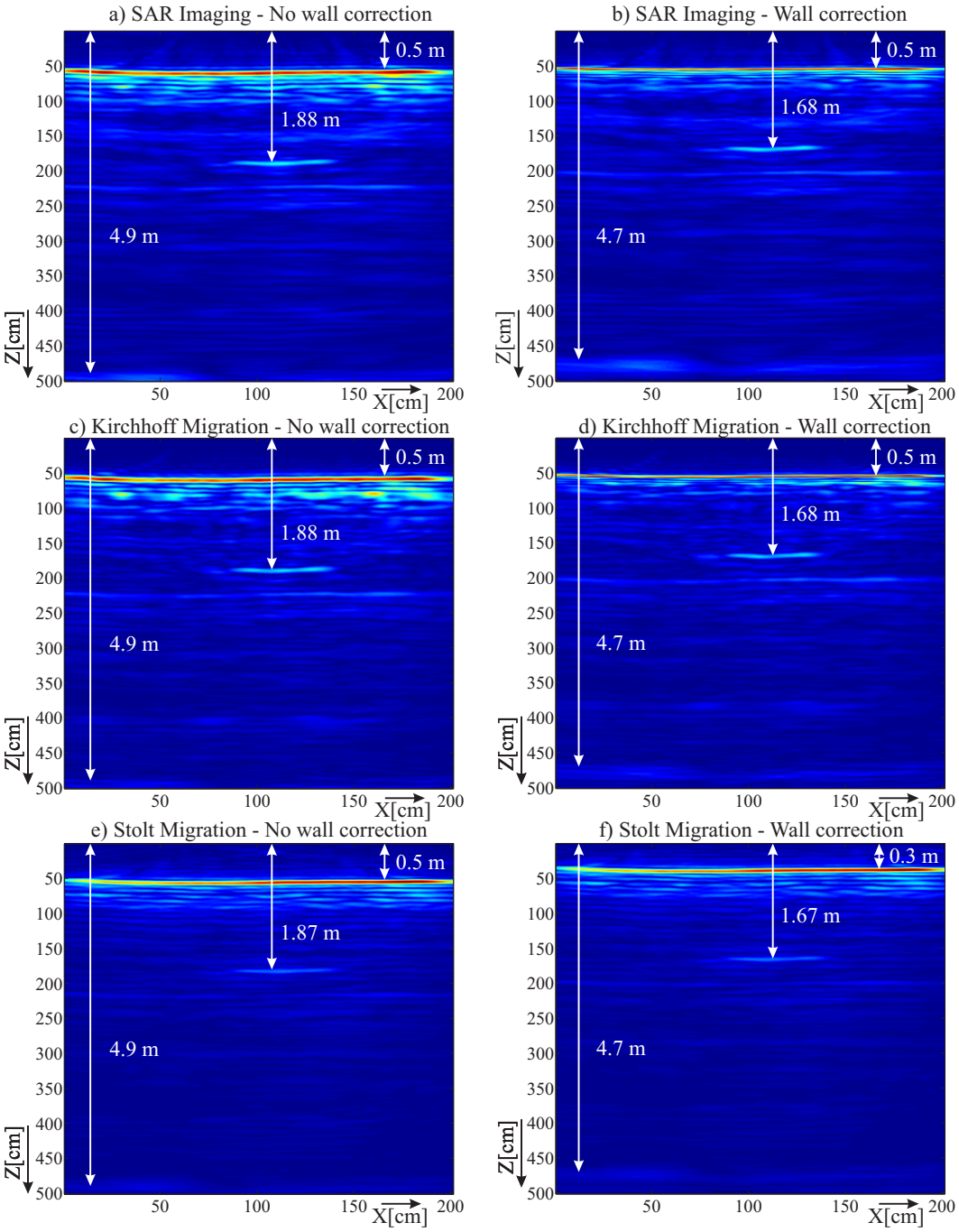

Fig. 4.4.3: Aquarium filled with clear water. a) SAR Imaging without wall compensation. b) SAR Imaging with wall compensation. c) Kirchhoff Migration without wall compensation. d) Kirchhoff Migration with wall compensation. e) Stolt Migration without wall compensation. f) Stolt Migration with wall compensation.

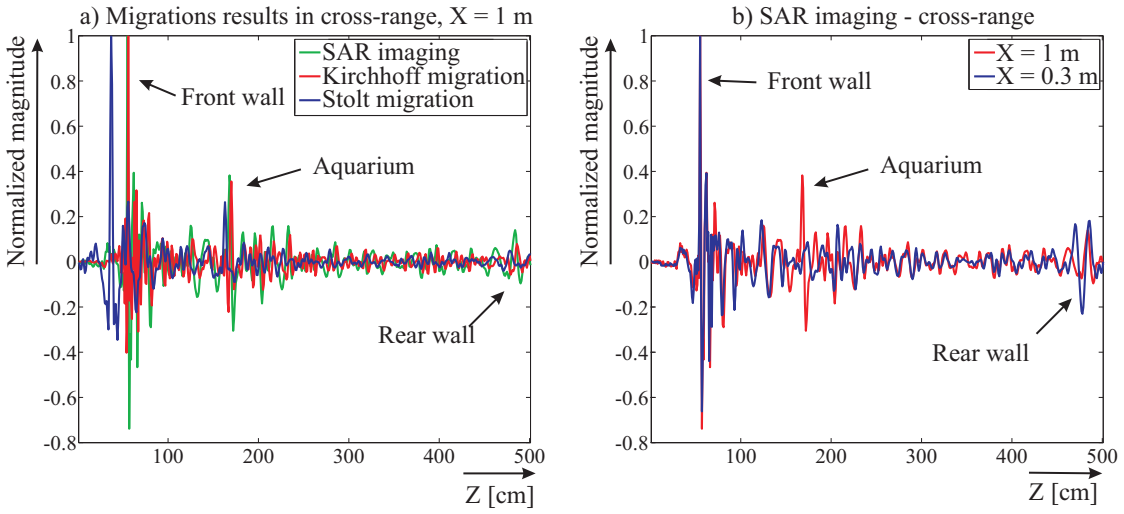

Fig. 4.4.4: Aquarium filled with clear water. Migrations with wall compensation. a) Migrations results in cross-range, X = 1 m. b) SAR imaging - cross-range.

4.5. SCR for SAR imaging and Kirchhoff migration are very similar and close to

Table 4.5: SCR, and RPE of Aquarium for considered migrations.

Methods	No wall compensation		With wall compensation	
	RPE	SCR	RPE	SCR
SAR imaging	10.59 %	5.00	1.18 %	4.74
Kirchhoff Migration	10.59 %	5.19	1.18 %	4.78
Stolt Migration	10.00 %	3.99	1.77 %	4.26

the 5. The values of the SCR depend on the regions in which they are calculated. However, it can be seen that the rear wall is better visible after SAR imaging. Even if the Kirchhoff migration gives a slightly better SCR, it seems to produce a bit more noise in clutter regions. However, this is strongly subjective.

Computational time required for migration of the shown scenario with image resolution $N_x \times N_z = 201 \times 501$ and number of scans $N = 200$ is shown in table 4.6. Migrations were computed in MATLAB on PC with 2.33 GHz Intel processor. SAR imaging and Kirchhoff migration are the slowest methods, while the Stolt migration is the fastest. It is faster even than the fast back projection described in Section 2.5.12, however it provides the worst results. It can be seen that implementation of the wall compensation into the migrations do not extent computational time more than about 65 %. Note that methods were not optimalized for fast computations and they were computed in MATLAB. Implementation of the methods on special

Table 4.6: Computational time and complexity for considered migrations. Note that for Stolt migration only a simple wall compensation (Section 2.5.3) was implemented.

Methods	Computational complexity	No wall compensation	With wall compensation
SAR imaging	$O_{SAR}(N_x N_z N)$	530.1 s	856.7 s
Kirchhoff Migration	$O_{Kir}(N_x N_z N)$	539.4 s	871.6 s
Stolt Migration	$O_{Sto}(N_x N_z log_2 N)$	3.69 s	3.69 s

hardware would significantly minimize the computational time. Moreover, such high image resolution should not be required for most of the practical applications.

SAR imaging is geometrically based whereas Kirchhoff and Stolt migrations are based on wave equations and should provide better results from theoretical point of view. From measured results it can be seen, that SAR imaging and Kirchhoff migration provides almost identical results. Note that the methods were tested only on one scenario. It is possible to expect different results from another scenarios.

4.4.2 Imaging of the Objects Behind a Brick Wall

In this section the several objects behind 20 cm brick wall with relative permittivity approx. 4 were scanned with UWB radar system and then processed. The measurements were done in Electronic Measurement Research Lab, TU Ilmenau, Germany. Attention is paid to show which kind of objects behind the brick wall can be imaged with UWB radar. A correctly chosen method to interpret the migrated images will be also discussed.

The same measurement environment as for comparison of basic migrations shown in Fig. 4.4.1 were chosen for testing. Six objects were scanned through the wall: 30 cm × 30 cm × 50 cm aquarium filled with clean water, a wooden cupboard 160 cm × 92 cm × 42 cm with glassy doors and small metallic handles scanned from two sides, an iron fire extinguisher 14 cm in diameter with a height of 55 cm, two metallic boxes one on the top of the other, a metallic sheet 100 cm × 50 cm, and a sphere of 20 cm in diameter covered with aluminum foil.

The SAR imaging with precise TOA estimation described in Section 4.1 was computed after the all preprocessing steps described in Section 2.4 were undertaken. The antenna beam was also compensated according to the equation (4.1.16) during migration. The results from measurements are shown in Appendix A.

There are many ways how to interpret migrated images. All the objects are imaged by five different ways in order to point out how the migrated images can

differ depending on the chosen interpretation method. Subfigure a) e.g. Fig. A.0.1 a) shows the photo of object behind the wall. Subfigure b) e.g. Fig. A.0.1 b) shows 1D cross-range plot mostly at position X = 1 m what corresponds to the object position and X = 0.3 m what corresponds to the position where object is absent. Subfigure c) e.g. Fig. A.0.1 c) shows 2D image of the scanned environment including the target, the front and the rear wall. After migration the image consists from positive and negative values. Dividing values into the both positive and negative do not have any physical interpretation in image. Therefore, an absolute value from Hilbert transform is imaged here in order to be closer to the "energy" representation. Subfigure d) e.g. Fig. A.0.1 d) shows the same 2D image as in c). However, only a zoomed region where the object occurs is imaged. The colormap is also changed in order to enhance the target visibility. Subfigure e) e.g. Fig. A.0.1 e) shows 3D image of scanned environment including the target, the front and the rear wall. The third dimension represents the "magnitude" of the image. Both, the positive and the negative values are imaged. Colormap differs from the one used in subfigures c). Subfigure f) e.g. Fig. A.0.1 f) shows the same 3D image as in c). However, only a zoomed region where the object occurs is imaged. Such representation helps to concentrate on the object especially when the front wall dominates in the migrated image.

From the Figures in Appendix A it can be seen that the most visible objects behind the brick wall are the metallic ones with the flat surface placed in parallel with the scanning direction. The metallic fire extinguisher with rounded surface is also clearly visible. However, a small sphere covered with aluminum foil with diameter only 20 cm is almost invisible behind a such wall. Subfigures A.0.7 b), d), and f) can help to find the position of the sphere. Even if the wooden cupboard is the biggest object that was scanned, the wood and glass are not a good reflectors for electromagnetic waves at such frequencies. Therefore, the magnitudes of cupboard in both directions are similar with much smaller objects but the metallic ones, sometimes even smaller. A clear watter is not the best conductor for direct current, however even the small aquarium filled with clear watter is a good reflector for electromagnetic waves at the used frequencies. The dimensions of the objects in scanning - X direction can be estimated with relatively good precision. However, dimensions of the objects in looking - Z direction can be estimated very difficultly from the migrated images. It is because of a most of the energy reflected from the front surface of the object and only hardly penetrate into the object, reflect from the rear surface and penetrate back to the receive antenna through the object and the wall. Such handicap can be eliminated by scanning of the objects from at least two sides.

Based on the previous analysis, the most of the objects in the room could be imaged with the UWB radar device through the brick wall. The methods for image representation should be chosen according to the scanned objects and also

according to the required application. The 2D view is suitable image representation method for most of the objects. For weakly reflecting objects 1D view, or zoomed 2D or 3D view provide a good solution. 3D view with rotation and zooming option could provide the best solution when it would be possible to implement it in radar device with relatively simple controlling.

4.4.3 Imaging of the Object Behind a Concrete Wall

The results from scanning of the metal cabinet behind the 60 cm thick concrete wall are shown in this section. The relative permittivity of the wall was approx. $\varepsilon_{rw} = 7.7$ and wall conductivity approx. $\sigma_w = 33.2$ mS/m. The metal cabinet has dimension approx. 60 × 40 × 50 cm. The measurement was provided by the International Research Centre for Telecommunications and Radar, Delft University of Technology in the Netherlands with M-sequence UWB radar described in Section 2.1.3. Bistatic radar with horn antennas and clock frequency $f_c = 4.5GHz$ was used. The measurement scenario can be seen in Fig. B.0.1 a). The object behind the wall was scanned by 4 m horizontal antennas movement.

The SAR imaging with precise TOA estimation described in Section 4.1 was computed after the all preprocessing steps described in Section 2.4 were undertaken. The antenna beam was also compensated according to the equation (4.1.16) during migration. The results from measurements are shown in Appendix B.

2D view of migrated image is shown in Fig. B.0.1 b). Here, the whole measurement scenario including the front wall and the metal cabinet is figured. In order to focus on the scanned object the zoom in Z direction from Z = 0.8 m - 4 m is shown in Fig. B.0.1 c). In this case only the metal cabinet without front wall is visible.

It can be seen that the metallic objets could be imaged with UWB radar even behind the 60 cm concrete wall if the appropriate colormap is chosen.

4.4.4 Imaging of the Object Behind a Wooden Door

The results from scanning of the metal cabinet behind the wooden door are shown in this section. The measurement was provided by the International Research Centre for Telecommunications and Radar, Delft University of Technology in the Netherlands with M-sequence UWB radar described in Section 2.1.3. Bistatic radar with horn antennas and clock frequency $f_c = 4.5GHz$ was used. The measurement scenario can be seen in Fig. C.0.1 a). The object behind the door was scanned by the 1.5 m vertical antennas movement.

The SAR imaging without the wall compensation was computed after the all preprocessing steps described in Section 2.4 were undertaken. The antenna beam was also compensated according to the equation (4.1.16) during migration. The results from measurements are shown in Appendix C.

2D view of migrated image is shown in Fig. C.0.1 b). Here, the empty room without metal cabinet behind the door is figured. In order to compare the signals strength between reflections from door and from metal cabinet behind the door the complete scenario with object behind the door with the same colormap is shown in Fig. C.0.1 c).

It can be seen that most of the energy penetrate through the wall and reflect back from the metal cabinet. There are many situations where an entrance door are barricaded by a metallic furniture. UWB radar device could helps us to investigate if the door are barricaded before entering a hazardous environment.

Chapter 5

Original Contributions of Dissertation

The thesis was concentrated on imaging of the objects through the opaque wall with UWB radar device. The thesis represents the compact publication and could provide a good basis for studying new techniques in this topic. Extensive state of the art provides an overview of all calibration, preprocessing and processing steps required for through-wall imaging. The detailed review of known migrations that could be used for through-wall imaging presented in state of the art could be a good starting point for all researchers in such new topic as through-wall imaging is. The aim of the thesis was to develop a new methods or improvements in signal processing techniques that are carried out between the receiver part and the visual display unit. According to the author's best knowledge, the original contributions of the presented thesis could be summarized as follows:

- Development of the new, effective, and precise method for estimation of TOA through the wall that is required for precise migration, with small computation complexity, that can be used for practical applications.
- Development of the new, fast, precise, and easy to handle measurement method for estimation the wall parameters required for precise TOA through-wall estimation. Because of its very low computational requirements it can be used in realtime for practical applications.
- Development of the image processing method for highlighting the building contours in order to enhance the wall visibility of a building scanned from outside.
- Performance analysis of the developed methods on real measurements based on practical scenarios in comparison with conventional methods. The limitations of the present through-wall imaging methods based on practical measurements were also shown.

5.1 Conclusion and Future Work

Through-wall imaging is new, but very promising field for rescue and security applications. Information about current state inside the building in hazardous environment could save many human lives. In order to obtain more precise information about the indoor environment, several improvements in signal processing techniques are required. It was shown how to improve the results of through-wall imaging and still preserve realtime processing that can be used in praxis. Even if similar approaches lead mostly to highly theoretical methods that can be barely implemented in praxis, we were concentrated on developing of methods, that we have already implemented for practical scenarios and tested by real measurements.

Imaging of the stationary objects behind the wall is in comparison with detection of moving objects much more problematic. However, the proposed methods such as the measurements of the wall parameters, or the estimation of TOA through the wall could be profitably used to enhance a precision for detection, localization, and tracking of moving objects behind the wall.

There are lots of applications where the imaging of the objects through the opaque obstacles could be used. It seems that the radar with the electromagnetic waves penetration is a good way to achieve it. However, all the required techniques need to be improved in a large scale. We suggest the next steps for future work:

- To include the multilayer model approach for the measurements of the wall parameters. This would provide thickness, permittivity and conductivity for every layer of the wall such as plaster, air cavity, glass-wall, etc.
- To include the multilayer model of the wall into the precise TOA estimation.
- Compensation of the antenna angle beam should take into account that the antenna weight function is dependent also on frequencies. Especially at the low frequencies the antenna has significantly different weight function.
- The migration that takes into account multiple reflections between objects and diffraction should be investigated.

Because the topic is relatively new, there are a lot of opportunities. All the signal processing steps including calibration, preprocessing, migration, and image representation as well as the radar hardware itself have great abilities for future improvements. It can be expected that more sophisticated methods with much larger computational requirements would be investigated in the future. They will require more powerful hardware that is available now. However, keep in mind that the future is closer than you think.

Appendix A

Imaging of the Objects Behind 20 cm Brick Wall

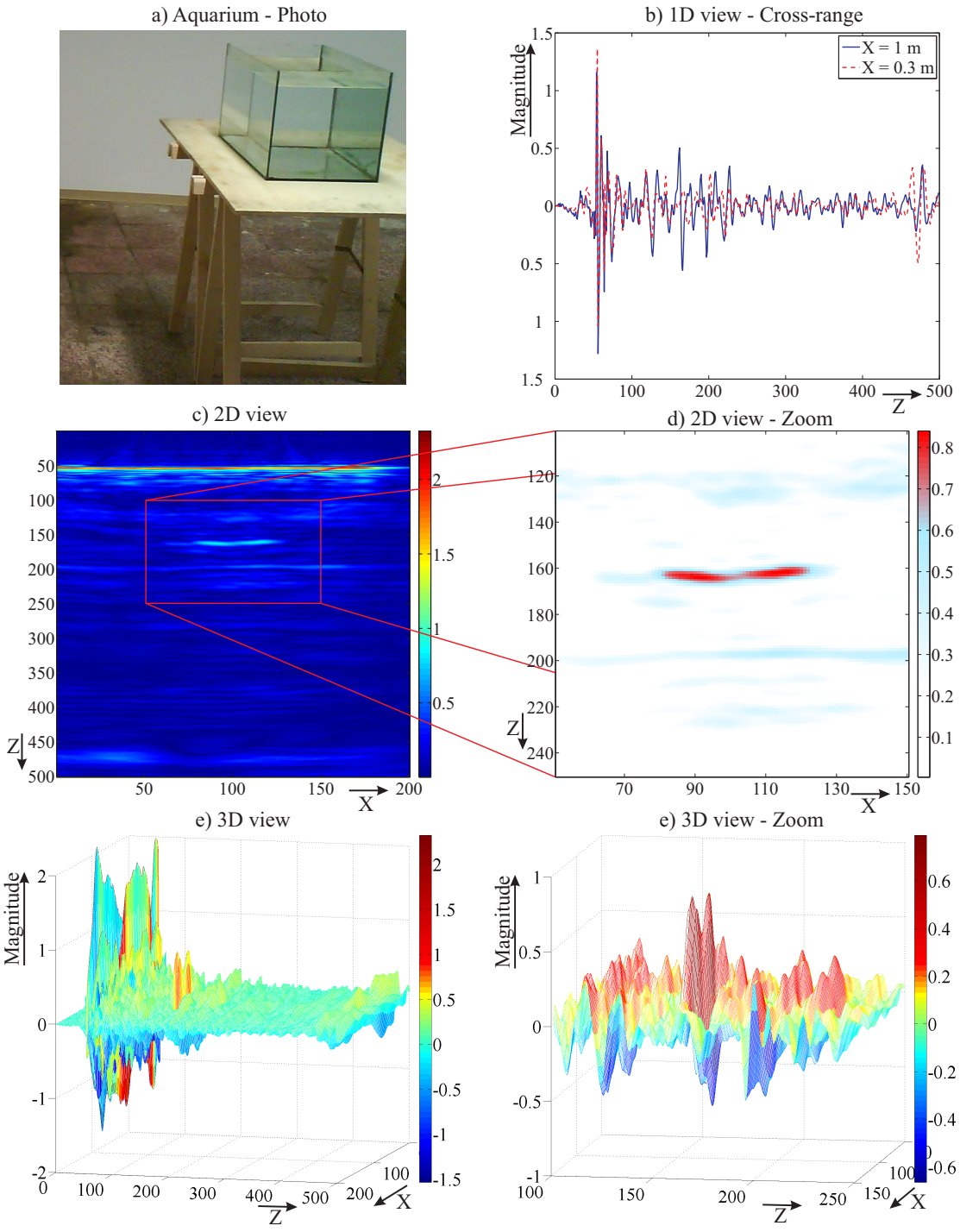

Fig. A.0.1: SAR imaging of the aquarium filled with a clear water. a) Photo. b) 1D view, Cross-range X = 1 m and X = 0.3 m. c) 2D view. d) Zoomed 2D view. e) 3D view. f) Zoomed 3D view.

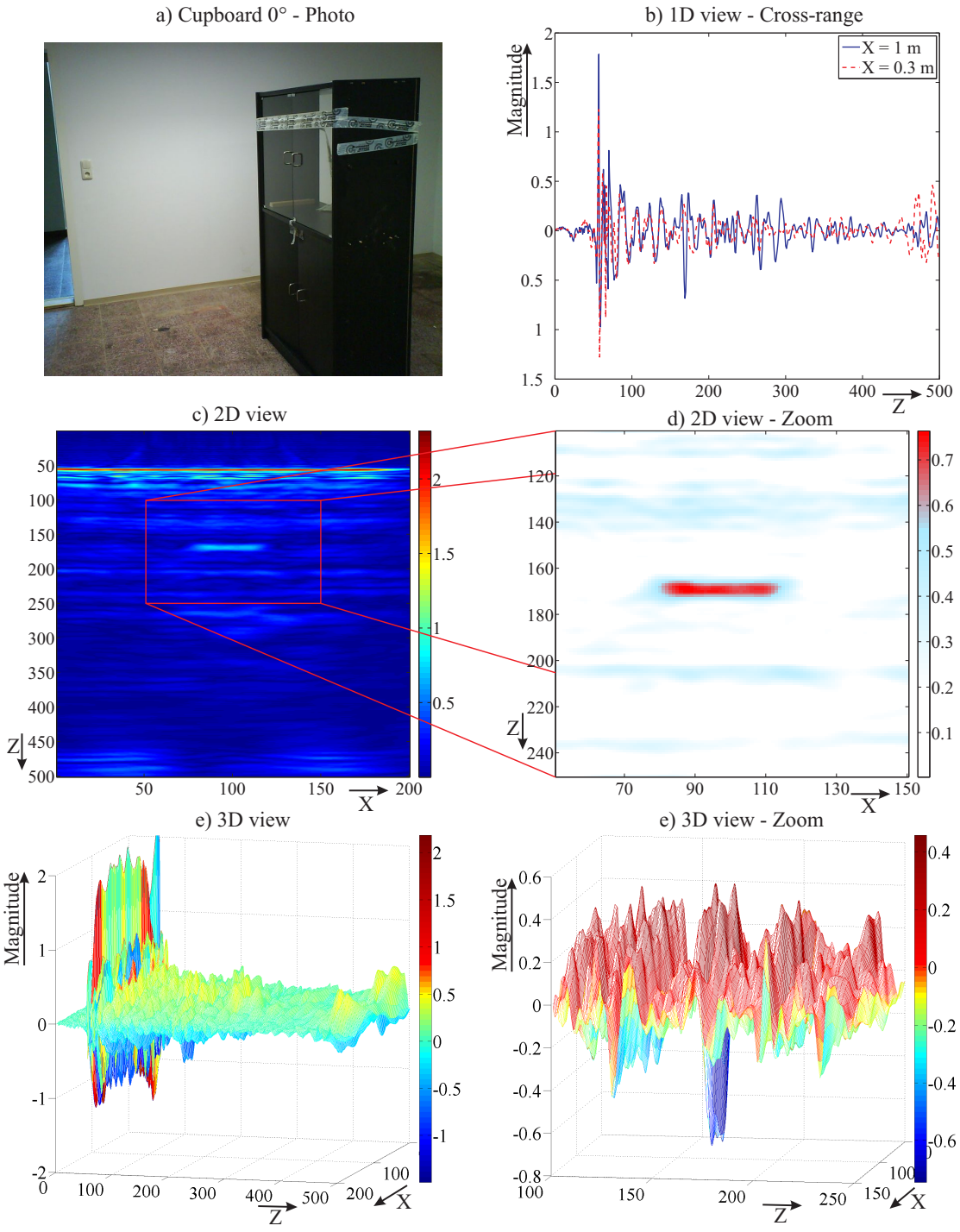

Fig. A.0.2: SAR imaging of the wooden cupboard perpendicular to the wall. a) Photo. b) 1D view, Cross-range X = 1 m and X = 0.3 m. c) 2D view. d) Zoomed 2D view. e) 3D view. f) Zoomed 3D view.

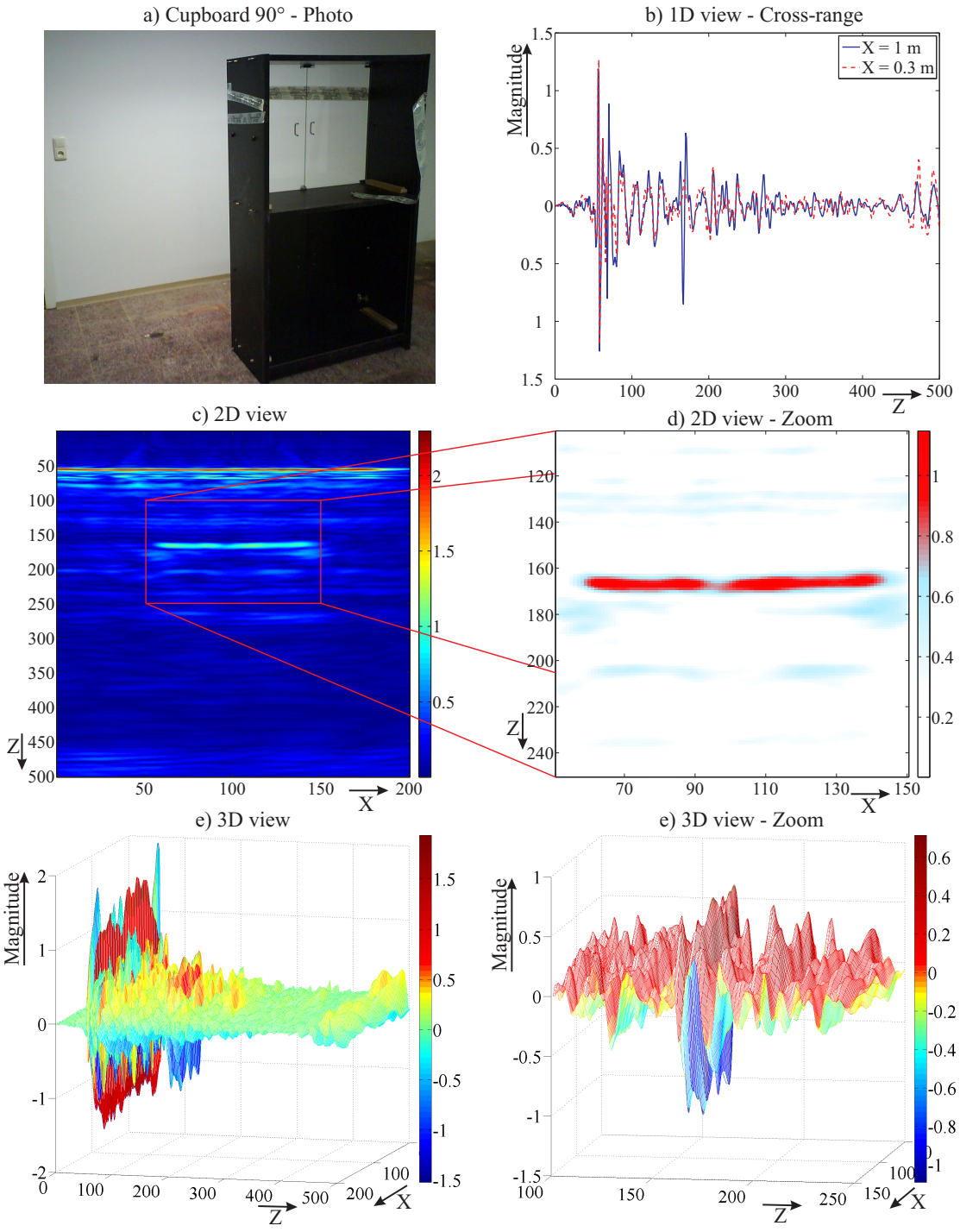

Fig. A.0.3: SAR imaging of the wooden cupboard in parallel to the wall. a) Photo. b) 1D view, Cross-range X = 1 m and X = 0.3 m. c) 2D view. d) Zoomed 2D view. e) 3D view. f) Zoomed 3D view.

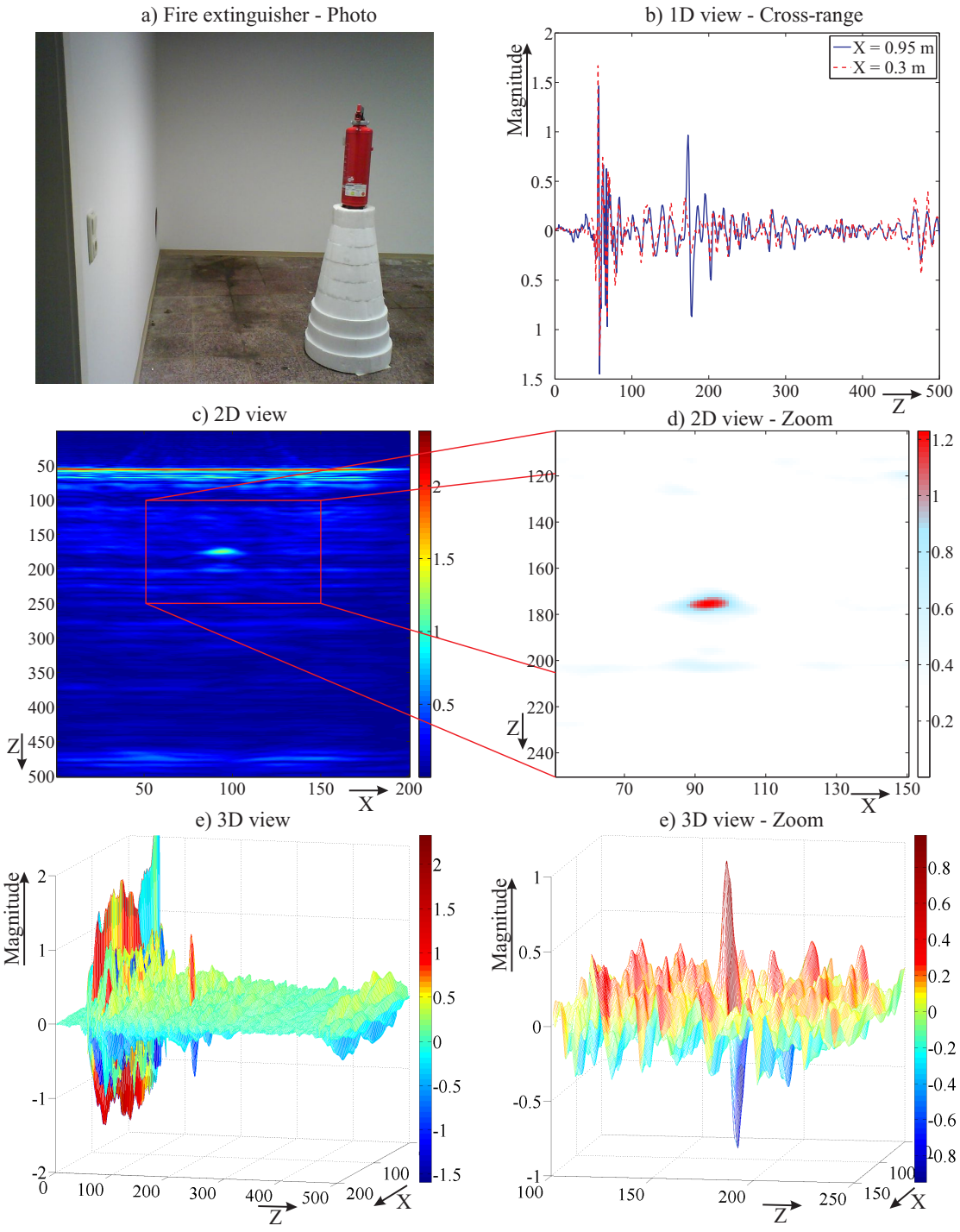

Fig. A.0.4: SAR imaging of the metallic fire extinguisher. a) Photo. b) 1D view, Cross-range X = 0.95 m and X = 0.3 m. c) 2D view. d) Zoomed 2D view. e) 3D view. f) Zoomed 3D view.

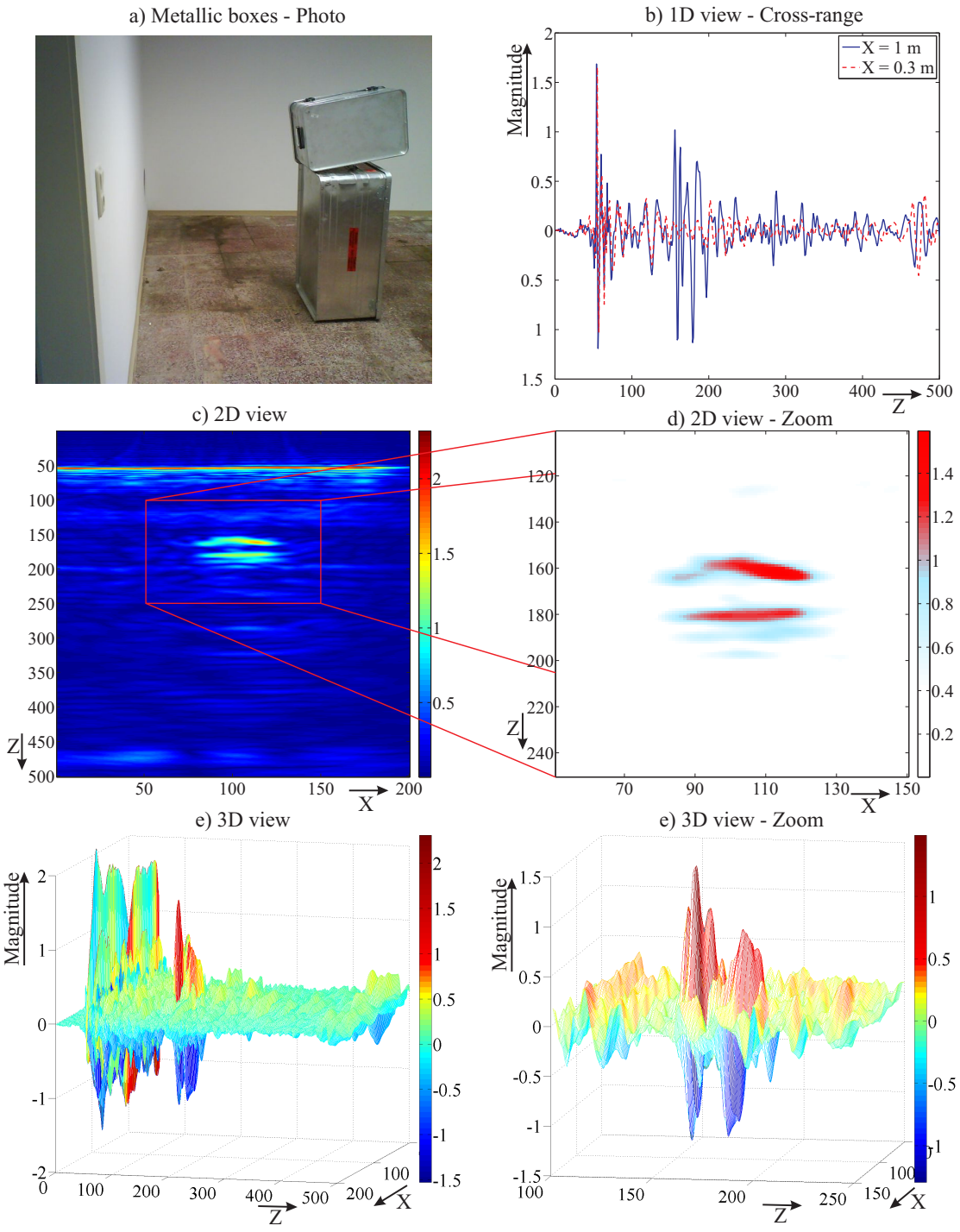

Fig. A.0.5: SAR imaging of the metallic boxes. a) Photo. b) 1D view, Cross-range X = 1 m and X = 0.3 m. c) 2D view. d) Zoomed 2D view. e) 3D view. f) Zoomed 3D view.

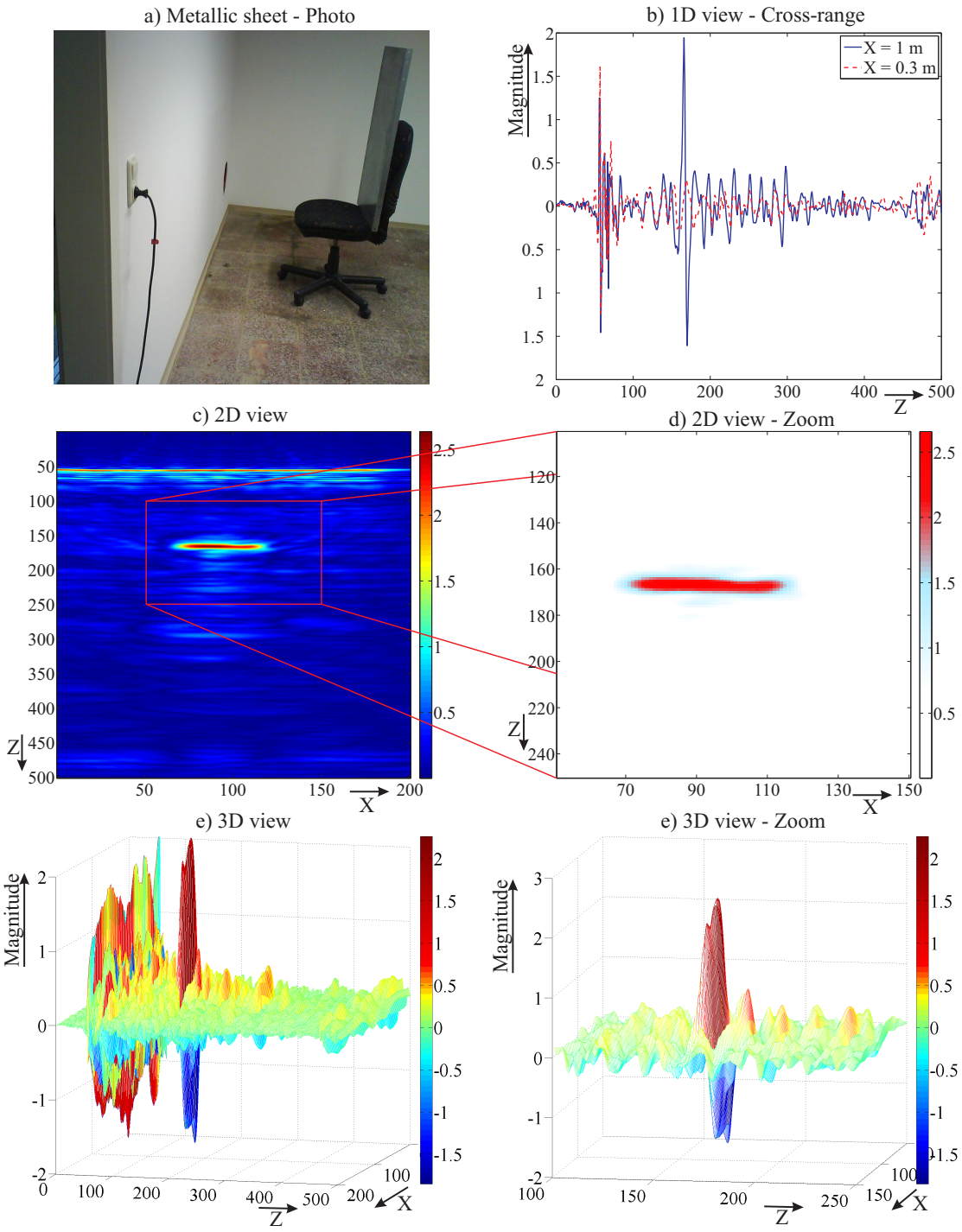

Fig. A.0.6: SAR imaging of the metallic sheet. a) Photo. b) 1D view, Cross-range X = 1 m and X = 0.3 m. c) 2D view. d) Zoomed 2D view. e) 3D view. f) Zoomed 3D view.

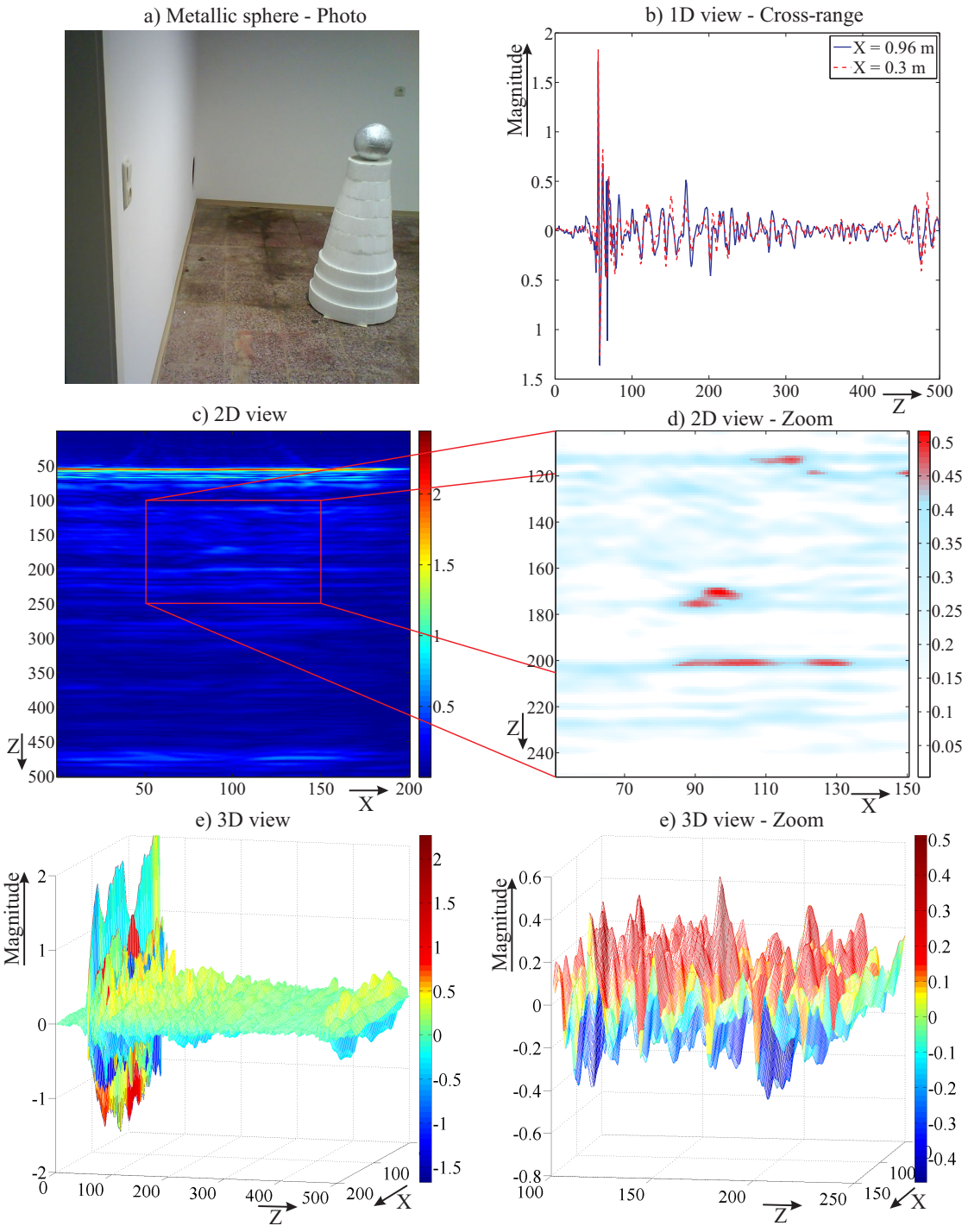

Fig. A.0.7: SAR imaging of the metallic sphere. a) Photo. b) 1D view, Cross-range X = 0.96 m and X = 0.3 m. c) 2D view. d) Zoomed 2D view. e) 3D view. f) Zoomed 3D view.

Appendix B

Imaging of the Object Behind 60 cm Concrete Wall

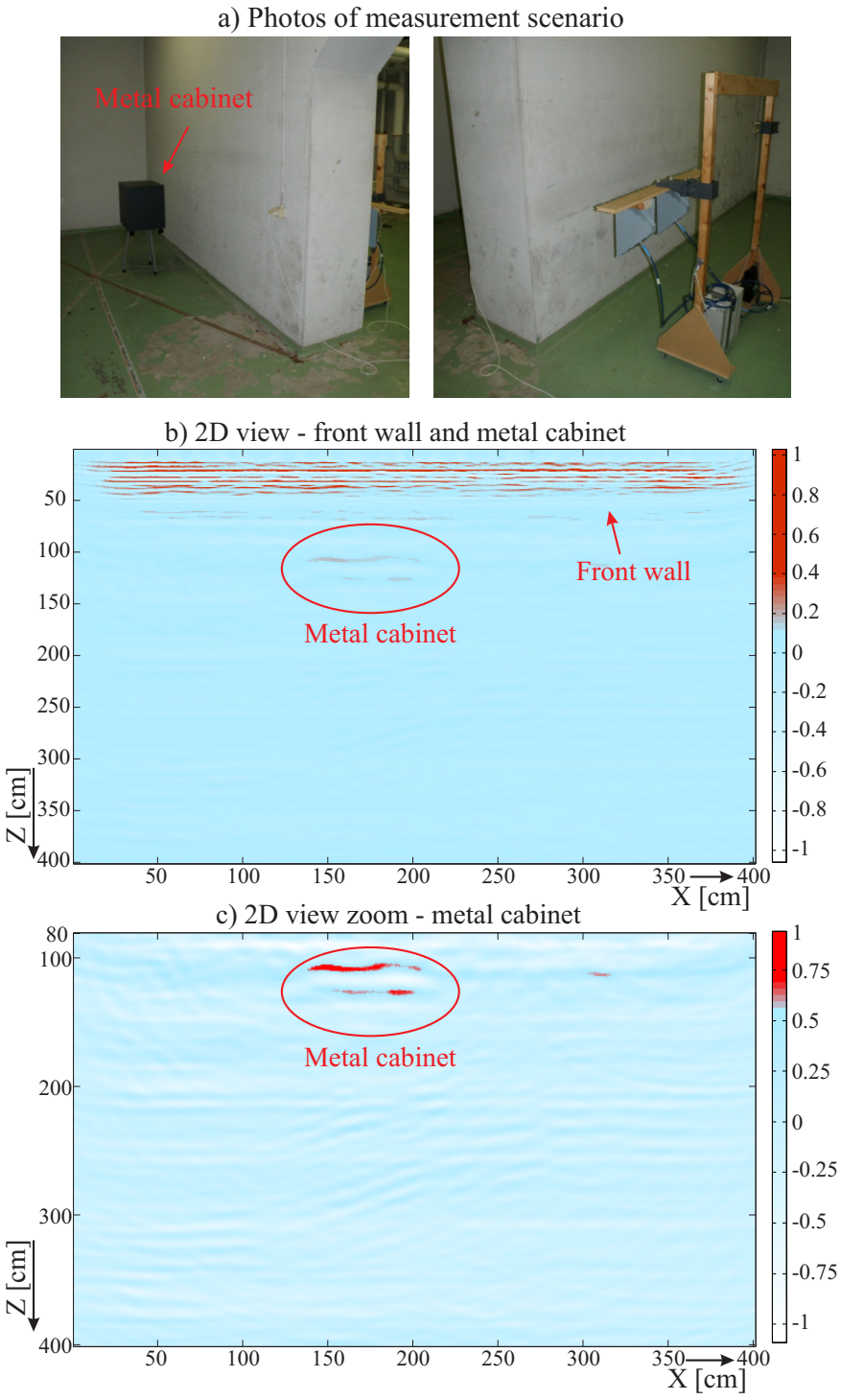

Fig. B.0.1: SAR imaging of the metal cabinet behind the 60 cm concrete wall. a) Photos of measurement scenario. b) 2D view - front wall and metal cabinet. c) 2D view - zoom on metal cabinet only.

Appendix C

Imaging of the Object Behind a Wooden Door

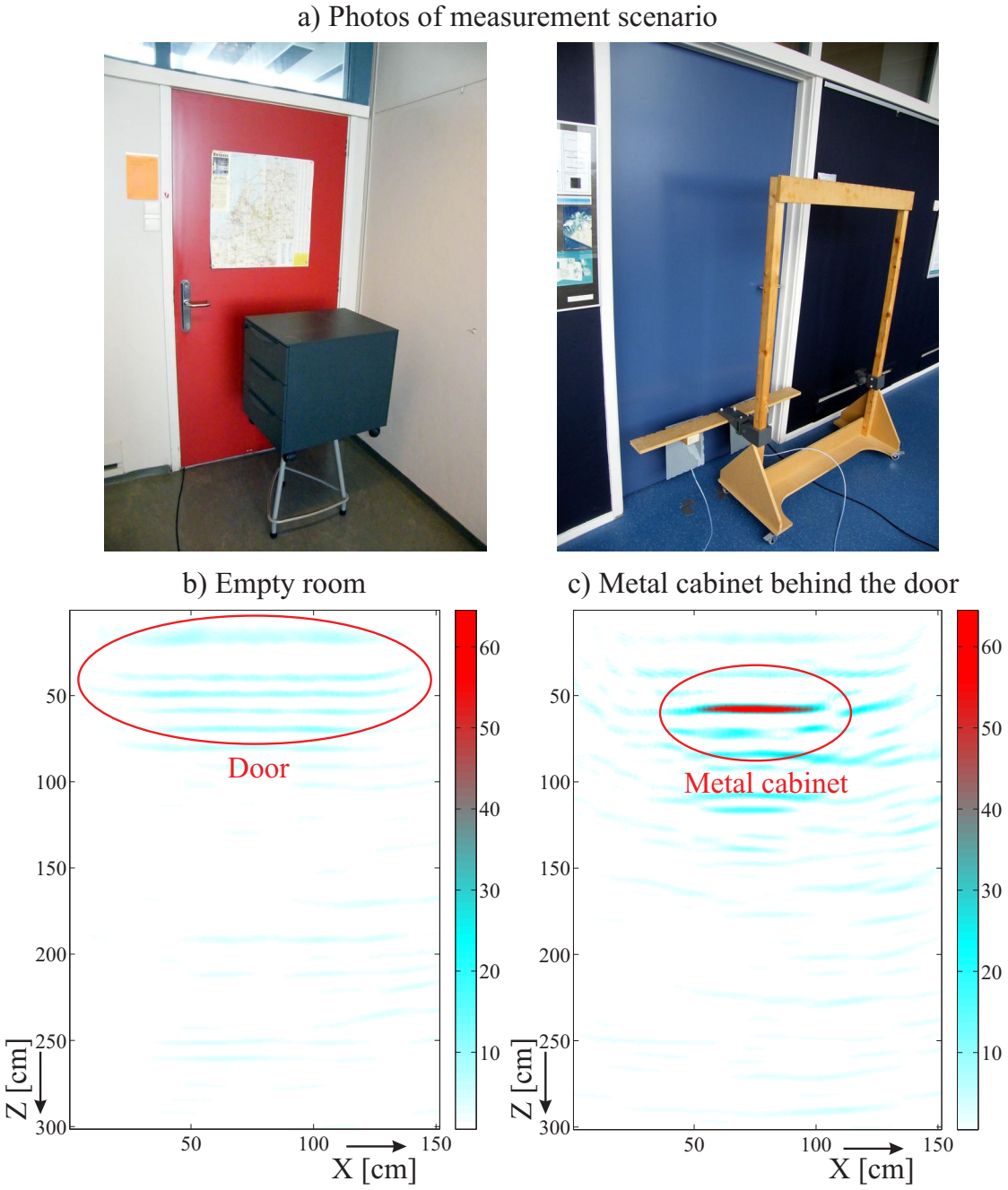

Fig. C.0.1: SAR imaging of the metal cabinet behind the wooden door. a) Photos of measurement scenario. b) 2D view - empty room. c) 2D view - metal cabinet behind the wooden door. Note that b) and c) subfigures have the same colormap.

Bibliography

[1] M. Aftanas, J. Rovnakova, M. Drutarovsky, and D. Kocur, "Efficient Method of TOA Estimation for Through Wall Imaging by UWB Radar," *International Conference on Ultra-Wideband, ICUWB 2008, Hannover, Germany*, vol. 2, pp. 101–104, Sept. 2008.

[2] M. Aftanas, J. Rovnakova, M. Riskova, D. Kocur, , and M. Drutarovsky, "An Analysis of 2D Target Positioning Accuracy for M-sequence UWB Radar System under Ideal Conditions," *Proceedings of 17th International Conference Radioelektronika, Brno, Czech Republic*, pp. 189–194, Apr. 2007.

[3] M. Aftanas, E. Zaikov, M. Drutarovsky, and J. Sachs, "Through Wall Imaging of the Objects Scanned by M-sequence UWB Radar System," *18th International Conference Radioelektronika*, pp. 33–36, Apr. 2008.

[4] M. Aftanas, "Signal Processing Steps for Objects Imaging Through the Wall with UWB Radar," *9th Scientific Conference of Young Researchers, SCYR 2009. Faculty of Electrical Engineering and Informatics, Technical University of Kosice*, pp. 14–17, May 2009.

[5] F. Ahmad and M. G. Amin, "High-Resolution Imaging using Capon Beamformers for Urban Sensing Applications," *Acoustics, Speech and Signal Processing, ICASSP, IEEE*, vol. 2, pp. 985–988, Apr. 2007.

[6] F. Ahmad, M. G. Amin, and S. A. Kassam, "Synthetic aperture beamformer for imaging through a dielectric wall," *Aerospace and Electronic Systems, IEEE*, vol. 41, pp. 271–283, Jan. 2005.

[7] F. Ahmad and M. G. Amin, "Multi-location wideband synthetic aperture imaging for urban sensing applications," *Journal of the Franklin Institute*, vol. 345, pp. 618–639, Sep. 2008.

[8] F. Ahmad, M. G. Amin, and G. Mandapati, "Autofocusing of through-the-wall radar imagery under unknown wall characteristics," *IEEE transactions on image processing*, vol. 16, pp. 1785–1795, July 2007.

[9] F. Ahmad, Y. Zhang, and M. G. Amin, "Three-Dimensional Wideband Beamforming for Imaging Through a Single Wall," *IEEE Geoscience and Remote Sensing Letters*, vol. 5, pp. 176–179, Apr. 2008.

[10] J. B. Anderson, *Digital Transmission Engineering*, 2nd ed. Wiley-IEEE Press, 2005.

[11] L. Y. Astanin and A. A. Kostylev, *Ultrawideband Radar Measurements - Analysis and Processing*. Institution of Engineering and Technology, 1997.

[12] G. Backus and F. Gilbert, "Numerical applications of a formalism for geophysical inverse problems," *Geophysical Journal International*, vol. 13, pp. 247–276, July 1967.

[13] T. W. Barrett, "History of UltraWideBand (UWB) Radar & Communications," *Progress In Electromagnetics Symposium*, July 2000.

[14] C. L. Bastard, V. Baltazart, Y. Wang, and J. Saillard, "Thin-Pavement Thickness Estimation Using GPR With High-Resolution and Superresolution Methods," *IEEE Transactions on Geoscience and Remote Sensing*, vol. 45, pp. 2511–2519, Aug. 2007.

[15] S. Basu and Y. Bresler, "O(N2log2N) Filtered Backprojection Reconstruction Algorithm for Tomography," *IEEE Transactions on Image Processing*, vol. 9, pp. 1760–1773, Oct. 2000.

[16] A. O. Bauer, "The history of a German mobile radar direction finder," *Centre for German Communication and related technology*, Dec. 2004.

[17] A. J. Berkhout, "Wave field extrapolation techniques in seismic migration, a tutorial," *Geophysics*, vol. 46, pp. 1638–1656, Dec. 1981.

[18] M. Bertero and P. Boccacci, "Introduction to Inverse Problems in Imaging," *Inst. of Physics Publ., Bristol*, Jan. 1998.

[19] G. Beylkin, "On the fast Fourier transform of functions with singularities," *Applied and Computational Harmonic Analysis*, vol. 2, pp. 363–381, 1995.

[20] A. Binder, H. W. Engl, C. W. Groetsch, A. Neubauer, and O. Scherzer, "Weakly closed nonlinear operators and parameter identification in parabolic equations by Tikhonov regularization," *Appl. Anal.*, vol. 55, pp. 215–234, Dec. 1994.

[21] A. Boag, Y. Bresler, and E. Michielssen, "A multilevel domain decomposition algorithm for fast O(N2logN) reprojection of tomographic images," *Image Processing, Proceedings International Conference*, vol. 2, pp. 633–636, Dec. 1999.

[22] M. Bragg, *The Location of Aircraft by Radar Methods 1935-1945*. Hawkhead Publishing, May 2002.

[23] S. Brlek, G. Labelle, and A. Lacasse, "The discrete green theorem and some applications in discrete geometry," *Theor. Comput. Sci.*, vol. 346, pp. 200–225, Nov. 2005.

[24] D. Calvetti and L. Reichel, "On the evaluation of polynomial coefficients," *Numerical Algorithms*, vol. 33, pp. 153–161, Aug. 2003.

[25] J. Canny, "A computational approach to edge detection," *IEEE Transactions on Pattern Analysis and Machine Intelligence*, vol. 8, pp. 679–698, Nov. 1986.

[26] S. Caorsi, G. L. Gragnanit, and M. Pastorino, "Microwave imaging by three-dimensional born linearization of electromagnetic scattering," *Rndio Sci.*, vol. 25, pp. 1221–1229, Dec. 1990.

[27] R. Chandra, A. N. Gaikwad, D. Singh, and M. J. Nigam, "An approach to remove the clutter and detect the target for ultra-wideband through-wall imaging," *Journal of Geophysics and Engineering*, vol. 5, pp. 412–419, Oct. 2008.

[28] J. Chen, G. Fang, and F. Li, "Image Correction for UWB Through-wall Imaging Radar," *7th International Symposium on Antennas, Propagation and EM Theory, 2006. ISAPE 06*, vol. 7, pp. 1–4, Oct. 2006.

[29] L. Chen and S. Ouyang, "Modified Cross-Correlated Back Projection for UWB Through-Wall Surveillance," *International Conference on Wireless Communications, Networking and Mobile Computing, WiCom 2007*, pp. 516–519, Sep. 2007.

[30] L. Chen and O. Shan, "A time-domain beamformer for UWB through-wall imaging," *IEEE Region 10 Conference TENCON 2007*, pp. 1–4, Nov. 2007.

[31] ——, "Through-wall Surveillance using Ultra-wideband Short Pulse Radar: Numerical Simulation," *2nd IEEE Conference on Industrial Electronics and Applications, ICIEA 2007*, pp. 1551–1554, May 2007.

[32] M. Cheney, "The linear sampling method and the MUSIC algorithm," *Inverse Problems*, vol. 17, pp. 591–595, Aug. 2001.

[33] J. Cheng-Li, J. Ke-Feng, J. Yong-Mei, and K. Gang-Yao, "Road extraction from high-resolution SAR imagery using Hough transform," *IEEE International Geoscience and Remote Sensing Symposium, IGARSS 05*, vol. 1, pp. 25–29, July 2005.

[34] J. F. Claerbout and S. Fomel, *Image Estimation by Example: Geophysical Soundings Image Construction: Multidimensional Autoregression.* Palo Alto:Stanford University, 2002.

[35] J. F. Claerbout, "Earth soundings analysis: Processing versus inversion," Ph.D. dissertation, Cecil and Ida Green Professor of Geophysics, Stanford University, Mar. 2004.

[36] M. C. Cobb and J. H. McClellan, "Omega-k quadtree UWB SAR focusing," *Radar Conference, Proceedings of the IEEE*, vol. 1, pp. 311–214, May 2001.

[37] D. Colton, M. Piana, and R. Potthast, "A simple method using Morozov's discrepancy principle for solving inverse scattering problems," *Inverse Problems*, vol. 13, pp. 1477–1493, Dec. 1997.

[38] S. Crabbe, M. Aftanas, P. A. Berthlin, M. Drutarovsky, R. Klukas, D. Kocur, T. T. Nguyen, P. Peyerl, J. Rovnakova, J. Sachs, and E. Zaikov, "Ultra wideband radar for through wall detection from the RADIOTECT project," *3rd Security Research Conference, Future Security*, pp. 299–304, Sep. 2008.

[39] G. Cui, L. Kong, and J. Yang, "A Back-Projection Algorithm to Stepped-Frequency Synthetic Aperture Through-the-Wall Radar Imaging," *1st Asian and Pacific Conference on Synthetic Aperture Radar, 2007. APSAR 2007.*, pp. 123–126, Nov. 2007.

[40] G. Cui, L. Kong, J. Yang, and X. Wang, "A New Wall Compensation Algorithm for Through-the-wall Radar Imaging," *Synthetic Aperture Radar, 2007. APSAR 2007*, pp. 393–396, Nov. 2007.

[41] J. C. Curlander and R. N. McDonough, *Synthetic Aperture Radar: Systems and Signal Processing.* New York: John Wiley and Sons, Nov. 1991.

[42] D. Daniels, *Surface Penetrating Radar - 2nd Edition.* The Institution of Electrical Engineers (IEE), 2004.

[43] ——, "M-sequence radar," in *Ground Penetrating Radar.* London, United Kingdom: The Institution of Electrical Engineers.

[44] M. Dehmollaian and K. Sarabandi, "Refocusing Through Building Walls Using Synthetic Aperture Radar," *IEEE Transactions on Geoscience and Remote Sensing*, vol. 46, pp. 1589–1599, June 2008.

[45] M. Dehmollaian, M. Thiel, and K. Sarabandi, "Through-the-Wall Imaging Using Differential SAR," *IEEE Transactions on Geoscience and Remote Sensing*, vol. 47, pp. 1289–1296, May 2009.

[46] G. Derveaux, G. Papanicolaou, and C. Tsogka, "Time reversal imaging for sensor networks with optimal compensation in time," *The Journal of the Acoustical Society of America*, vol. 121, pp. 2071–2085, Apr. 2007.

[47] M. D. Desai and K. Jenkins, "Convolution backprojection image reconstruction for spotlight mode synthetic aperture radar," *IEEE Trans. on image processing*, vol. 1, pp. 505–517, Oct. 1992.

[48] A. J. Devaney, "Super-resolution processing of multi-static data using time reversal and MUSIC," *Preprint, Northeastern University*, 2000.

[49] A. Devaney, *Class notes of Inverse Problems in Electromagnetism.* Boston: Department of Electrical and Computer Eng., Northeastern University, 2001.

[50] Y. Ding and D. C. Munson, "A fast back-projection algorithm for bistatic SAR imaging," *Image Processing, Proceedings International Conference*, vol. 2, pp. 449–452, 2002.

[51] P. Docherty, "A brief comparison of some kirchhoff integral formulas for migration and inversion," *Geophysics*, vol. 56, pp. 1264–1169, Aug. 1991.

[52] R. O. Duda and P. E. Hart, "Use of the Hough transformation to detect lines and curves in pictures," *ACM New York*, vol. 15, pp. 11–15, Jan. 1973.

[53] A. Dutt and V. Rokhlin, "Fast Fourier transforms for nonequispaced data," *SIAM Journal on Scientific Computing*, vol. 14, pp. 1368–1393, Nov. 1993.

[54] E. Eide, "Radar imaging of small objects closely below the earth surface," Ph.D. dissertation, Norwegian University of Science and Technology, Norway, Aug. 2000.

[55] H. W. Engl, M. Hanke, and A. Neubauer, *Regularization of Inverse Problems.* New York: Springer, July 1996.

[56] C. K. et all, *Unexploded Ordnance Detection and Mitigation.* Springer Netherlands, 2009, ch. UXO Signal Multi Sensor Detection and Estimation.

[57] X. Feng and M. Sato, "Pre-stack migration applied to GPR for landmine detection," *Inverse Problems*, vol. 20, pp. 1–17, Nov. 2004.

[58] R. Fisher, S. Perkins, A. Walker, and E. Wolfart, "Hypermedia Image Processing Reference," *[online] available at: http://homepages.inf.ed.ac.uk/rbf/HIPR2/*, Oct. 2000.

[59] C. Gauss, "Allgemeine Flachentheorie," *W. Engelmann , Leipzig, (Translated from Latin)*, 1900.

[60] S. Gauthier and W. Chamma, "Through-The-Wall Surveillance," *Technical Memorandum DRDC, Ottawa*, Oct. 2002.

[61] S. Gauthier, E. Hung, and W. Chamma, "Surveillance Through Concrete Walls," *Proceedings of SPIE 5403*, pp. 597–608, Dec. 2004.

[62] J. Gazdag, "Wave-equation migration with the phase-shift method," *Geophysics*, vol. 43, pp. 1342–1351, Dec. 1978.

[63] S. H. Gray, "Efficient traveltime calculations for kirchhoff migration," *Geophysics*, vol. 51, pp. 1685–1688, Aug. 1986.

[64] F. K. Gruber, E. A. Marengo, and A. J. Devaney, "Time-reversal imaging with multiple signal classification considering multiple scattering between the targets," *Acoustical Society of America Journal*, vol. 115, pp. 3042–3047, 2004.

[65] M. N. Guddati and A. H. Heidari, "Migration with arbitrarily wide-angle wave equations," *Geophysic*, vol. 70, pp. 61–70, May 2005.

[66] A. Gunawardena and D. Longstaff, "Wave equation formulation of Synthetic Aperture Radar (SAR) algorithms in the time-space domain," *IEEE Transactions on Geoscience and Remote Sensing*, vol. 36, pp. 1995–1999, Nov. 1999.

[67] K. Haddadi, M. M. Wang, O. Benzaim, D. Glay, and T. Lasri, "Contactless Microwave Technique Based on a Spread-Loss Model for Dielectric Materials Characterization," *IEEE Microwave and Wireless Components Letters*, vol. 19, pp. 33–35, Jan. 2009.

[68] S. Hantscher, B. Praher, A. Reisenzahn, and C. G. Diskus, "Analysis of Imaging Radar Algorithms for the Identifcation of Targets by Their Surface Shape," *Antennen und Messverfahren fr Ultra-Wide-Band (UWB)-Systeme*, Dec. 2006.

[69] S. Hantscher, A. Reisenzahn, and C. G. Diskus, "Through-Wall Imaging With a 3-D UWB SAR Algorithm," *IEEE Signal Processing Letters*, vol. 15, pp. 269–272, 2008.

[70] M. A. Haun, D. L. Jones, and W. D. O'Brien, "Efficient three-dimensional imaging from a small cylindrical aperture," *Ultrasonics Symposium, IEEE Transactions*, vol. 2, pp. 1589–1592, Oct. 2000.

[71] G. T. Herman, *Image reconstruction from projections.* Berlin, Germany: Spriner-Verlag, Oct. 1980.

[72] A. Ho, W. H. Tham, and K. S. Low, "Improving classification accuracy in through-wall radar imaging using hybrid prony's and singular value decomposition method," *Geoscience and Remote Sensing Symposium, IGARSS, Proceedings IEEE*, vol. 6, pp. 4267–4270, July 2005.

[73] A. J. Hunter, M. P. Hayes, and P. T. Gough, "A Comparison Of Fast Factorised Back-Projection And Wavenumber Algorithms for SAS image reconstruction," *WCU 2003, Paris*, pp. 527–530, Sep. 20003.

[74] I. Immoreev and Fedotov, "Ultra wideband radar systems: advantages and disadvantages," *Ultra Wideband Systems and Technologies*, pp. 201–205, 2002.

[75] J. D. Jackson, *Classical electrodynamics.* New York: J. Wiley and Sons, Aug. 1998.

[76] E. M. Johansson and J. E. Mast, "Three-dimensional ground-penetrating radar imaging using synthetic aperture time-domain focusing," *AMMWD, Proceedings of SPIE*, vol. 2275, pp. 205–214, Sep. 1994.

[77] S. Kaczmarz, "Angenaehrte Aufloesung von Systemen Linearer Gleichungen," *Bulletin of the Polish Academy of Sciences Letters*, pp. 355–357, 1937.

[78] A. C. Kak and M. Slaney, *Principles of computerized tomographic imaging.* Society for Industrial Mathematics, July 2001.

[79] L. V. Kempen, "Ground penetrating radar for anti-personnel landmine detection," Ph.D. dissertation, Vrije Universiteit Brussel, Faculty of Engineering Sciences, Dept. of Electronics and Informatics (ETRO), Sept. 2006.

[80] H. Khatri and C. Le, "Identification of Electromagnetic Parameters of a Wall and Determination of Radar Signal Level Behind a Wall," *Proceedings of SPIE, the International Society for Optical Engineering*, vol. 6210, pp. 1–7, Apr. 2006.

[81] S. Kidera, T. Sakamoto, and T. Sato, "A high-resolution 3-D imaging algorithm with linear array antennas for UWB pulse radar systems," *Antennas and Propagation Society International Symposium 2006, IEEE*, pp. 1057–1060, July 2006.

[82] A. Kirsch, "The MUSIC algorithm and the factorization method in inverse scattering theory for inhomogeneous media," *Inverse Problems*, vol. 18, pp. 1025–1040, June 2002.

[83] G. D. Knott, *Interpolating Cubic Splines*, 1st ed. Birkhauser Boston, 1999.

[84] K. Ladas and A. Devaney, "Generalized ART algorithm for diffraction tomography," *Inverse Problems*, vol. 7, pp. 109–125, Feb. 1991.

[85] G. A. Latham, "Best L2 Tikhonov analogue for Landweber iteration," *Inverse Problems*, vol. 14, pp. 1527–1537, 1998.

[86] C. Lei and S. Ouyang, "Through-wall Surveillance using Ultra-wideband Short Pulse Radar: Numerical Simulation," *Industrial Electronics and Applications, 2007*, pp. 1551–1554, May 2007.

[87] W. Lertniphonphun and J. H. McClellan, "Migration of underground targets in UWB-SAR systems," *IEEE Trans. Image Processing*, vol. 1, pp. 713–716, 2000.

[88] A. Li, "Algorithms for the implementation of Stolt interpolation in SAR processing," *Proceedings of the 12th Annual International Geoscience and Remote Sensing Symposium*, vol. 1, pp. 360–362, May 1992.

[89] R. Linnehan, J. Schindler, D. Brady, R. Kozma, R. Deming, and L. Perlovsky, "Dynamic Logic Applied to SAR Data for Parameter Estimation Behind Walls," *IEEE Radar Conference 2007*, pp. 850–855, Apr. 2007.

[90] K. Liu and J. C. Bancroft, "The effects of dip-limited Kirchhoff migration and F-K migration," *CREWES Research Report*, 2002.

[91] Q. H. Liu and N. Nguyen, "An Accurate Algorithm for Nonuniform Fast Fourier Transforms (NUFFT's)," *Microwave and Guided Wave Letters, IEEE*, vol. 8, pp. 18–20, Jan. 1998.

[92] X. Liu and H. Leung, "Through the Wall Imaging using Chaotic Modulated Ultra Wideband Synthetic Aperture Radar," *IEEE International Conference on Acoustics, Speech and Signal Processing,ICASSP 2007*, vol. 3, pp. 1257–1260, Apr. 2007.

[93] D. Loewenthal, L. Lu, R. Roberson, and J. W. C. Sherwood, "The Wave Equation Applied to Migration," *Geophys. Prosp.*, vol. 24, pp. 380–399, June 1976.

[94] R. Lomas, *The Man who Invented the Twentieth Century.* Headline Book Publishing, Jan. 1999.

[95] G. Mandapati and M. Amin, "Blurness and focusing-defocusing for Through the Wall Radar Imaging," *Signal Processing and Information Technology, 2004*, pp. 246–249, Dec. 2004.

[96] G. F. Margrave, "Numerical methods of exploration seismology with algorithms in matlab," Master's thesis, Department of Geology and Geophysics, The University of Calgary, Jan. 2001.

[97] J. McCorkle and M. Rofheart, "An order N2log(N) backprojettor algorithm for focusing wide-angle wide-bandwidth arbitrary-motion synthetic aperture radar," *SPIE Radar Sensor Technology Conference Proceedings*, vol. 2747, pp. 25–36, June 1996.

[98] D. Miller, M. Oristaglio, and G. BeylkinG, "A new slant on seismic imaging," *Migration and integral geometry: Geophysics*, vol. 52, pp. 943–964, July 1987.

[99] L. Min, "Seismic applications of interactive computational methods," Master's thesis, The Department of Geosciences, University of Sydney, July 2000.

[100] A. Moreira, J. Mittermayer, and R. Scheiber, "Extended chirp scaling algorithm for air and spaceborne SAR data processing in stripmap and ScanSAR imaging modes," *IEEE Trans. Geosci. Remote Sens.*, vol. 34, pp. 1123–1136, Sep. 1996.

[101] A. Muqaibai, A. Safaai-Jazi, A. Bayram, A. Attiya, and S. Riad, "Ultrawideband through-the-wall propagation," *IEE Proc. Microw. Antennas*, vol. 152, pp. 581–588, Dec. 2005.

[102] A. Muqaibel and A. Safaai-Jazi, "A new formulation for characterization of materials based on measured insertion transfer function," *Microwave Theory and Techniques*, vol. 51, pp. 1946–1951, Aug. 2003.

[103] A. Muqaibel, A. Safaai-Jazi, A. Bayram, A. Attiya, and S. Riad, "Ultrawideband through-the-wall propagation," *Microwaves, Antennas and Propagation, IEE Proceedings*, vol. 153, pp. 581– 588, Dec. 2005.

[104] F. Natterer, "Imaging and inverse problems of partial differential equations," *Jahresber. Deutsch. Math.*, vol. 109, pp. 31–48, Apr. 2006.

[105] N. Nguyen and Q. H. Liu, "The regular Fourier matrices and nonuniform fast Fourier transforms," *SIAM Journal on Scientific Computing*, vol. 21, pp. 283–293, Aug. 1999.

[106] P. Pardalos and H. Romeijn, *Handbook of Global Optimization*, 2nd ed. Springer, June 2002.

[107] A. Quarteroni, R. Sacco, and F. Saleri, *Rootfinding for Nonlinear Equations.* Springer New York, Aug. 2007, vol. 37.

[108] S. J. Radzevicius, B. T. Clark, D. Herbst, and T. T. Webster, "Imaging columns with GPR," *IEEE Proceedings on Ground Penetrating Radar*, vol. 1, pp. 387–390, 2004.

[109] J. Reed, R. Buerhrer, and D. Mckinstry, *Introduction to UWB: Impulse Radio for Radar and Wireless Communications.* GM Briefing, Aug. 2002.

[110] A. Reigber, E. Alivizatos, A. Potsis, and A. Moreira, "Extended wavenumber-domain synthetic aperture radar focusing with integrated motion compensation," *Radar, Sonar and Navigation, IEE Proceedings*, vol. 153, pp. 301–310, June 2006.

[111] M. Riskova, J. Rovnakova, and M. Aftanas, "M-Sequence UWB Radar Architecture or Throughwall Detection and Localisation," *7th PhD Student Conference and Scientific and Technical Competition of Students of Faculty of Electrical Engineering and Informatics, Technical University of Kosice, Slovakia*, pp. 29–30, May 2007.

[112] E. A. Robinson and S. Treitel, *Geophysical signal analysis.* Southampton, United Kingdom: Prentice-Hall, Aug. 1980.

[113] F. Roth, *Convolutional Models for Landmine Identification with Ground Penetrating Radar.* Amsterdam: Delft University Press, Jan. 2005.

[114] J. Rovoňáková and D. Kocur, "Compensation of Wall Effect for Through Wall Tracking of Moving Targets," *Radioengineering journal: Special Issue on Workshop of the COST Action IC0803*, vol. 18, no. 2, pp. 189–195, June 2009.

[115] J. Sachs, M. Aftanas, S. Crabbe, M. Drutarovsky, R. Klukas, D. Kocur, T. Nguyen, P. Peyerl, J. Rovnakova, and E. Zaikov, "Detection and Tracking of Moving or Trapped People Hidden by Obstacles using Ultra-Wideband Pseudo-Noise Radar," *5th European Radar Conference, EuRAD 2008*, pp. 408–411, Oct. 2008.

[116] J. Sachs, P. Peyerl, P. Rauschenbach, F. Tkac, M. Kmec, and S. Crabbe, "Integrated Digital UWB-Radar," *Amerem 2002*, pp. 507–514, Juny 2002.

[117] J. Sachs, P. Peyerl, and M. Rossberg, "A New UWB-Principle for Sensor-Array Application," *IEEE proceedings of IMTC/99*, vol. 3, May 1999.

[118] J. Sachs, P. Peyerl, R. Zetik, and S. Crabbe, "M-Sequence Ultra-Wideband-Radar: State of Development and Applications," *Radar 2003, Adelaide (Australia)*, pp. 224–229, Sep. 2003.

[119] F. Sagnard and G. E. Zein, "In Situ Characterization of Building Materials for Propagation Modeling: Frequency and Time Responses," *IEEE Transactions on Antennas and Propagation*, vol. 53, pp. 3166–3173, Oct. 2005.

[120] T. Sakamoto and T. Sato, "A target shape estimation algorithm for pulse radar systems based on Boundary Scattering Transform," *IEICE Transactions on Communications*, vol. 87, pp. 1357–1365, May 2004.

[121] ——, "A fast algorithm of 3-dimensional imaging for pulse radar systems," *IEEE AP-S International Symposium and USNC/URSI National Radio Science Meeting*, vol. 3, pp. 2099–2102, June 2004.

[122] P. C. Sava, "Prestack residual migration in the frequency domain," *Geophysics*, vol. 68, pp. 634–640, Mar. 2003.

[123] T. Savelyev, L. van Kempen, and H. Sahli, "GPR Antipersonnel Mine Detection: Improved Deconvolution and Time-Frequency Feature Extraction," *SPIE, Nondestructive Evaluation and Health Monitoring of Aerospace Materials and Composites II*, vol. 5046, pp. 232–241, 2003, san Diego, USA.

[124] J. A. Scales, *Theory of Seismic Imaging*. New York: Springer, Jan. 1995.

[125] B. Scheers, "Ultra-wideband ground penetrating radar, with application to the detection of anti personnel landmines," Ph.D. dissertation, Universit Catholique de Louvain, Belgium, 2001.

[126] B. Scheers, M. Archeroy, and A. V. Vander, "Time-domain modeling of UWB GPR and its application to land mine detection," *SPIE, Detection and Remediation Technologies for Mines and Minelike Targets V*, vol. 4038, pp. 1452–1460, Aug. 2000, orlando, FL, USA.

[127] R. O. Schmidt, "Multiple emitter location and signal parameter estimation," *IEEE Trans.*, vol. 34, pp. 276–280, Mar. 1986.

[128] W. S. Schneider, "Integral formulation for migration in two or three dimensions," *Geophysics*, vol. 43, pp. 49–76, 1978.

[129] L. G. Shapiro and G. Stockman, *Computer Vision*. Prentice-Hall, 2001.

[130] P. Shargo and J. Melody, "Model-based Correction of Through-wall SAR Imagery via Raytracing," *IEEE Radar Conference 2007*, pp. 706–711, Apr. 2007.

[131] F. Soldovieri and R. Solimene, "Through-Wall Imaging via a Linear Inverse Scattering Algorithm," *IEEE Geoscience and Remote Sensing Letters*, vol. 4, pp. 513–517, Oct. 2007.

[132] L.-P. Song, C. Yu, and Q. H. Liu, "Through-wall imaging (TWI) by radar: 2-D tomographic results and analyses," *Geoscience and Remote Sensing, IEEE*, vol. 43, pp. 2793–2798, Dec. 2005.

[133] R. H. Stolt, "Migration by Fourier transform," *Geophysics*, vol. 43, pp. 23–48, Feb. 1978.

[134] J. A. Stratton, *Electromagnetic Theory - A classic Reissue.* Wiley-IEEE Press, 2007.

[135] B. Subiza, E. Gimeno-Nieves, J. M. Lopez-Sanchez, and J. Fortuny-Guasch, "An Approach to SAR Imaging by Means of Non-Uniform FFT's," *Geoscience and Remote Sensing Symposium. IGARSS apos.*, vol. 6, pp. 4089–4091, July 2003.

[136] R. Tanaka, "Report on SAR imaging," Internal Report, Oct. 2003.

[137] N. Thanh, L. van Kempen, T. Savelyev, X. Zhuge, M. Aftanas, E. Zaikov, M. Drutarovsky, and H. Sahli, "Comparison of Basic Inversion Techniques for Through-Wall Imaging Using UWB Radar," *Proceedings of the 5th European Radar Conference - EuRAD*, pp. 140–143, Oct. 2008.

[138] C. W. Therrien, *Discrete Random Signals and Statistical Signal Processing.* Hemel Hempstead: Prentice-Hall International.

[139] J. P. Tignol, *Galois' Theory of Algebraic Equations.* World Scientific Publishing Company, July. 2001.

[140] L. Ulander, H. Hellsten, and Stenstrom, "Synthetic aperture radar processing using fast factorized back-projection," *Aerospace and Electronic Systems*, vol. 39, pp. 760–776, July 2003.

[141] G. Wang and M. G. Amin, "Imaging Through Unknown Walls Using Different Standoff Distances," *Signal Processing, IEEE*, pp. 4015–4025, Oct. 2006.

[142] H. Wang, Z. Zhou, and L. Kong, "Wall Parameters Estimation for Moving Target Localization with Through-the-Wall Radar," *Microwave and Millimeter Wave Technology, 2007*, pp. 1–4, Apr. 2007.

[143] J. W. Wiggins, "Kirchhoff integral extrapolation an migration of nonplanar data," *Geophysics*, vol. 49, pp. 1239–1248, Aug. 1984.

[144] S. Xiao, D. C. Munson, S. Basu, and Y. Bresler, "An N2logN back-projection algorithm for SAR image formation," *Signals, Systems and Computers, Conference Record of the Thirty-Fourth Asilomar Conference*, vol. 1, pp. 3–7, 2000.

[145] S. Xu and D. Pham, "Seismic Data Regularization with Anti-Leakage Fourier Transform," *66th EAGE Conference and Exhibition, Paris*, vol. 66, June 2004.

[146] X. Xu and E. L. Miller, "Optimization of Migration Method to Locate Buried Object in Lossy Medium," *Geoscience and Remote Sensing Symposium, IGARSS apos., IEEE International*, vol. 1, pp. 337–339, June 2002.

[147] B. Yang, A. Yarovoy, T. Savelyev, and L. Ligthart, "Estimated Path Loss for Through Wall Imaging," *Internal Radiotect intermediate report on workpackage 2, IRCTRS01807*, May 2007.

[148] A. Yegulalp, "Fast backprojection algorithm for synthetic aperture radar," *Proceedings of the IEEE National Radar Conference*, pp. 60–65, 1999.

[149] R. Yelf, "Where is true time zero?" *Proceedings of the Tenth International Conference on Ground Penetrating Radar*, vol. 1, pp. 279–282, June 2004.

[150] O. Yilmaz, *Seismic Data Processing, volume 2 of Investigations in Geophysics.* Tulsa: Society of Exploration Geophysicists, Oct. 1987.

[151] Y.-S. Yoon and M. G. Amin, "High-Resolution Through-the-Wall Radar Imaging Using Beamspace MUSIC," *IEEE Transactions on Antennas and Propagation*, vol. 56, pp. 1763–1774, June 2008.

[152] E. Zaikov, J. Sachs, M. Aftanas, and J. Rovnakova, "Detection of trapped people by UWB radar," *German Microwave Conference, GeMiC 2008*, pp. 240–243, Mar. 2008.

[153] R. Zetik and J. Sachs, "Time-Frequency Signal Representations Applied to Ultra Wideband Radar," *German Radar Symposium GRS*, Oct. 2000.

[154] R. Zetik, J. Sachs, and R. Thome, "Imaging of Propagation Environment by UWB Channel Sounding," *XXVIIIth URSI General Assembly*, Oct. 2005.

[155] J. Zhang, M. Nakhkash, and Y. Huang, "Electromagnetic imaging of layered building materials," *Measurement of Science and Technology, IOP Journal*, vol. 12, pp. 1147–1152, May 2001.

[156] K. Zhang and D. Li, *Electromagnetic Theory for Microwaves and Optoelectronics*, 2nd ed. Springer-Verlag Berlin and Heidelberg GmbH, 2008.

[157] W. Zheng, Z. Zhao, and Z. P. Nie, "Application of TRM in the Uwb Through Wall Radar," *Progress In Electromagnetics Research, PIER 87*, vol. 87, pp. 279–296, 2008.